

Experiments with Trapped RbCs Molecules

A Dissertation
Presented to the Faculty of the Graduate School
of
Yale University
in Candidacy for the Degree of
Doctor of Philosophy

by
Nathan Brown Gilfoy

Dissertation Director: David DeMille

December, 2011

UMI Number: 3496848

All rights reserved

INFORMATION TO ALL USERS

The quality of this reproduction is dependent upon the quality of the copy submitted.

In the unlikely event that the author did not send a complete manuscript and there are missing pages, these will be noted. Also, if material had to be removed, a note will indicate the deletion.



UMI 3496848

Copyright 2012 by ProQuest LLC.

All rights reserved. This edition of the work is protected against unauthorized copying under Title 17, United States Code.



ProQuest LLC
789 East Eisenhower Parkway
P.O. Box 1346
Ann Arbor, MI 48106-1346

ABSTRACT

Experiments with Trapped RbCs Molecules

Nathan Brown Gilfoy

2011

We measure the inelastic collision rates of ultracold, vibrationally excited RbCs molecules with Rb and Cs atoms. In order to do this we have demonstrated simultaneous optical trapping of $T = 250 \mu\text{K}$ RbCs molecules and their constituent atoms. Electronic ground state, vibrationally excited RbCs molecules are created via photoassociation from laser-cooled samples of Rb and Cs atoms. A sample consisting of molecules, atoms, or a combination of the two can be confined in a far red detuned optical lattice. Measurements of the trap lifetimes of the molecules in the lattice show background-gas limited collision rates for the molecules. Co-trapping atoms with the molecules results in strong inelastic collisions in the sample. We used state-sensitive detection to measure the molecular scattering rate with the two species of atoms over an order of magnitude in molecular binding energies. We find that there is no dependence of the molecule-atom cross-section on molecular vibrational quantum number.

Copyright © 2011 by Nathan Brown Gilfoy

All rights reserved.

ACKNOWLEDGEMENTS

I'd like to thank Dave DeMille for his otherworldly patience throughout my time here in New Haven. Dave's insight, encouragement, and famous teaching abilities were such a huge help that it would be impossible for me to overstate what they meant to my progress and the experiment. So, thanks Dave.

I'd also like to thank my thesis committee for agreeing to meet on such short notice and for being genuinely engaged in the work.

Thank you to Dr. Hudson, who taught me everything I know about experimental physics while showing me how science really gets done. Any positive technical trait should be attributed to his guidance, and anything else is wholly a result of my own failings. Thank you to Bruzer, Iceman, Steve Falcon, and The Sage for extreme tolerance in the lab under my always-sunny disposition. We had excellent times, gentlemen.

Thanks to all the other DeMillionaires past and present. I would never have graduated without so many tolerant souls of off which to bounce ideas and "borrow" equipment.

I would like to thank my Mom and Jed for their unconditional support and tolerance of this puzzling endeavor.

Thank you Steph for standing by me, keeping me sane, and making me laugh.

Finally, and with much trepidation, I would like to thank my father. I'll never forget the joy he brought us all, the lessons he taught me, and the example he set every day of his too-short life. Although he never saw the experiment, he made me promise him I'd finish the PhD. We'll all miss him every day of our lives.

For Peter

Contents

1	INTRODUCTION.....	1
1.1	History.....	1
1.2	Applications of Ultracold, Polar Molecules.....	3
1.2.1	Ultracold Chemistry.....	3
1.2.2	Quantum Computation.....	4
1.2.3	Quantum Simulation.....	5
1.2.4	Precision Measurements.....	5
1.3	Experimental Techniques for Producing Cold Molecules.....	6
1.3.1	Fano-Feschbach Association.....	7
1.3.2	Buffer Gas Cooling.....	7
1.3.2	Stark Deceleration.....	8
2.	TRAPPING AND COOLING ATOMS.....	10
2.1	Laser Cooling.....	10
2.1.1	The Light Force.....	10
2.1.2	1-D Doppler Cooling and Optical Molasses.....	14
2.1.3	The Magneto Optical Trap.....	16
2.2	Trapping and Cooling Actual Rubidium and Cesium Atoms.....	18
2.2.1	Loading Techniques.....	21
2.2.2	MOT Diagnostics.....	27
2.3	The Second Generation Apparatus.....	33
2.3.1	Vacuum Apparatus Construction.....	33

2.3.2	Bake Protocol.....	36
2.3.3	Degassing.....	39
2.3.4	Electric and Magnetic Fields	40
2.3.5	Diode Laser Systems.....	42
3.	THE OPTICAL LATTICE.....	45
3.1	Background	45
3.1.1	The Dipole Force	45
3.1.3	Quasi Electrostatic Traps and Lattices.....	47
3.1.2	Gaussian Beam Traps	49
3.1.4	Trapping Actual Atoms and Molecules	51
3.2	Experimental Implementation of the Lattice	51
3.2.1	The CO ₂ Laser.....	52
3.2.2	The CO ₂ AOM.....	53
3.2.3	Development of the Beam Line	55
3.3	Lattice Diagnostics.....	59
3.3.1	Absorption Measurements in the Lattice	60
3.3.2	Loading Protocols	62
3.3.3	Temperature Measurements.....	64
3.4	Ion Detection.....	66
3.4.1	Resonance Enhanced Multi-Photon Ionization.....	66
3.4.2	Lifetime Measurements	67
4.	BASIC MOLECULAR THEORY.....	70
4.1	Introduction.....	70

4.1.1	The Born-Oppenheimer Approximation	70
4.1.2	Molecular State Labeling and Selection Rules	74
4.1.3	Electric Dipole Transitions in Molecules	77
4.2	Collision Theory	81
4.2.1	Basic Elastic Collision Theory.....	81
4.2.2	Inelastic Collisions and Photoassociation.....	85
5	MEASUREMENT OF RBCS COLLISION RATES	91
5.1	Experiment Overview	91
5.1.1	Experimental Photoassociation	92
5.1.2	Ion Detection.....	95
5.1.3	Push Beams.....	99
5.1.4	Signal Optimization.....	101
5.1.5	Experimental Lattice Loading.....	102
5.2	Results of the Collision Experiments.....	104
5.2.1	Lifetime Measurements.....	104
5.2.2	Inelastic Collision Model	109
6	CONCLUSION	113

List of Figures

Figure 2.1: A summary of the 1-D MOT model.....	18
Figure 2.2: Schematic of the actual trap levels.	19
Figure 2.3: Schematic representaion of lightpipe assembly	24
Figure 2.4: Typical results of loading via LIAD.....	26
Figure 2.5: Typical results of a MOT absorption measurement.	31
Figure 2.6: Schematic of the vacuum chamber.....	35
Figure 2.7: Schematic of the chamber electrodes	41
Figure 2.8: Schematic of the lasers and optics.....	43
Figure 3.1: Summary of Gaussian beam parameters	50
Figure 3.3: A typical QUEST absorption measurement.	62
Figure 3.4: Effect of Optical Molasses on QUEST loading.	63
Figure 3.5: Ballistic expansion measurement of Rb in a lattice	65
Figure 3.6: Schematic representation of ion detection.....	67
Figure 3.7: Difference in trap lifetime with and without a shutter.	68
Figure 4.1: Vector Diagrams of relevant Hund's cases.....	76
Figure 4.2: Structure of Born Oppenheimer potentials.....	79
Figure 4.3: The mechanics of a free-to-bound transition.....	86
Figure 4.4: The process of photoassociation.....	90
Figure 5.1: RbCs levels used in photoassociation	93
Figure 5.2: Detecting triplet state molecules.	96
Figure 5.3: A typical time of flight measurement signal from the ion detector.....	98
Figure 5.4: The effect of the push beams.....	100
Figure 5.5: Schematic of intentionally lowering the lattice potential.....	102
Figure 5.6: Typical molecular lifetime data.....	105

Figure 5.7: Spectroscopy and population distribution of the $\alpha^3\Sigma^+$ state	107
Figure 5.8: K vs binding energy for molecules in specific vibrational levels.....	108
Figure 5.9: K vs E for atom-molecule and molecule-molecule collisions.....	111

List of Tables

Table 2.1: A summary of pressures over time for gas species relevant to bakeout. 37

Table 2.2: Summary of frequencies and AOM shifts used in the experiment. 44

Table 5.1: Calculated C_6 coefficients..... 111

1 Introduction

Atomic physics has been consistently striving to create colder samples of matter for the past thirty-five years. The colder an atomic sample is the cleaner it is for spectroscopic interrogation, which enables more precise optical clocks and general, measurements of all kinds. The impetus of this work is the creation of ultracold samples that have strong, tunable interactions. The extra degrees of freedom in such a system will allow a much richer landscape of experiments including applications with fundamental ramifications in ultracold chemistry¹, quantum simulation², and quantum computation³. Although there are many competing techniques for cooling polar molecules within the atomic, molecular, and optical physics community, in this work we focus on using optical traps to construct molecules from their constituent atoms.

As first noted in English by Gordon,⁴ a laser field is capable of exerting two kinds of forces on polarizable particles, the radiation pressure and dipole forces. The origins of these two types of forces will be investigated in detail, but it is worth noting that the two experimental traps used in this work derive from these two aspects of the force. If you use a three-dimensional laser field and add a suitable magnetic field gradient you can create a magneto optical trap⁵ (MOT) and if you simply focus a laser beam you can create the quasi-electrostatic trap or QUEST⁶.

1.1 History

Although the radiative force of light has been experimentally demonstrable since the early twentieth century, with the first atomic beam slowing experiments of any kind being realized in 1933 with a sodium lamp, the dawn of modern atomic physics is truly

with the advent of the laser. The coherent, intense light is perfect for light force experiments, and many contemporary physicists realized this fact. Multiple Russians proposed using the dipole force rather than the radiative force to trap atoms in 1960's. In 1978 Ashkin proposed using the momentum of light to slow atoms. Having read this proposal, 1979 Phillips and co-workers began experiments in slowing atomic beams with laser light using Zeeman cooling to effectively generate a one-dimensional force proportional to the atoms' velocity⁷. Ten years later, Chu and coworkers were able to create a highly viscous environment for a sample of Sodium atoms, using a three dimensional beam geometry, which was termed "optical molasses⁸" in the lab, thus marking an important step forward in the nascent field of atom trapping. They crucially showed that laser cooling was extensible to trapping in three dimensions within two years by demonstrating the MOT. They were able to trap 10^6 atoms with velocity profiles equivalent to temperatures of a few hundred μK . The MOT is a fantastic experimental tool, achieving phenomenally low temperatures with relative experimental ease, but it is limited to a handful of atoms in addition to a few promising types of molecules.

The very thing which makes polar molecules such a fruitful subject for investigation also dramatic limits our ability to confine it with any meaningful density. Molecules have multiple degrees of freedom, which result in multiple energy-level manifolds at vastly different scales. These levels result in many interesting physical properties, but make it difficult in general to find closed molecular transitions suitable for optical cooling. As a result, the array of technologies that have been developed in the atomic cooling and trapping community are not normally applicable to molecular

systems. Luckily, there is a much more general way to trap polarizable particles using laser light.

The other common way one can use a laser to confine a polarizable sample is via the optical dipole force. The first example of this force was utilized by Ashkin in his implementation of optical tweezers⁹ on dielectric beads. The advent of modern, far off resonant optical traps was in 1995 with the use of a CO₂ laser to trap first cesium atoms and then Cs₂ molecules.

1.2 Applications of Ultracold, Polar Molecules

The field of ultracold molecules has exploded since the beginning of the work in this thesis. Much like the nascent days of BEC, we are proceeding from experiments designed merely to create samples of molecules, to experiments with samples that actually use samples of ultracold molecules

1.2.1 Ultracold Chemistry

Because the molecules produced using the various techniques described above are so cold, they can provide unique insight into the fundamentals of chemical reactions. At temperatures in the tens of μK the details of molecular collisions can be observed. The molecules will still retain all of their extensive internal structure but if they are cold enough quantum effects may not be obscured by thermal collisions. This would enable the observation of low-binding energy many-body states such as field linked states¹⁰ or dipolar crystals¹¹ in an optical trap. These states would only be observable at ultracold temperatures due to their low binding energies relative to room temperatures.

The cold, dense nature of the molecular sample also opens up the possibility of performing detailed measurements of interesting aspects of chemical processes themselves. One can hope to observe tunneling during collisions or to measure reaction rates as a function of angular momentum in the sample. Because the molecules we create are strongly polarizable, one can look for changes in collision cross sections as a function of various parameters.

One obvious thing to vary would be the external electric field inducing the dipole moments in the molecules, to look for collisional resonances¹². Particularly interesting are predictions¹³ of huge collisional cross sections between ground state polar molecules, which if observed, would open up the possibility of evaporative cooling of molecules even at the relatively low available present densities of particles.

1.2.2 Quantum Computation

The original motivation for most of this work is the goal of creating a robust, scalable quantum computer¹⁴. Quantum computation is a field of intense interest due to its potential implementation of new algorithms for factoring large numbers¹⁵ and sorting certain classes of databases. Our proposed quantum computer would consist of single polar molecules confined within an optical lattice. Polar molecules are excellent candidates for use as qubits because they have very strong interactions due to their induced dipole moment, while still being relatively insensitive to their environment because of their being optically trapped. These relatively long coherence times coupled with strong interactions are two key desirables in any scheme for quantum computation. The speed of gate operations is proportional to the interaction strength between qubits, while the total number of gates performed is limited by the decoherence time.

It is important to clarify what we mean by “decoherence” in this case. This can be thought of as the amount of time on average it takes for the information contained in the qubit to be lost. In this implementation of the quantum computer the main source of decoherence would be inelastic scattering of photons from the optical lattice itself. Because the lattice is detuned far from any molecular resonance, these processes are relatively infrequent. This results in the expected long decoherence time.

This version of molecular qubits we would utilize the two lowest rotational states of the absolute electronic and vibrational ground state of the molecule. The qubit molecules would be located in an electrostatic gradient so that the resultant Stark shift would render each individual molecule spectroscopically addressable by a microwave pulse.

1.2.3 Quantum Simulation

A more recent hot area of the UCPM game is the idea of doing simulations of condensed matter systems with atomic physics experiments^{16,17,18}. Because the atomic experiments are much easier to fundamentally understand than complicated high- T_c solid state systems, the hope is that experimentalists will be able to simulate presently intractable Hamiltonians in the condensed matter physics world.

1.2.4 Precision Measurements

Ultra-cold molecules are a phenomenal subject for precision measurements.¹⁹ Since they have so many different degrees of freedom while still offering long interrogation times, they can be used for precision spectroscopy²⁰ at many different ranges of photon energies. Because UCPMs have so many different energy levels, they

are bound to have closely spaced levels from different electronic manifolds. These will typically have quite different binding energies and/ parities. Systems of this type are ideal for studying variations in fundamental constants²¹ because one is able to choose systems of levels where one frequency is expected to be highly sensitive to the physics in question, while another is not and can be used as a stable reference²².

The search for the electric dipole moment of the electron²³ is ongoing in a molecular sample to take advantage of the high induced electric field within the molecule. The current work could be improved upon with the greatly increased interaction times and spectroscopic precision offered by ultracold samples. A new proposal to do exactly this with ThO is under way²⁴.

1.3 Experimental Techniques for Producing Cold Molecules

The experiment described in this thesis utilizes the technique of photoassociation²⁵ to create polar molecules from a pair of different laser-cooled atoms. The resultant molecule is at a translational temperature of roughly the same order of magnitude as that of the cooled atoms, which is on the order of $100\mu\text{K}$. This method of creating molecules relies on the fact that its constituent atoms can both be efficiently laser cooled and trapped at relatively high (10^{13} cm^{-3}) densities. As a result, this technique, and any others that “assemble” polar molecules from ultracold atoms are essentially limited to producing polar bi-alkali molecules at present. Although there has been substantial progress in cooling exotic atoms such as Ytterbium²⁶ and alkaline earth elements²⁷, there have not yet been molecules formed from them. The details of the photoassociation technique are discussed in a later chapter.

1.3.1 Fano-Feschbach Association

The other main technique for assembling ultracold molecules from laser cooled atoms is to utilize a Fano-Feschbach resonance²⁸ to convert a sample of cold atoms into molecules wholesale²⁹. This can be done by starting with a dense sample of atoms and precisely sweeping a magnetic field to cross over into the first bound state of the molecular potential between the two atoms. This technique has been enormously successful in producing extremely dense and cold molecular samples.

1.3.2 Buffer Gas Cooling

Instead of assembling molecules from ultracold atoms, one can attempt to directly cool molecules by various methods. One way to do this is to take a solid chunk which contains some of the desired molecule and ablate it with a high powered laser in the presence of a buffer gas of cold atoms.

The molecules that are created by the ablating laser pulse collisionally thermalize with the buffer gas to reach a velocity spread equivalent to a temperature on the order of 1K³⁰. Once one has created a sample of cold molecules in a cold cell it is possible to trap them directly using a magnetic trap.³¹ One problem with this scheme is that the trap lifetime of the molecular sample is severely limited by collisions with the buffer gas. There is a workaround if one chooses molecules with sufficiently high magnetic moments to remain trapped in the presence of high throughput vacuum pumps. This enables long trap lifetimes, but limits which species can be used.

Rather than immediately trapping the molecular sample, one can extract it from the ablation chamber in the form of a cold molecular beam. Once the beam emerges from a hole in the wall of the cooling chamber it can be loaded into an electro- or

magneto-static guide. This arrangement has the dual advantage of preserving the generality of the buffer gas cooling technique while still separating the molecular sample from the contaminating buffer gas. The resultant guided pure molecular beam should be rotationally and translationally cooled to a temperature very close to that of the buffer gas. This is typically on the order of 0.5-5 K depending on the specifics of the experiment.

Although buffer gas cooling is a fantastic technology, it has some drawbacks as well. In order to use a magnetic trap³², one must employ weak field seeking states of the cooled molecules. This is by definition not the ground state of the molecule, which holds the most interest for applications. The molecules produced in a buffer gas cell are cold, but still three or more orders of magnitude hotter than those produced by the “atomic assembly” techniques. This limits the available trapping techniques to these same superconducting magnetic traps and all the inherent problems.

1.3.2 Stark Deceleration

The other widely used method of directly cooling molecular samples is to shift their velocity distribution using AC electric fields. A typical Stark-deceleration experiment³³ begins with a conventional molecular beam that is rotationally cold due to supersonic expansion through a nozzle. The beam is translationally at room temperature at typical speeds of a few hundred meters per second. A molecular packet is then injected into a series of closely spaced electrodes which are the actual decelerator.

As the packet flies through the first pair of electrodes they are incident on a spatially varying inhomogeneous field that increases as they approach the point between the electrode tips. The molecules are selectively prepared to be in a weak-field seeking

state, so that this field arrangement will be a potential barrier. If the electrodes are rapidly switched off precisely as the desired subset of molecules reach the point of field maximum, the molecules are in a field-free state and have lost some fraction of their translational kinetic energy by converting it to potential energy. An actual decelerator utilizes many stages of electrodes and rapidly switches them while being careful to continually address the same subset of the molecular packet. In this way, a spatially filtered subset of the original wave packet with a narrow velocity distribution is produced.

Current deceleration efforts are limited to velocity distributions equivalent to temperatures of roughly 1K. Although these are fairly high temperatures, decelerated molecules can nevertheless be loaded into electrostatic or permanent magnetic traps. There has been extensive work done on studying molecular collisions magnetic traps³⁴, and sympathetic cooling with MOTs³⁵. Although a variety of molecules³⁶ have been decelerated using this technique, it is nowhere near as general as buffer gas cooling. This is due to the fact that any molecule which one would like to decelerate must have a weak-field seeking ground state and should also be as light as possible, to maximize the amount of kinetic energy removed per stage. Furthermore, although work is ongoing, it seems that there is a fundamental limit to how cold decelerators can make a molecular sample. At very slow speeds each of the last few stages of the decelerator removes a relatively large percentage of kinetic energy. This results in a fundamental lower limit of the molecule temperature because there is still a velocity distribution. Some molecules become “over focused” and don’t reach the same speeds as their peers

2. Trapping and Cooling Atoms

The underpinning for all of the work on this experiment is the cooling of atoms by laser light. In this chapter we will lay out a simple theory for laser cooling and trapping, show how we apply these simple ideas to actual atoms, and then describe the entire experimental setup in detail.

2.1 Laser Cooling

The fundamental tool in atomic physics experiments is the laser and this experiment takes advantage of both ways a laser beam can produce a force. We will briefly derive the light force since it is the essential physical basis for trapping both atoms and molecules in our experiment.

2.1.1 The Light Force

Following Cohen-Tannoudji we can write a Hamiltonian for the combined atom and incident radiation field system including translational degrees of freedom. We have

$$H = \frac{P^2}{2M} + H_A + H_R - \mathbf{d} \cdot \mathbf{E}_e(\mathbf{R}, t) + E_{\perp} , \quad (2.1)$$

where M and \mathbf{P} are the mass and momentum of the atom. The Hamiltonian of the atom and incident field are included as H_A and H_R respectively. The atomic dipole \mathbf{d} interacts with the external electric field \mathbf{E}_e . Finally, E_{\perp} is the radiated field of the atom. Note that both the external and radiation field are evaluated at the center of mass of the atom,

located at a position R . We can write the Heisenberg equations of motion for the Hamiltonian as follows:

$$\dot{R} = \frac{\delta H}{\delta P} = \frac{P}{M}. \quad (2.2)$$

$$\dot{P} = M\ddot{R} = -\frac{\delta H}{\delta R}. \quad (2.3)$$

Evaluating (2.3) we have

$$\dot{P} = \sum_{j=x,y,z} d_j \nabla_{\mathbf{R}} [E_{e_j}(\mathbf{R}, t) + E_{\perp j}(\mathbf{R})]. \quad (2.4)$$

Taking the expectation value of both sides of the equation with respect to a time-independent Heisenberg state ket (averaging over the atomic wavepacket), we have the Ehrenfest relation for our particular Hamiltonian:

$$M \langle \ddot{\mathbf{R}} \rangle = \sum_j \langle d_j \nabla_{\mathbf{R}} [E_{e_j}(\mathbf{R}, t) + E_{\perp j}(\mathbf{R})] \rangle. \quad (2.5)$$

In order to evaluate this equation we will introduce two approximations. First, we will assume that the atomic wave packet is confined to a much smaller spatial extent than the incident field. This follows from the fact that the atom or molecule has a finite mass and as a result its De Broglie wavelength $\lambda_{DB} = \frac{h}{Mv}$ is much smaller than the wavelength of the incident radiation field. Because we can consider our quantum mechanical wave packet to be a particle with finite spatial extent, we can substitute all instances of the operator \mathbf{R} in (2.5) with its average value. If we define the center of the wavepacket as \mathbf{r}_G then we can write $\langle \mathbf{R} \rangle = \mathbf{r}_G$ and are left with the expression

$$M\dot{\mathbf{r}}_G = \sum_{j=x,y,z} \langle d_j \rangle [\nabla_{\mathbf{R}} E_{e_j}(\mathbf{r}_G, t) + \nabla_{\mathbf{R}} E_{\perp j}(\mathbf{r}_G)]. \quad (2.6)$$

The term $\nabla_{\mathbf{r}} E_{\perp j}(\mathbf{r}_G)$ is the force on the atom by the gradient of the radiation field at \mathbf{r}_G .

It can be shown that this contribution is even in \mathbf{r} , so that its gradient at the origin is zero and the term can be eliminated. As a result we have the final equation

$$M\dot{\mathbf{r}}_G = \sum_{j=x,y,z} \langle d_j \rangle \nabla E_{e_j}(\mathbf{r}_G, t). \quad (2.7)$$

The right hand side of this equation is the force as a function of driving field on the center \mathbf{r}_G of the atomic wavepacket. Recognizing this interpretation, we can also infer from the lack of gradient-contribution shown above that the average force on an atom by its own field is zero.

The second approximation is that internal processes in an atom occur on a much faster timescale than external processes. The natural time scale for an internal process is $T_{int} = \Gamma^{-1}$, where Γ is the transition rate between the two states in question. To buttress this assumption we will consider atoms of velocity v that are moving very slowly with respect to the scale on which the incident light field varies. That is to say, we will take the distance $vT_{int} \ll \lambda$. Where λ is the wavelength of the incident radiation. We must introduce one additional point because in laser cooling we have variations in the velocity over external timescales $T_{ext} = \hbar/E_{rec}$ with E_{rec} is the atomic recoil energy defined to be $E_{rec} = \hbar^2 k^2 / 2M$. When an atom initially at rest absorbs (emits) a photon $k\varepsilon$ it gains (loses) E_{rec} . Note that for commonly considered (allowed) cooling transitions we still maintain $T_{int} \ll T_{ext}$ because these transitions satisfy the relation $\hbar\Gamma \ll E_{rec}$. The end result of this second approximation is that the average dipole $\langle d \rangle$ reaches a steady state before the center of the atom (\mathbf{r}_G) has moved due to the force described in equation (2.7).

Now we need to consider the field interacting with our atom at the origin with magnitude E_0 and frequency ω_L . We can write it as

$$E_e(\mathbf{r}, t) = \mathbf{e}E_0(\mathbf{r}) \cos[\omega_L t + \phi(\mathbf{r})]. \quad (2.8)$$

Assuming that the polarization does not depend on \mathbf{r} and choosing a time such that $\phi=0$, we can write the field as

$$E_e(0, t) = E_0 \cos \omega_L t. \quad (2.9)$$

Using (2.9) we can write (2.7) as

$$\nabla E_{ej} = e_j \cos \omega_L t \nabla E_0 - \sin \omega_L t E_0 \nabla \phi, \quad (2.10)$$

where all gradients as well as E_0 are evaluated at the origin, e.g. at $\mathbf{r} = 0$. Invoking the rotating wave approximation and following the standard breakdown of the Bloch vector into three components u , v , and w . We can write the steady state solution of the optical Bloch equations with these variables as

$$u_{st} = \frac{\Omega^2}{2} \frac{\delta_L}{\delta_L^2 + (\Gamma^2/4) + (\Omega^2/2)}, \quad (2.11)$$

$$v_{st} = \frac{\Omega^2}{2} \frac{\Gamma/2}{\delta_L^2 + (\Gamma^2/4) + (\Omega^2/2)}, \quad (2.12)$$

$$v_{st} = \frac{\Omega^2}{4} \frac{1}{\delta_L^2 + (\Gamma^2/4) + (\Omega^2/2)} - \frac{1}{2}, \quad (2.13)$$

where Ω is the Rabi frequency, Γ is the spontaneous emission rate and $\delta_L \equiv \omega_L - \omega_0$ is the detuning between the incident field ω_L and the atomic frequency ω_0 . The physical interpretation of these equations is that The average value of the dipole moment operator can be written in terms of u_{st} and v_{st} as

$$\langle d_j \rangle = 2(\mathbf{d}_{ab})_j u_{st} \cos \omega_L t - v_{st} \sin \omega_L t . \quad (2.14)$$

Now we use (2.14) and (2.10) and insert them in expression(2.7). Then we average over a single optical period to recover an equation that describes the mean radiative force

F acting on the atom

$$F = \sum_j \overline{\langle d_j \rangle \nabla E_{e_j}} = e_j \cdot \mathbf{d}_{ab} u_{st} \nabla E_0 - v_{st} E_0 \nabla \phi , \quad (2.15)$$

which reveals the two types of optical forces acting on an atom. These are conventionally split up into the reactive or dipole force

$$F_{dp} = e_j \cdot \mathbf{d}_{ab} u_{st} \nabla E_0 , \quad (2.16)$$

which is proportional to the amplitude gradient of the driving field and the dissipative, or radiation pressure force

$$F_{rad} = e_j \cdot \mathbf{d}_{ab} v_{st} E_0 \nabla \phi , \quad (2.17)$$

which is proportional to the phase gradient of the field. At this point it is clear that a strong dipole force requires a large field gradient, while all the radiation pressure force requires is a phase gradient. We will leave discussion of the dipole force to its relevant chapter and concentrate on the radiation pressure force in laser cooling.

2.1.2 1-D Doppler Cooling and Optical Molasses

The preceding expressions for the light force were derived for an atom at rest. In order to investigate optical cooling, we must now consider our atom moving at a constant velocity v in a single frequency running wave. Treating our system as one dimensional along a plane defined by the coordinate z , and still working in a semi-classical regime we must rewrite the incident field (2.9) as

$$E_e(z, t) = E_0 \cos(\omega_L t - \mathbf{k} \cdot \mathbf{v}t). \quad (2.18)$$

The atom now undergoes a time-dependent phase due to the Doppler shift. The previously noted steady state solutions to the optical Bloch equations are still valid under this incident field with the substitution $\delta_d = \delta_L + \mathbf{k} \cdot \mathbf{v}t$. This substitution also propagates through to the expression for F_{rad} yielding the expression

$$F_{rad}(\mathbf{v}) = \hbar \mathbf{k} \frac{\Gamma}{2} \frac{\Omega^2/2}{\delta_d^2 + \Gamma^2/4 + \Omega^2/2}. \quad (2.19)$$

If we consider velocities such that $\mathbf{k} \cdot \mathbf{v} \ll \Gamma$ we can expand to lowest order in v to find

$$F_{rad}(\mathbf{v}) = F_{rad}(\mathbf{v}=0) - \eta \mathbf{v}, \quad (2.20)$$

with

$$\eta = -\hbar k^2 \frac{\Gamma}{2} \frac{\delta_L \Omega^2/2}{\left[\delta_L^2 + \Gamma^2/4 + \Omega^2/2 \right]^2}. \quad (2.21)$$

The second term in equation (2.20) is a friction force that depends on the detuning from the atomic resonance. The atom sees a field propagating in the direction opposing its motion shifted to a higher frequency than one opposing its motion because of the Doppler shift. As a result, if consider the case of an incident field with red detuning at rest $\delta_L < 0$ a beam opposite the direction of motion would be shifted closer to resonance, while a beam traveling in the same direction would be shifted further away. If we consider two counter-propagating ($\mathbf{k} = +k \mathbf{z}$ and $-k \mathbf{z}$) beams weak enough that they can be treated independently the final resultant force on an atom would be³⁷

$$F_{rad}(\mathbf{v}) \approx -2\eta \mathbf{v}. \quad (2.22)$$

This is a true cooling force, because in the case of opposing standing waves we can take a spatial average that eliminates $F_{dissip}(v=0)$ in (2.20), so that atoms in counter-propagating traveling waves do have their velocity distributions narrowed.

It is possible to arrange three pairs of mutually-perpendicular beams to create a region in space where an actual atomic sample could have its velocity distribution narrowed, and its motion strongly damped in a three dimensional optical molasses. Although atoms in such an arrangement would have their velocity distribution narrowed, which is by definition cooled, they are still not confined. Atoms will leave the cooling region eventually via a random walk from the momentum transfer of $\hbar\mathbf{k}$ associated with the recoil energy lost on emission. In order to trap as well as cool an atomic sample it is necessary to add a magnetic field.

2.1.3 The Magneto Optical Trap

We can begin a simple model of the MOT with the familiar 3-D molasses configuration of three orthogonal pairs of beams that interact weakly enough with an atom that they can all be considered independently. Additionally, we specify that each pair of counter-propagating beams must also be circularly polarized (σ^+ and σ^-) in opposite senses from each other. We will now consider a toy atom traveling only in one of these dimensions, along which we will define the z-axis. We will assign our model atom a total electron spin $J=0$ in the ground state and a $J=1$ excited state with three degenerate magnetic sub levels $M_J = -1, 0, +1$. Now we red-detune the beams and we cool our atom in one dimension as in the previous section.

Now we will turn on a linear magnetic field $\mathbf{B} = B_0 z \hat{z}$, that induces a Zeeman shift $\pm Bz$ where if we define z such that the σ^+ beam travels in the $+z$ direction. The total detuning is now³⁸

$$\delta_{\pm} = \delta_L \mp \mathbf{k} \cdot \mathbf{v}t \mp \mu_B Bz, \quad (2.23)$$

where δ_{\pm} is the shift of the $M_J = \pm 1$ levels. The shift, and therefore the total Doppler force, is spatially dependent and increases in magnitude the further from the $z=0$ the atom travels. The system is shown with massively exaggerated shifts for clarity in Figure 2.1.

Selection rules hold that σ^- (σ^+) photons connect the $J=0$ state with the $J=1, M_J=-1$ ($+1$) state. So if the atom starting from $z=0$ is traveling in the $+z$ direction its $M_J=-1$ level will be shifted closer to resonance with the σ^- light field and its $M_J=+1$ level will be further from resonance with the σ^+ light field. As a result it preferentially absorbs the σ^- light and feels a net force opposing its motion until it is pushed back to $z=0$. The system behaves exactly like an over-damped harmonic trap that cools the atoms in its range of capture and can easily be generalized to a three dimensional trap using anti-Helmholtz coils.

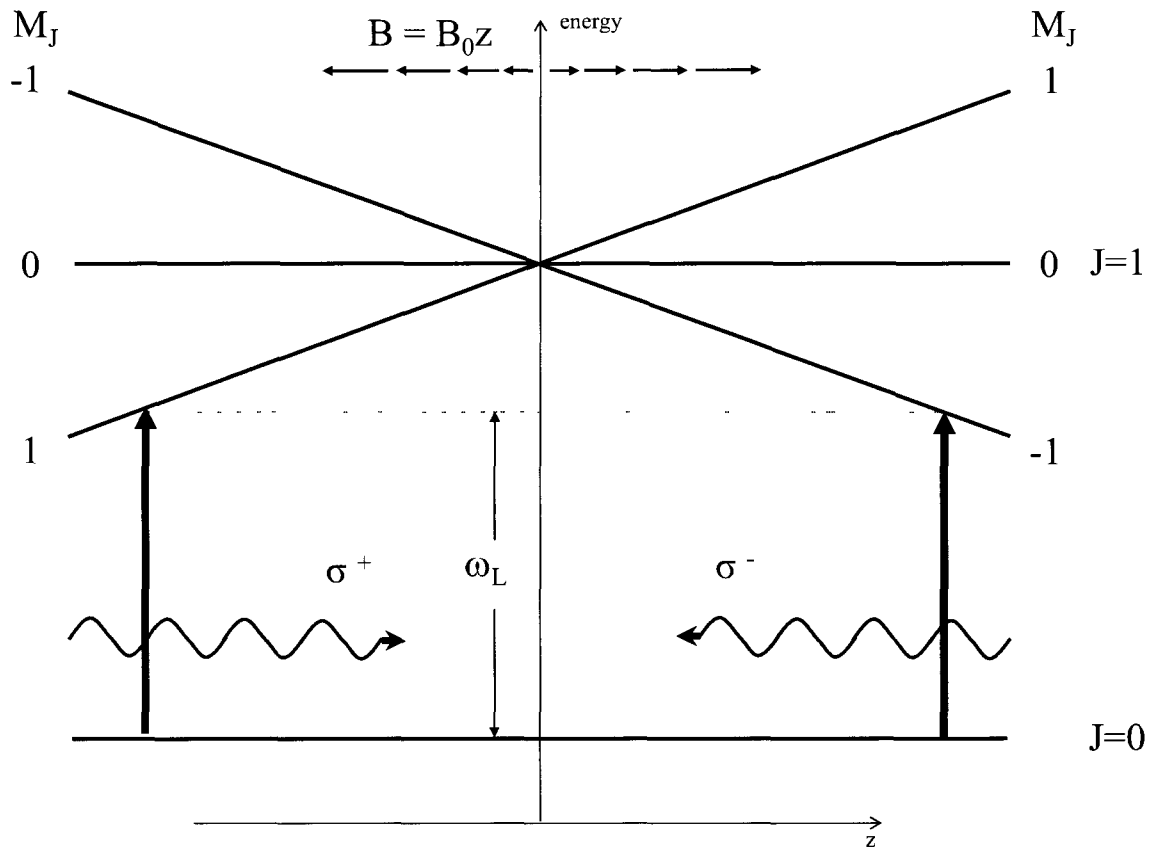


Figure 2.1: A summary of the 1-D MOT model. State selection rules for magnetic sublevels selectively shift photons traveling in the direction opposite of the atom's motion closer to resonance. This preferential scattering results in a net force opposing this motion and traps the atom.

2.2 Trapping and Cooling Actual Rubidium and Cesium Atoms

Trapping and cooling actual Alkali atoms is more involved than our toy model. rubidium and cesium have nuclear spins $I = 5/2$ and $7/2$ respectively, which means we must take the hyperfine interaction into account when examining the energy levels of our trapping scheme. Including the hyperfine interaction means J is no longer the total angular momentum and we must use $F=I+J$ instead. For our atoms this yields the specific level structures shown in figure 2.2.

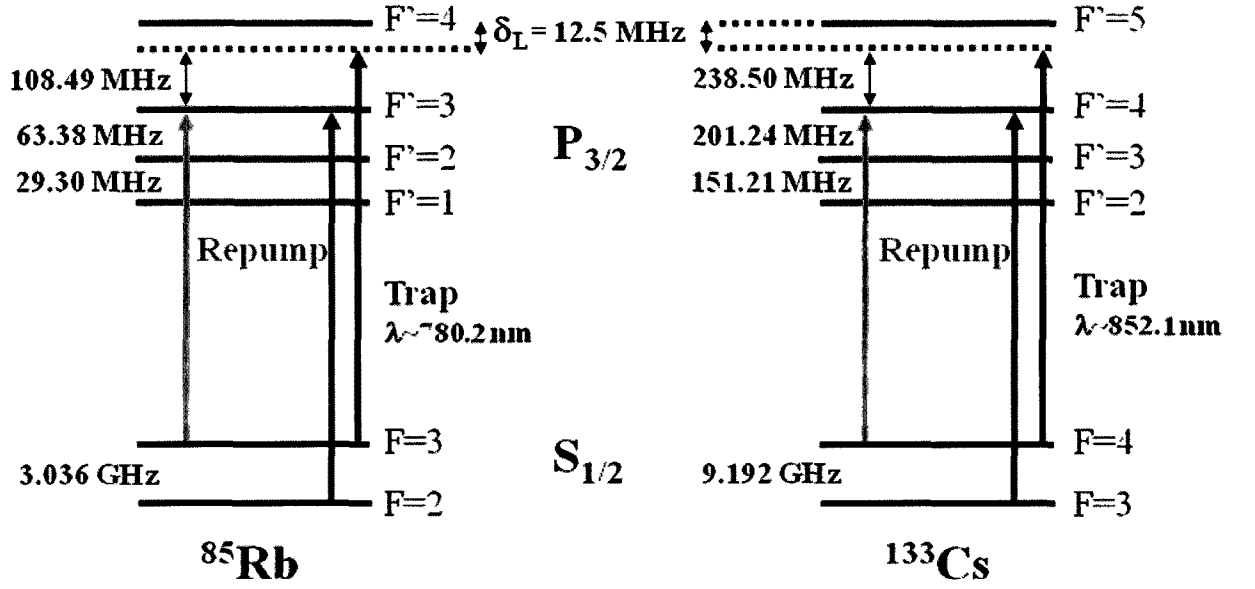


Figure 2.2: Schematic representation of the actual levels used to experimentally trap and cool Rb and Cs. The relevant splittings are labeled.

When σ^\pm laser light is incident on an actual alkali atom it tends to drive the atom into the $|F = F_+, M_F = \pm F\rangle$, where $F_+ = I + \frac{1}{2}$. This state only has allowed transitions to $|F' = F + 1, M_F = \pm F \pm 1\rangle$. As a result cooling lasers must be tuned to $F \rightarrow F' = F + 1$ transitions in order to ensure the repeated cycling that laser cooling and trapping requires. In our case we red-detune the trapping lasers to transitions between the $5S_{1/2}, F = 3 \rightarrow 5P_{3/2}, F' = 4$ levels in rubidium and the $6S_{1/2}, F = 4 \rightarrow 6P_{3/2}, F' = 5$ levels in cesium. Since the trapping light must be red detuned and the detuning roughly $\sim 10\%$ of the excited state hyperfine splitting there is a significant possibility of off-resonantly exciting to the $F' = F_+$ level. From here the atom is free to spontaneously decay into the lowest hyperfine level of the ground state with $(F = F_- = I - \frac{1}{2})$ which, due to its relatively large splitting, is off-resonant or “dark” to the trapping light. A second beam tuned to the $F_- \rightarrow F' = F_- + 1$ transition ($F = 3 \rightarrow F' = 4$ in Cesium and $F = 2 \rightarrow F' = 3$

transition in Rubidium), known as the repump is added to trapping scheme to overcome this problem. The repump transfers population from the lower to the upper ground state hyperfine level via the $F' = F_+$ level. This creates a closed level scheme that functionally imitates the key points of our toy model and allows atoms with such schemes to be cooled and trapped.

The key parameter to maximize in the MOTs for our experiments is density (for reasons that will be discussed in chapters 3 and 4). The maximum density of the MOT is limited by a repulsive force between atoms caused by the absorption of spontaneously emitted trap photons. As the MOT becomes denser there is a correspondingly increased probability of reabsorption of these spontaneous photons due solely to the increased number of atoms. The maximum density is the point at which the trapping force of the MOT balances this repulsive force. This limit can be overcome by adding a third beam to our cooling scheme.

This beam is referred to as the “depump” and is tuned to the $F_+ \rightarrow F' = F_+$ transition ($F = 4 \rightarrow F' = 4$ in cesium and the $F = 3 \rightarrow F' = 3$ transition in rubidium). A hole in the collimated repump beam is imaged onto the MOT and then filled with the depump beam. This creates a small region within the MOT that has no repump light, allowing the atoms in this region to remain in the dark lower hyperfine state. Because the required off-resonant scattering transitions are relatively infrequent, the depump is inserted into the system to actively drive the atoms in the center of the MOT into a nearly dark state. Typically the depump intensity is $\sim 10\%$ of the repump intensity, but this is an adjustable parameter that must be optimized empirically. We do not want a completely dark MOT center, because we want to maintain the net trapping force so that the density

increases. Without some repump light there is no confining force within the dark region and there will be negligible gain in the atomic density.

2.2.1 Loading Techniques

The apparatus was designed with three ways to load the MOTs. The backup method was loading from a small amount of background Rb and Cs vapor provided by a pair of “cold fingers”. The cold fingers are two valved-off, temperature controlled ampoules filled with roughly a gram of alkali metal each. When the valves are opened to the chamber the partial pressure of each of the species can be regulated by tuning the temperature of the ampoules. The extreme low-velocity tail of the room-temperature alkali released into the chamber in this way is in the MOTs. The second way to load the chamber was two pairs of SAES alkali metal dispensers.

These dispensers are simply mounted on a pair of feedthroughs roughly facing the chamber center. They are wires with an active region that contains an alkali chromate combined with another material that serves as a getter. The dispensers are relatively inert at room temperature, although they are susceptible to degradation if they are in contact with atmospheric water vapor for more than 24 hrs. For this reason we store them under a modest vacuum. When 4 Amps of current is run through the getters they heat up to roughly 700 °C and emit Rb or Cs along with trace contaminants into the chamber. At 4.5 A the dispensers provide a background vapor pressure of roughly $2(10^{-9})$ torr, which results in MOT loading times on the order of 3 seconds ($1/e$ time ~ 1 s). This level of background pressure is acceptable for experimental operation, but must be monitored carefully when using ion detection as will be discussed in Chapter 4. Although the getters are highly controllable, they are fundamentally limited by their thermal operating

process. This gives them a characteristic response time of ~ 1 sec, which is far too slow for true pulsed loading.

The original idea for efficient pulsed loading of the MOTs was light induced atomic desorption (LIAD³⁹) of Rb and Cs atoms from the surface of the vacuum chamber. In order to appreciate the potential gains using this loading technique we will first review the loading dynamics of a two-species MOT.

Rubidium atoms are loaded into a MOT at a rate R_{Rb} , which is a complex function of many experimental parameters including laser intensity, trapping region volume, atomic partial pressure, and light scattering rates. The rate equation governing the total number of atoms N_{Rb} in a Rb MOT is

$$\frac{dN_{Rb}}{dt} = R_{Rb} - N_{Rb} \left(\frac{1}{\tau_b} + \frac{1}{\tau_{Rb}} + \frac{1}{\tau_{Cs}} \right) - \int_{MOT} (K_{Rb,Rb} n_{Rb}^2 + \frac{1}{2} K_{Rb,Cs} n_{Rb} n_{Cs}) dV - \Gamma_{additional}, \quad (2.24)$$

where $1/\tau_b$, $1/\tau_{Cs}$, and $1/\tau_{Rb}$ are the background gas collision rate, the untrapped Cesium-only collision rate, and the untrapped Rubidium-only collision rate respectively. The intraspecies two-body loss rate is $K_{Rb,Rb}$ while the interspecies two-body loss rate is $K_{Rb,Cs}$. These two values are for unit atomic density, so we multiply by the atomic densities n_{Cs} and n_{Rb} . The integral is over the MOT volume and the terms within it all refer to their respective values in the MOT. Finally, $\Gamma_{additional}$ is a catchall term that encompasses all other loss rates. Note that the equivalent equation governing the total number of Cesium atoms in a MOT is the same with the subscripts Rb and Cs reversed. The rate equation (2.24) can be solved by

$$N_{Rb}(t) = N_{Max} \left(1 - e^{-\frac{t}{\tau_{MOT}}} \right), \quad (2.25)$$

where

$$\frac{1}{\tau_{MOT}} = \frac{1}{\tau_b} + \frac{1}{\tau_{Rb}}, \quad (2.26)$$

and

$$N_{Max} = R_{Rb} \tau_{MOT}. \quad (2.27)$$

For conventional vapor cell MOTs loaded from background gas $1/\tau_b = 1/\tau_{Rb} = 1/\tau_{Cs}$ and the loading time is equal to the lifetime of the MOT. The basic idea behind LIAD is to maintain very low background collision rates while being able to load more atoms more quickly than the background rate would normally allow. If $1/\tau_{Rb} \gg 1/\tau_b$, as is the case when during LIAD, then the loading rate and atom number are only functions of the local partial pressure of Rubidium at the trap center. Once N_{Max} is reached, LIAD can be stopped and the MOT lifetime will be governed by the loss mechanisms described in (2.24). Our experimental duty cycle is loading-time limited by an order of magnitude, so any gains that could be made would have enormous practical value.

Most LIAD experiments are usually performed in coated- or uncoated- glass cells⁴⁰ that have been thoroughly saturated with alkali metal. The typical glass cell experiment begins with a base cell pressure of 10^{-10} torr and heats alkali dispensers for 15 minutes while keeping the pressure below 10^{-9} torr. The chamber pressure is then allowed to recover to its initial value over night and the experiment is performed. A high intensity (100 mW +) LED array or flash lamp is used to irradiate the cell while monitoring the total number of atoms in a MOT. LIAD typically increases the total number of loaded atoms by two orders of magnitude, which indicates a similar increase

in the local vapor pressure in the trapping region. The physical process of desorption involves using a high-energy photon to overcome a surface potential that holds an atom on the cell wall. For this reason UV photons are much more efficient at inducing LIAD than white light sources. Although there are reports⁴¹ of successful implementation of LIAD in stainless steel chambers, we were concerned about the lack of available optical access for illuminating the chamber. To increase the effective fraction of the surface area we could hit with diodes we used custom made quartz light pipe feedthroughs that had 1" diameter quartz plates affixed 1" from their ends. The plates were designed so that they allowed the UV light to spread out and hit more surface area of adsorbed alkali.

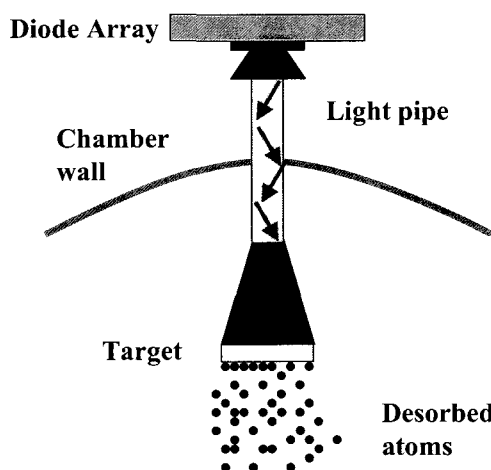


Figure 2.3: Schematic representation of the light pipe assembly used to maximize LIAD loading. A UV diode array outside of the vacuum chamber is placed as close as possible to the end of a quartz light pipe feedthrough. The light from the diode travels down the light pipe into vacuum, where it diverges into the chamber. A target is placed 1" from the end of the light pipe to take advantage of the increased area of the UV beam. The target, precoated with alkali atoms, emits the atoms toward the trapping region when the light hits it.

The targets were placed as close as possible to the trapping region and fastened to the light pipes with stainless steel collars. Although we experimented with projector lamps as white light sources, in the end we found the most effective source to be a 350 mw UV

(Optotechnology “Shark” 370 nm center wavelength) diode array mounted on the end of each light pipe.

In our experimental test we followed the technique of the Toronto group⁴² and ran on our alkali dispensers at 4 Amps for a period of 24 hours in an effort to thoroughly coat the inside of the chamber and quartz targets. This had the effect of raising the background pressure in the chamber to $6(10^{-9})$ torr without the dispensers on the entire next day. We loaded a small ($N = 2(10^6)$) Rubidium MOT from this background and monitored the total number of atoms through fluorescence. This relatively small MOT was necessary to quantify the effect of LIAD on our system. The total atom number vs. loading time with and without LIAD is shown in Figure 2.3. Although LIAD resulted in a marked improvement in loading characteristics, it falls far short of the desired two-order of magnitude improvement. These loading parameters were not sufficient for our system and we typically loaded from background gas generated by the dispensers for this reason.

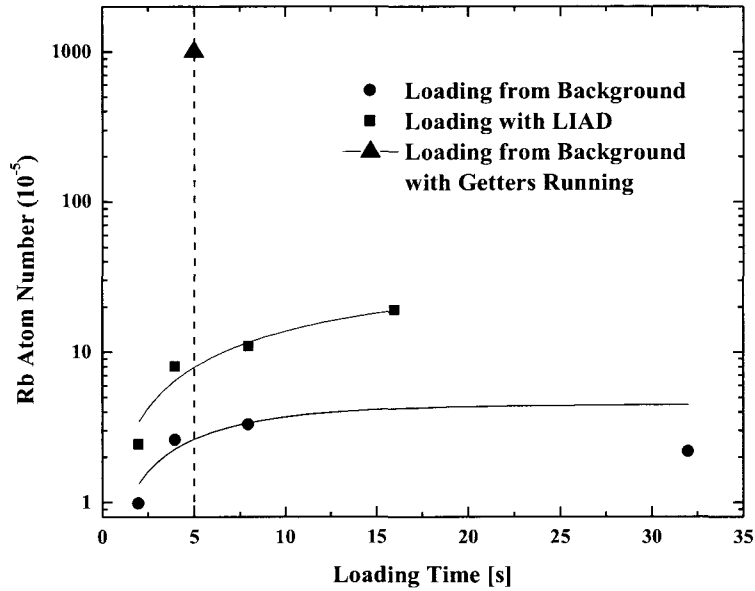


Figure 2.4: Typical results of loading via LIAD in a large stainless steel chamber with relatively limited optical access for desorption light. The blue triangle shows the typical operating regime for experiments, which was achieved by running 4-4.5 A through the getters. The blue dashed line is the longest loading time at which experiments were performed. Although LIAD does make a factor of 2 difference in the fitted exponential loading rate, the total number of loaded atoms is two orders of magnitude lower than the necessary operating level.

There are two main sources for the failure of LIAD in our vacuum chamber configuration. One is the relative lack of solid angle addressed by our UV light even with the feedthroughs and targets. Additionally, unlike glass cell experiments, the targets are positioned relatively far away from the trapping region. The true problem with this layout is the pumping action of stainless steel. The chamber itself acts as a strong getter of alkali, and in addition to being adsorbed as expected the alkali atoms are eventually pumped into the steel. This is the empirical reason behind the massive atom number drop shown in the inset of figure 2.3. We tried running the getters at 6A (chamber pressure $\sim 10^{-8}$ torr) for a full day in order to overcome this stainless pumping limit, even this drastic measure was insufficient to coat the chamber. This finding is consistent in that it

takes roughly a week to build up enough background pressure to load a MOT with cold fingers, which suggests that a constant vapor pressure of 10^{-8} torr in addition to constant contact with a macroscopic reservoir is needed to counteract the effect of the stainless. In the end we have too much stainless steel, not enough glass, and too little optical access for the UV light to allow LIAD MOT loading to be effective in our system.

2.2.2 MOT Diagnostics

We measure the number of atoms in the MOT by fluorescence imaging. This requires switching off the depump beams along with the use of an additional repump beam to fill in the dark spot MOT. To maximize the signal all of the trapping beams are tuned to resonance and the fluorescence given off by the MOT is captured with a photodiode. In order to get an accurate count of the atoms it is important to empirically verify that the atomic excitation is saturated. We do this by manually changing the trap light intensity and verifying that the fluorescence signal saturates. This procedure ensures that every atom sees enough light to be strongly saturated. As a result half of the atomic population is by definition in the excited state and the fluorescence rate per atom is given by $\Gamma/2$ where Γ is the natural line width of the trapping transitions. Under these conditions the total atom number N can be expressed as

$$N = \frac{2I^2 R \lambda}{hc\Gamma} \frac{4\pi}{d\Omega}, \quad (2.28)$$

where I is the current in the photodiode with resistance R , λ is the wavelength of the fluorescent light, and $d\Omega/4\pi$ is the solid angle subtended by the active area of the photodiode. For the transitions we use these Γ is 6 MHz for Cesium and 5.2 MHz for

Rubidium. We typically find $N \sim 10^9$ atoms in the MOTs using this method. Note that the solid angle is calculated by measuring the distance from the photodiode to the MOT, but the calibration of the detection optics takes a bit of care. To ensure that the MOT fluorescence is being detected instead of scattered light, we maximize a differential signal on the detector by switching the magnetic field on and off while adjusting the positions of the detector and any intervening optics.

For our experiment the primary MOT diagnostic tool is absorption imaging, which is used to maximize the density, the spatial overlap of the two species, and the temperature of the atoms. Because we ultimately wish to load an optical lattice that is much smaller than the spatial extent of even a dark MOT, we are much more concerned with density than atom number or specific loading characteristics provided all other parameters have reasonable values.

The density is measured by shining two orthogonal tunable beams near the trap resonances through the atoms and onto CCD cameras. These beams must be tunable to avoid saturation effects on the measurement and weak enough to exert a negligible force on the MOTs during imaging. We image the shadow of the MOT directly onto the CCD active area with lenses arranged with one of the images set a double magnification for diagnostic purposes. We calculate the atomic density in the MOTs by assuming that the distribution of the atoms in the MOT is Gaussian in each dimension. In this case the transmitted intensity through the cloud is

$$I = I_0 \exp\left[-\sqrt{\frac{\pi}{\ln 2}} n_p \sigma_{abs} \omega_0 \left(\frac{1}{1 + \frac{4\delta_L^2}{1^2}}\right)\right], \quad (2.29)$$

where n_p is the peak density in the atomic sample and ω_0 is the full width at half maximum of the sample in the absorption beam direction. In this case δ_L refers to the absorption beam's detuning from resonance while Γ still refers to the natural line width of the trap transition. The absorption cross-section σ_{abs} is given by⁴³

$$\sigma_{abs} = \frac{\lambda^2}{2\pi} \frac{2F'+1}{2F+1} \frac{\gamma_p}{\gamma_{tot}}. \quad (2.30)$$

Because we are using trapping light on resonance we are working with a so-called closed transition, for which the partial width of the transition γ_p is equal to the total transition width γ_{tot} . The absorption cross sections for Rubidium and Cesium are $1.25 \times 10^{-9} \text{ cm}^2$ and $1.41 \times 10^{-9} \text{ cm}^2$ respectively.

The density is measured by completely loading the MOT for roughly 5 seconds, then switching off the trap light, the depump, and the repump. After a 50 μs delay to ensure that there is no light remaining in the chamber the fill in beams are switched on for 50 μs and then the absorption light is switched onto the now-bright MOT immediately for 20 μs . The two-2D shadows of the MOT are acquired through Mightex CCD cameras reading out to PCI cards. The MOT images are viewed in real time using a Labview program that subtracts the current image from a static background created by switching the magnetic field off prior to an imaging run. This procedure generates a measure for I/I_0 but is by no means a sophisticated or ideal setup, as it requires re-zeroing every few minutes as the images quickly degrade due to vibration noise on the optics steering various beams and vignetting in the basic imaging optics.

The final density is obtained by fitting the density profile of the cloud to a Gaussian to obtain a value of ω_0 to pair with the measured I/I_0 . Although it is possible to

shine combined absorption beams onto the overlapped MOTs, a much better measure of density and position can be found by using one color of absorption light at a time. In practice the background light generated by using both colors of absorption degrades both absorption signals without adding anything substantial to the process. In the normal process of optimizing the MOTs it is usually possible to increase the duty cycle of imaging from 0.2 Hz to roughly 2 Hz because the imaging sequence takes so little time that a negligible number of atoms are lost from the trap if the beams are turned on again immediately after imaging. It is vital to switch the MOT beams back on before a program loop finishes in Labview because there is a variable hardware delay in Labview on the order of hundreds of milliseconds that will allow the MOT to partially unload and skew the density measurements.

The normal procedure for optimizing the MOTs is to systematically tune optics for maximum density, while continually detuning the absorption beam to avoid saturating the CCD while still having enough signal to noise to generate a good Gaussian fit.

Typical absorption images obtained using the method described are shown in figure 2.4.

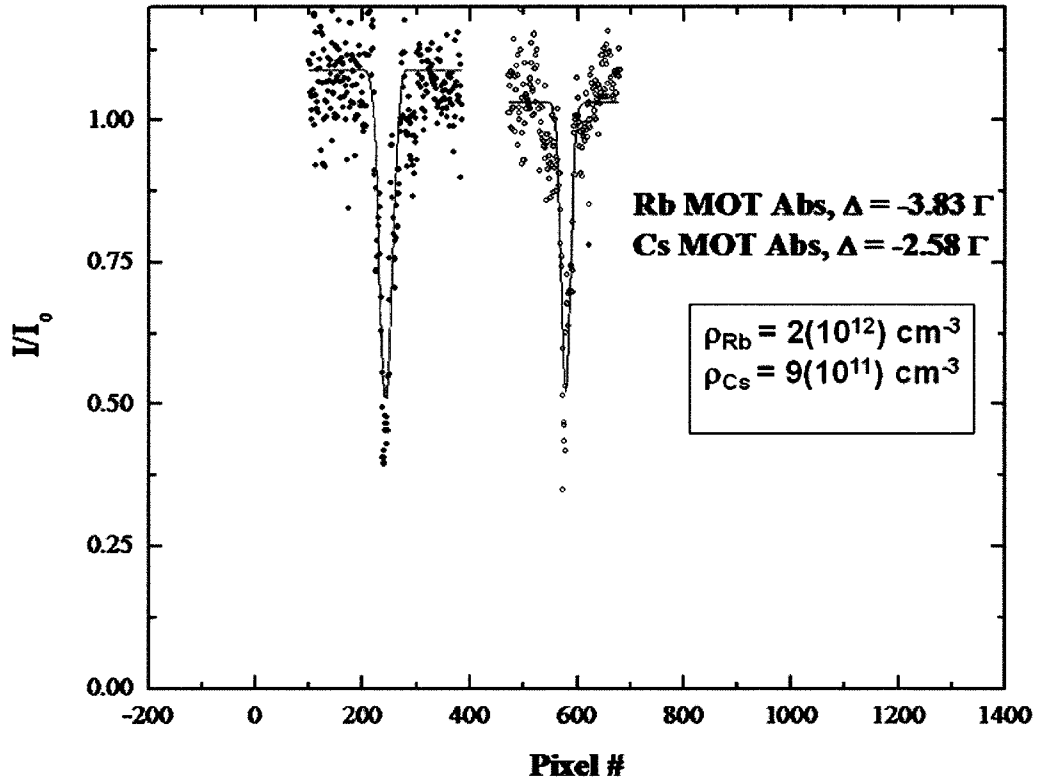


Figure 2.5: Typical results of an absorption measurement. Results for both atomic species are plotted, although they were not imaged simultaneously.

The final use of absorption imaging in the apparatus is to measure the temperature of the atomic sample. In the atomic cooling and trapping community the terms temperature and cooling have very specific meanings because a typical trapped sample of atoms is very far from both a thermal reservoir and equilibrium. What one can measure in atomic physics is the velocity distribution of a sample of atoms. Since we usually measure a velocity spread in one dimension we assume this spread has the form of a 1D Maxwell-Boltzmann distribution of the velocities centered at v_0 (typically 0 for our purposes)

$$f(v) = \frac{1}{\sqrt{2\pi\tilde{v}^2}} \exp\left(-\frac{(v-v_0)^2}{2\tilde{v}^2}\right). \quad (2.31)$$

This is related to the temperature of the atoms by the definition

$$\tilde{v} \equiv \sqrt{\frac{k_B T}{m}}. \quad (2.32)$$

Temperature in atomic physics is related to the spread in kinetic energy, so it follows that what is meant by cooling is the narrowing of the spread in a velocity distribution of a sample. The change in this spread can readily be measured using absorption imaging.

The temperature measurements are performed by adding a variable delay after switching off all MOT beams but before acquiring an image. This allows the atomic cloud of atoms with mass m to expand for a time t that can be related to the temperature of atoms in the MOT. We continue to assume that the MOT has Gaussian spatial and velocity distributions and can relate the width of the atomic cloud before (w_0) and after expansion (w) by

$$T_{atoms} = \frac{m}{4k_B t^2} w^2 - w_0^2 \quad (2.33)$$

The typical expansion times we use are up to 5ms. For later times the degradation in the absorption system is truly a hindrance, since for such long expansion times the absorption of the (much larger) cloud is small and the size determination is limited by the noise in the images. To overcome this noise we typically fit to a series of images with 5 different expansion times.

2.3 The Second Generation Apparatus

The second generation apparatus initially had three primary goals that constrained its design. After the masterful work of Sage et.al in the first generation, it was clear that the primary reason for a new vacuum chamber was to incorporate a CO₂ laser lattice to facilitate trapping and studying polar molecules. Once it was clear that a new vacuum chamber was necessary, a few other interesting features were added for experimental convenience. Chief among these were Quartz feedthroughs for pulsed optical trap loading using Light Induced Atomic Desorption (LIAD), as well as electrodes to facilitate distillation of pure RbCs ground state molecule samples by applying electrostatic forces. These two internal constructions, combined with CO₂ viewports that are constrained to be aligned vertically essentially dictated the orientation of the remainder of the experiment.

2.3.1 Vacuum Apparatus Construction

The centerpiece of the second generation apparatus is the vacuum chamber, which is a custom “spherical cube” from Kimball Physics. This experiment, like all of those using optical lattices, must achieve vacuum levels well into the Ultra-High or UHV regime. We were able to achieve ultimate pressures at or below 10^{-11} Torr. This is essential because we need our trapped molecule lifetimes to be limited by their own collision physics rather than by background gas collisions. If the lifetime of the trap is background gas limited then it is impossible to determine the collisional cross sections of the molecules.

The standard way to achieve these levels of vacuum is to use only low-outgassing materials while being extremely careful in handling anything that will be in the vacuum region. During vacuum handling it is vital to wear powder-free latex gloves and change them at the slightest hint of contamination. Every in-vacuum part that can survive a thorough cleaning is scrubbed with methanol using a non-abrasive cloth, then placed in an ultrasonic methanol bath for five minutes, wrapped in oil-free aluminum foil and stored in a cabinet until needed.

If there is any evidence of macroscopic dirt or machine oil it may be necessary to pre-clean the part with a sequential treatment of deionized water, acetone scrub, acetone ultrasound, methanol scrub, methanol ultrasound, and air bake at 300° C. Note that anything that has a glass-to-metal seal or is assembled commercially under vacuum, like a detector, should not be cleaned at all unless there is visible macroscopic contamination. Even if such parts need to be cleaned they should never be placed in the ultrasonic bath. Regardless of a part's fragility every single copper gasket and knife-edge in the system is thoroughly scrubbed with methanol prior to assembly.

There are a few important general design considerations in our chamber. We use new silver coated bolts each time we reassemble the apparatus after baking to avoid parts seizing. These seem to work much better than molybdenum disulfide or other lubricating powders suspended in methanol and then rolled onto the screws. These didn't seem to be much better than uncoated screws and carry the additional risk of contaminating the system with the lubricant powder.

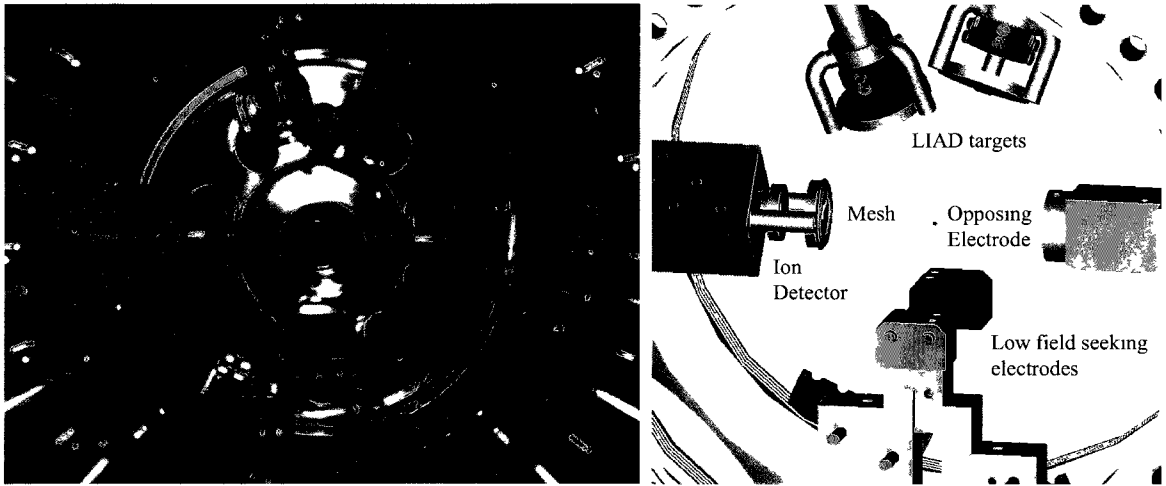


Figure 2.6: [Left:] Actual view of the chamber interior just prior to vacuum sealing. [Right:] Schematic of the chamber interior showing the major hardware that is explained throughout the text.

Because there are so many independent stainless steel parts in vacuum it is important to be vigilant about virtual leaks in custom designed parts. Ideally, one would like to use an enclosure at least one conflat size larger than any component that can reach a significant temperature (typically things with filaments like the Ti:sub pump, getters, ion gauge etc.). This is to avoid heating the chamber walls and increasing the background pressure. It is important to place all pumps behind at least one 90° elbow to minimize the effects of outgassing both during a bake and normal operation. This is especially important in the Titanium sublimation (Ti:sub) pump, because the way it operates is to actively spew high-temperature atomic titanium into the chamber.

2.3.2 Bake Protocol

In our system the background gases mainly consist of Nitrogen, Hydrogen, and water vapor that are adsorbed onto the stainless steel parts when the chamber is exposed to atmosphere. The only way to reach UHV pressures is to force these gasses to desorb at an exponentially higher rate than normal and pump them away. The way we accomplish this is to literally bake our entire vacuum chamber. We carefully wrap the entire apparatus with resistive, fiberglass-insulated heater tape, paying special attention to not concentrate the tape in sensitive areas like glass-to-metal seals and small parts with high surface area. Thermocouples are affixed to the chamber at locations around the apparatus to verify that heating proceeds evenly over the apparatus. The tape is then covered loosely, but completely in oil-free aluminum foil that serves as insulation and a way to evenly conduct the heat over the entire apparatus. The current flowing to each heater tape was individually controlled by variacs. For most UHV compatible components the suggested maximum temporal thermal gradient is on the order of 1C/min, but because the variacs are very nonlinear we generally try to change the temperature no faster than 10C/hr. whether we are heating or cooling. The ultimate temperature of 150° C is limited by the temperature rating of the ZnSe windows. Ideally, the chamber would be held at its ultimate temperature until the partial pressure of Hydrogen stopped decreasing, but in practice with such a low temperature bake this could take over a month. Instead, we wait for the H₂ pressure to stop increasing and then ramp the temperature down at roughly the same rate at which we ramped it up.

There are three stages of vacuum pumps used to maintain the pressure in our system. The basic pump is a Turbovac 50 turbo molecular pump from Leybold that

pumps at 50 liters per second. For these experiments this pump was backed by an oil-based roughing pump that provided a backing pressure of 20 millitorr. The compression ratio for this particular pump is on the order of 2×10^6 for most gasses, with the notable exception of Hydrogen. As a short practical aside, if we assume the relative atmospheric abundance of N_2 to be on the order of unity, we would expect ultimate partial pressures on the order 10^{-8} torr. So, after a bake is under way there is no need to re-leak check while heating unless it proves impossible to pump down to this partial pressure.

Background gas pressures in the chamber are measured in two ways. There is a permanently attached nude ion gauge to measure total chamber pressure, and during bake out there is a residual gas analyzer (SRS RGA-100) attached to a mobile assembly that contains the turbo and backing pump. The RGA is invaluable for monitoring both the progress of the bake and its ability to leak check by detecting Helium that is blown into the chamber. Table 2.1 summarizes typical measured pressures at various points over a typical bake.

Table 2.1: A summary of pressures over time for gas species relevant to bake out. The ion gauge measures the total background pressure in torr. The partial pressures for the listed gases are measured using the RGA. The initial pressures of the chamber are not listed due to the observed ~ 2 order of magnitude variation in pressures based on bake out and handling history.

Bake Stage	Ion Gauge	H ₂	H ₂ O	CO ₂
Day 1 (T=150 C)	1.2 (10^{-6})	2 (10^{-6})	3.5 (10^{-8})	3.5 (10^{-8})
Day 9 (T=150 C)	4.3 (10^{-7})	1.5 (10^{-6})	1.5 (10^{-8})	1.5 (10^{-8})
Final (Room Temp)	2.7 (10^{-9})	5 (10^{-9})	1.1 (10^{-9})	< 5 (10^{-10})

The combined turbopump station and RGA system is connected to the vacuum chamber by a UHV dedicated, bakeable valve so that it can be disconnected from the chamber when the bake out has finished. The high throughput of the turbo-pump is essential to remove the large volume of gas generated by the bake out procedure, but its ultimate pumping pressure is too high for our experimental needs.

The main pump which is used to maintain a reasonable base background pressure in a baked chamber is the ion pump. We use a refurbished 60 L/s V-60T triode ion pump from Duniway. Its rated operating range is from pressures of 10^{-4} to “below 10^{-8} ” torr, although the best vacuum we have achieved to date with just the ion pump is in the few 10^{-9} torr range. The triode configuration ion pump is particularly useful for our system because it excels at pumping the dominant post-bake background gas H_2 while still being able to handle acceptable gas loads of Argon and Helium, its two weakest pumping species. When acting as the primary pump the ion pump typically operates at $\sim 9(10^{-10})$ torr while drawing roughly $12 \pm 2 \mu A$ of current as read by its own controller. Because the ultimate achievable pressure of an ion pump is chamber geometry-specific, we also incorporated the Ti:sub pump into our design to ensure we reached the desired 10^{-11} torr operating region.

The Ti:sub is a set of three Titanium-molybdenum filaments mounted on a high-current electrical UHV feedthrough. The filaments are mounted on a 6” conflat elbow and cylindrical tube to maximize the surface area available for coating. Because the pump functions by one-to-one adsorption of atoms and molecules that come into contact with Titanium on the chamber surface, the pumping speed is proportional to the total surface area coated.

Normal operation of the pump consists of running 47A through one of the filaments for 3 minutes. This operation coats the walls of the chamber with direct line of sight to the filament, and will cause a spike in the chamber pressure as contaminants adsorbed onto the filament make their way into the main chamber. In a typical operation of the pump beginning with a chamber at 5×10^{-10} torr the pressure rose to 10^{-7} torr and settled in mid 10^{-8} torr range with the pump on. After 12 hours the pressure in the chamber pumped down to less than 4×10^{-11} torr, although the Ti:sub can continue to slowly pump down for months. Unfortunately we typically operate in the 2×10^{-9} torr range when loading directly from alkali dispensers and waste this pumping effect to pump away detritus from the getters. For this reason it is also necessary to use the Ti:sub once every six months to maintain adequate background pressure.

2.3.3 Degassing

During the bake out it is vital to degas all active components that do not have very good thermal contact with the chamber. These components act like cold fingers during the bake and can limit the ultimate vacuum pressure of the chamber if they are not periodically degassed during the baking process. The Ti:sub pump requires special care because it requires high currents to degas. If the pump is run above 25 A at 150 °C it is possible to thermally fracture the electrical feedthrough. The best way to degas the pump is by running each filament at 25A for 3 minutes once per day while the chamber is at temperature. This level of current is enough to heat up the filaments to drive off casually adsorbed contaminants, but is below the required threshold for desorbing Titanium. The alkali dispensers are the other important component that must be degassed. Immediately

before cooling down the dispensers are run at 5A for 30s. As the chamber is cooling down the dispensers are held at 2.5 amps until the system equilibrates at room temperature.

2.3.4 Electric and Magnetic Fields

The main coils of the MOT consist of 1/8" diameter copper refrigerator tubing wrapped with Teflon insulation and wound around a flange that extends toward the center of the vacuum chamber. Room temperature water flows continually through the tubing to provide enough cooling power to allow the coils to be run at roughly 60A. Operating at 60A and running in the anti-Helmholtz configuration, the coils produce a linear field gradient of 17G/ cm. This is where the experiment is typically run, but it is not clear if this is truly the optimal field gradient because we were limited by the ultimate power provided by the power supply.

In addition to the main MOT coils there are three sets of shim coils to further cancel the magnetic field in the center of the chamber. The coils are mounted orthogonally to each other to allow fine alignment of the MOTs and the optical lattice. The coils consist of 100 turns of Kapton coated copper magnet wire wound on circular, 4.65 cm radius plastic mounts attached to the vacuum chamber. Up to 1A can be safely run through the coils to produce a field of 500 mG at the MOT location. The coils air-cooled, so they were ordinarily run at currents no larger than 0.5A or on extremely short duty cycles (c.f. spin polarization in Chapter 4) at full current in order to avoid overheating in the air-cooled design.

The apparatus can generate in-vacuum electric fields by using two pairs of high voltage electrodes. The electrodes are designed so that they can produce a one-dimensional electrostatic force in the upward direction for both strong- and weak- field seeking states of polar molecules. The strong-field seeking trap electrode configuration consists of a large stainless steel electrode opposing a 90% clear aperture copper mesh mounted in front of our ion detector. The weak-field seeking trap is a pair of smaller stainless steel electrodes mounted toward the bottom of the chamber. The dimensions and fields are shown schematically in figure 2.7.

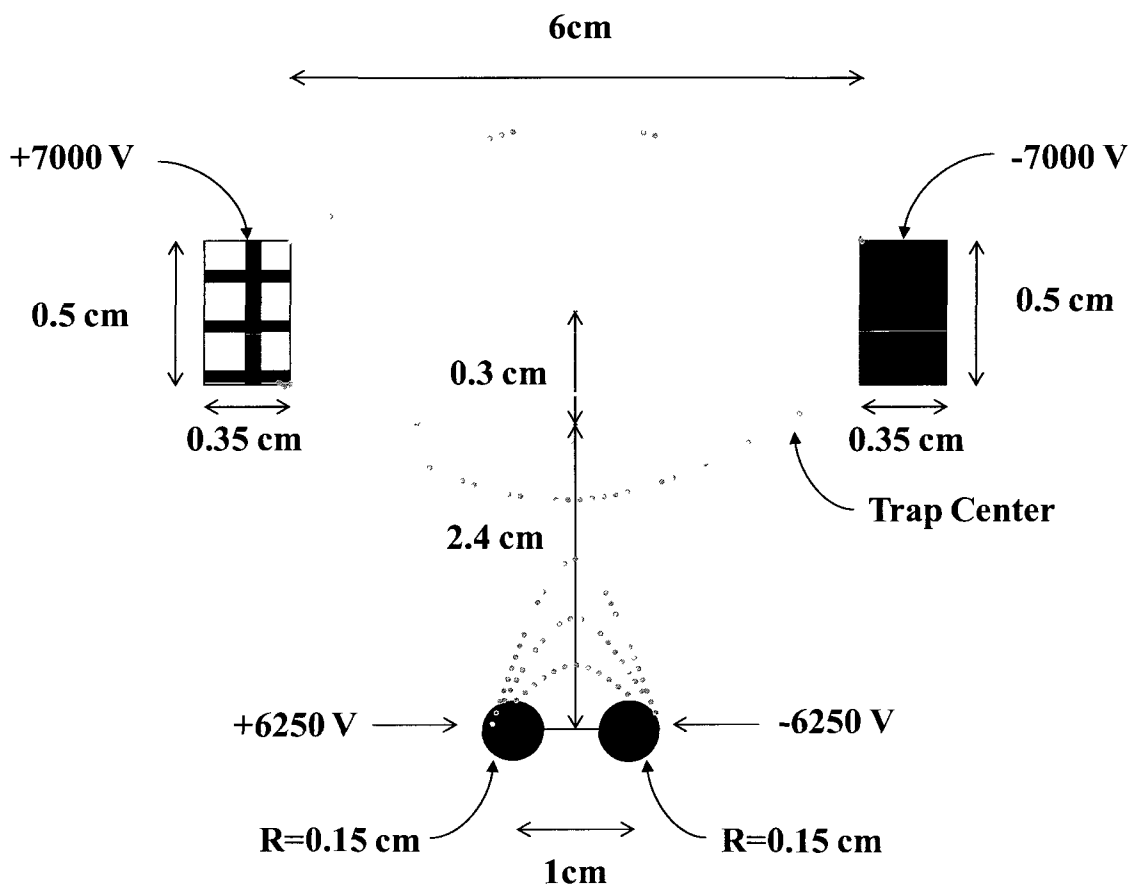


Figure 2.7: Schematic representation of the electrodes mounted in the chamber. The dotted gray lines are the qualitative field lines for the two sets of electrodes. The given voltages provide the 1-D electrostatic trap described in the text. The high-field seeking trap consists of the top two electrodes (grid on left, solid on right), while the low-field seeking electrodes are at the bottom of the page.

With the parameters described below the trap will levitate RbCs $J=0$ (strong-field seeking) or $J=1 M=0$ (weak-field seeking) molecules against gravity without forcing them out of the confinement range of the optical dipole trap. The voltages and distances described below result in a trap size of roughly 1mm for 10 μ K molecules.

Because the electrodes are isolated from the rest of the vacuum chamber they reach only a relatively low temperature during the vacuum bake. This causes them to adsorb all manner of background particles that must be removed before using them. The procedure to accomplish this is known as electrode conditioning, and consists of slowly applying even steps of voltage to both remove and ionize adsorbed contaminants and round off any microscopic sharp edges caused by surface imperfections. The procedure we followed was to apply voltage in 1kV steps up to the limit of our electrical feedthroughs at 10kV. The voltage was turned up and the current was monitored. If any current was generated the voltage was held until it dropped to zero. Otherwise, the current was held for one minute. When a current is generated by arcing in this way there is a spike in the vacuum pressure of approximately 10^{-6} torr, which quickly pumps away. We found that the electrodes require periodic reconditioning due to adsorption of remnant alkali from the dispensers' normal functioning.

2.3.5 Diode Laser Systems

There are four diode lasers used to supply all of the near-resonant light to the atoms in our apparatus. Much of the schematic idea of the setup is detailed in [Ref⁴⁴] The Rubidium trap laser is a high power laser diode from Toptica and the Cesium trap laser is a diode-tapered amplifier system from the same company. These trap lasers provide

roughly 100 mW of total power (after all AOMs) at the apparatus immediately before the beams are split into thirds to create the MOT. The trap lasers have extremely asymmetric beam profiles and require cylindrical telescopes to clean up their modes for use in AOMs and conventional telescopes before coupling into fibers. The lasers are stabilized by locking to zero crossings in the derivative signal generated by the saturated absorption spectroscopy setup shown in figure 2.8. A summary of the various AOMs and relevant beams in the experiment is listed in table 2.2.

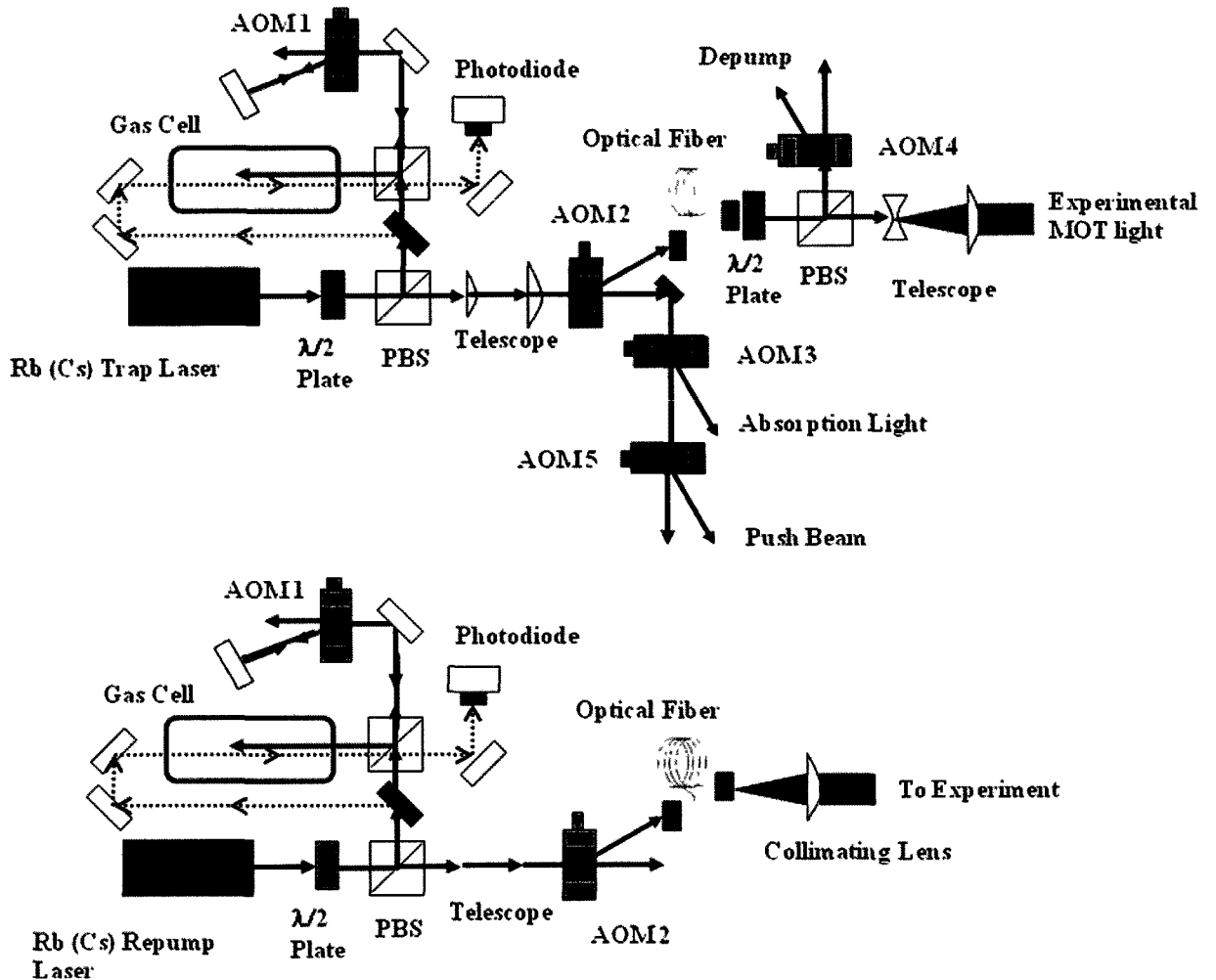


Figure 2.8: Schematic of the lasers and optics used for generating the various frequencies of light needed for the experiment. For simplicity we have only included one setup for each species. The trap beam line is shown on the top of the diagram and the repump beam line is depicted on the bottom of the figure.

Table 2.2: Summary of frequencies and AOM shifts used in the experiment

Rb Trap #1 3 → 4	Cs Trap #2 4 → 5	Rb Repump #3 2 → 3	Cs Repump #4 3 → 4
Lock to 3 → 3x4 -60.5 MHz of 3 → 4	Lock to 4 → 3x5 -226.1 MHz of 4 → 5	Lock to 2 → 1x3 -46.4 MHz of 2 → 3	Lock to 3 → 2x4 -176 MHz of 4 → 5
AOM 1 1 – Sat Abs DP – 121.5 MHz Order -1 $\Delta = +120.2$ MHz	AOM 2 1 – Sat Abs DP – 102.5 MHz Order -1 $\Delta = +100.7$ MHz	AOM 3 1 – Sat Abs DP – 80.5 MHz Order +1 $\Delta = -80.5$ MHz	AOM 4 1 – Sat Abs DP - 110 MHz Order -1 $\Delta = +98.9$ MHz
AOM 1 2 – Switching SP – 73.5 MHz (fixed) Order -1 $\Delta = -73.5$ MHz	AOM 2 2 – Switching SP – 111.6 MHz (fixed) Order +1 $\Delta = +111.6$ MHz	AOM 3 2 – Switching SP – 126.9 MHz (fixed) Order +1 $\Delta = +126.9$ MHz	AOM 4 2 – Switching SP – 77.1 MHz (fixed) Order +1 $\Delta = +77.1$ MHz
$\Delta_{\text{Total}} = -13.8$ MHz	$\Delta_{\text{Total}} = -13.8$ MHz	$\Delta_{\text{Total}} = 0$	$\Delta_{\text{Total}} = 0$
Rb Abs 3 → 4	Cs Abs 4 → 5	Rb Fill-in 2 → 3	Cs Fill-in 3 → 4
0 th order of AOM 1 2 - 59.7 MHz of 3 → 4	0 th order of AOM 2 2 -125.4 MHz of 4 → 5	0 th order of AOM 3 2 -126.9 MHz of 2 → 3	0 th order of AOM 4 2 - 77.1 MHz of 3 → 4
AOM 1 3 – Switching SP – 61 MHz Order -1 $\Delta = -61$ MHz	AOM 2 3 – Switching SP - 121 MHz (fixed) Order +1 $\Delta = +121$ MHz	AOM 3 3 – Switching SP – 126.9 MHz (fixed) Order +1 $\Delta = +126.9$ MHz	AOM 4 3 – Switching SP – 77.1 MHz Order +1 $\Delta = +77.1$ MHz
$\Delta_{\text{Total}} = -1.3$ MHz	$\Delta_{\text{Total}} = -4.4$ MHz	$\Delta_{\text{Total}} = 0$ MHz	$\Delta_{\text{Total}} = 0$ MHz
Rb Depump 3 → 3	Cs Depump 4 → 4	Rb Push 3 → 3	Cs Push 4 → 4
Take from trap post FC +108.5 MHz of 3 → 3	Take from trap post FC +238.5 MHz of 4 → 4	Take from trap post FC +108.5 MHz of 3 → 3	Take from trap post FC +238.5 MHz of 4 → 4
AOM 1 4 – Switching SP – 111.6 MHz (fixed) Order -1 $\Delta = +111.6$ MHz	AOM 2 4 – Switching DP – 121 MHz (fixed) Order -1 $\Delta = -242$ MHz	AOM 1 4 – Switching SP – 111.6 MHz (fixed) Order -1 $\Delta = +111.6$ MHz	AOM 2 4 – Switching DP – 121 MHz (fixed) Order -1 $\Delta = -242$ MHz
$\Delta_{\text{Total}} = -3.1$ MHz	$\Delta_{\text{Total}} = -3.5$ MHz	$\Delta_{\text{Total}} = -3.1$ MHz	$\Delta_{\text{Total}} = -3.5$ MHz

3. The Optical Lattice

3.1 Background

In order to perform experiments with both cold molecules and atoms, we need a way to simultaneously confine rubidium, cesium, Rb_2 , Cs_2 , and RbCs . In addition, we would also like to confine the particles of interest for times on the order of a second. For atoms at our temperatures a good solution is to employ an optical lattice trap.

Unlike atoms, molecules in general do not have closed transitions. As a result, the methods used to magneto-optically trap atoms cannot, except perhaps in a few special cases⁴⁵, be applied. Although molecules do not have closed transitions, they do have a large number of transitions due to the two additional degrees of freedom in a diatomic molecule relative to an atom. Because there are so many available transitions, and particularly because many of the transitions are expected to be around the $\sim 1 \mu\text{m}$ region, we have chosen to employ a dipole force trap so far detuned from any relevant transitions in the system it acts as a quasi-electrostatic trap or “QUEST^{46,47}.” In our case the trap is created by a focused standing wave of a $10.6 \mu\text{m}$ CO_2 laser. We will approach our brief, and simple, theoretical background for the QUEST in three main parts: first we will discuss and derive the optical dipole force, then we will examine the case of a far off resonant trap, and finally we will work out the entirety of the QUEST lattice.

3.1.1 The Dipole Force

We derived an expression for the dipole force on an atom in the previous chapter based on the rotating wave approximation (RWA). Although as we discuss later this

approximation breaks down under our experimental conditions, here for simplicity we discuss the dipole force under the RWA. If we define the Rabi frequency to be

$$\Omega = -\mathbf{d}_{ab} e E_0 / \hbar \quad (3.1)$$

we can write the previous definition of the dipole force (2.16) as

$$F_{dip} = -\hbar \Omega u_{st} \left(\frac{\nabla \Omega}{\Omega} \right) \quad (3.2)$$

then we can substitute (2.11) for u_{st} and find

$$F_{dip} = \frac{-\hbar \delta_L}{4} \frac{\nabla(\Omega^2)}{\delta_L^2 + \frac{\Gamma^2}{4} + \frac{\Omega^2}{2}} \quad (3.3)$$

This force is only non-zero when a field with a gradient drives it so unlike F_{dissip} it is necessarily zero in a generic running wave. We can express F_{dip} as the gradient of an optical potential $F_{dip} = -\nabla U_{opt}(R) \propto \nabla I(R)$ we can see that the force is conservative as well as being proportional to the driving field's intensity. Note that the dipole force, as opposed to the Doppler force, will not saturate with intensity. The dipole force is also proportional to the detuning and for red $\delta_L < 0$ detuning it will drive atoms toward potential minima in the optical potential, which are maxima in the field's intensity.

It is instructive to view the total force in terms of the saturation parameter

$$s \equiv \frac{\Omega^2/2}{\delta_L^2 + \Gamma^2/4} = \frac{s_0}{1 + 4\delta_L^2/\Gamma^2} \quad (3.4)$$

Where we define

$$s_0 \equiv \frac{I}{I_{sat}} = \frac{2\Omega^2}{\Gamma^2} \quad (3.5)$$

and $I_{sat} \equiv \pi \hbar c \Gamma / 3 \lambda^3$ which allows us to rewrite as

$$F_{dip} = \frac{\hbar\Gamma^2}{8I_{sat}} \left[-\frac{\nabla I(\mathbf{r})}{\delta_L} \right]. \quad (3.6)$$

For an optical trap, what we are truly interested in are the scaling of the optical potential depth and the trap photon scattering rate, which in this case will determine the heating caused by the trap itself and limit the trap lifetimes. Although the above expressions are informative, we must account for the breakdown in the RWA to gain additional insight.

3.1.3 Quasi Electrostatic Traps and Lattices

In our case we must consider extremely large laser detunings, δ_L , such that $\delta_L \ll \Delta_{HFS}$ and $\omega_L \ll \omega_0$ where Δ_{HFS} is the hyperfine splitting and ω_0 and ω_L are the transition and laser frequencies respectively. In this case the rotating wave approximation invoked in chapter 2 no longer applies and the optical trap acts like a quasi-electrostatic trap (QUEST). For laser wavelengths of 10.6 μm the saturation parameter (3.4) is always quite small for our laser powers. This allows us to write the general form of the Stark shift to leading order in perturbation theory as

$$\Delta E_g = -\frac{1}{4\hbar} \sum_e |\mathbf{d}_{eg} \cdot \mathbf{E}|^2 \left[\frac{1}{\omega_{eg} - \omega_L} + \frac{1}{\omega_{eg} + \omega_L} \right], \quad (3.7)$$

with $\omega_{eg} = (E_e - E_g)/\hbar$ and the subscripts e and g refer to excited and ground states.

Because we are so far-detuned there is negligible population in the excited states due to trap light and we can use the ground state static polarizability, α_s , to write the optical potential as

$$U_{opt} = -\frac{1}{2} \frac{\alpha_{st}}{[1 - (\omega / \omega_L)^2]} I(r), \quad (3.8)$$

where α_{st} is the static polarizability, which is simply the polarizability at zero frequency.

At our wavelengths the optical potential (3.8) is well-approximated by a spatially

dependent DC Stark shift $-\alpha_{st} \frac{I(r)}{2\epsilon_0 c}$. As a result, the trap potential no longer depends on

the detuning or reference to any specific transition in the atom. This makes it possible to trap multiple types of atoms and molecules in the same optical potential.

The final aspect we have yet to discuss is the use of a standing wave to form an optical lattice. Two counter propagating, linearly polarized beams have an electric field

$$\mathbf{E} = E_0 \cos(\omega t - kz) + \cos(\omega t + kz) \hat{\mathbf{e}}_x = 2E_0 \cos(kz) \cos(\omega t) \hat{\mathbf{e}}_x \quad (3.9)$$

This field results in a dipole potential

$$U_{lattice} = U_0 \cos^2(kz) \quad (3.10)$$

where U_0 is the maximum light shift (at the antinodes) which has an intensity and corresponding potential depth four times greater than that of a single beam trap. The standing wave trap has the same radial confinement as the single beam trap, but has a much stronger dipole force along the axis of the beam. The standing wave forms an array of $\lambda/2$ sized pancake traps stacked up in the z direction that can easily levitate a sample of atoms against gravity.

One final note is that the general form of the scattering rate for a dipole trap is

$$R_{scat} = \frac{\Gamma^3}{8I_{sat}} \left[\frac{I(\mathbf{r})}{\delta_L^2} \right] \propto \frac{I(\mathbf{r})}{\delta_L^2}. \quad (3.11)$$

While this does not strictly apply for our case, it informs the choice of the QUEST as a tool for trapping atoms and molecules. The scattering rate and trap depth are both linear in the intensity but the scattering rate scales as the square of the laser detuning. For atom trapping applications one usually wants a trap deep enough to contain an atomic or molecular sample of a given temperature while minimizing heating due to scattering from the trap beam. For a given beam focusing a high intensity beam using a long wavelength will fulfill both criteria. Further discussion of the trap requires specific knowledge of the parameters involved.

3.1.2 Gaussian Beam Traps

The dynamics of trapping atoms require specific knowledge about the spatial dependence of the driving field $I(r)$. We consider a focused beam with a Gaussian radial intensity profile that propagates in the z direction with a $1/e^2$ radius of w_0 . If the beam has a power P the laser's intensity profile is⁴⁸

$$I(r, z) = \frac{2P}{\pi w^2(z)} \exp\left(-\frac{2r^2}{w^2(z)}\right) \quad (3.12)$$

Here the variation of the beam waist with z is described by⁴⁹

$$w(z) = w_0 \sqrt{1 + \left(\frac{z}{z_R}\right)^2} \quad (3.13)$$

where z_R is the Rayleigh range defined as

$$z_R = \pi w_0^2 / \lambda \quad (3.14)$$

The various beam parameters are summarized in figure 3.1. Because $z_R/\omega_0 = \pi\omega_0/\lambda$ the dipole trap configuration will confine a cold atomic sample very tightly in the transverse region, but not very well along the axis of the focusing lens due to the relatively gentle gradient in the field in the z direction. The trapping potential must overcome gravity and as a result, traps of this type are usually implemented horizontally because of the relatively small confinement force they generate in the z direction.

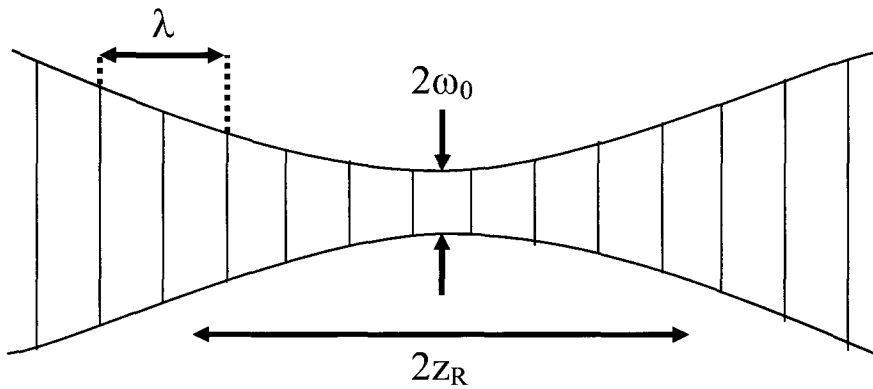


Figure 3.1: A schematic showing a horizontal optical lattice. The relevant Gaussian beam parameters are labeled, as well as the lattice spacing for the case of a retroreflected optical lattice. Note that in reality for our system the Rayleigh range ZR is 1 mm vs. a beam waist of 100 μm .

In our case we have intentionally aligned our trap beam vertically to preserve the option of filtering our sample by letting atoms and molecules leak out of the trapping region due to gravity. An additional beam can be added to the dipole trap configuration to create a standing wave that provides a strong force against gravity, but before we discuss this configuration we must address the fact that we operate our trap in a very far red-detuned mode.

3.1.4 Trapping Actual Atoms and Molecules

Up to this point we have only considered model two-level atoms with detunings large compared to the Rabi frequency. Since we plan to operate in the electrostatic regime, there is very little difference between the model system and actual atoms. The detuning is very large compared to the fine structure and any smaller splittings, so we are free to apply the framework we have developed in this section to actual atoms.

3.2 Experimental Implementation of the Lattice

In the previous section we investigated some of the scaling characteristics of the dipole force. Because the optical potential is roughly proportional to I/δ_L while the principal heating mechanism, the scattering force, is proportional to I/δ_L^2 , it is clear that the ideal dipole trap will maximize both the intensity and detuning. The principle downsides to maximizing these quantities are the technical hurdles of dealing with high-power and the increase in lattice spacing as one red detunes the laser. Because 5- μm

lattice spacing is acceptable for our experiments, we have implemented an optical lattice trap using a 100W CO₂ laser operating at a 10.6 μm wavelength. This technology satisfies our requirements of maximizing the intensity and detuning of the trapping beam and is far enough detuned that it places the system deep in the quasi-electrostatic regime.

An acousto-optic modulator (AOM) is placed in the CO₂ beam to allow modulation of the trap depth. After the AOM the beam profile must be shaped to allow for maximum focusing of the laser to create a deep optical trap. This section outlines the development of the beam line and the relevant details of the important equipment involved in control of the CO₂ laser.

3.2.1 The CO₂ Laser

The lattice is produced by a Coherent-DEOS GEM Select 100 CO₂ laser. This laser operates on a single, fixed CO₂ vibrational line near 10.6 μm and emits 100 W of laser power as measured immediately after the output coupler. The actual laser has some non-ideal features that must be considered when setting up the beam line. The first consideration is that it takes 2200 W of RF power to pump the laser, which must be actively fluid-cooled (we use a Merlin M-75 chiller filled with a 2:1 volume mix of distilled water and inhibited propylene glycol). As a result there are initially serious transient thermal effects on both the laser power and beam profile when the laser is turned on. It takes between 30 minutes and an hour for the laser to reach a steady state while operating at full power. Once it has arrived at this steady state we observe a consistent beam profile with long-term power fluctuations to be below the 200 mW resolution of our thermal power meter.

The beam profile is slightly elliptical with a larger horizontal dimension. The horizontal (H) and vertical (V) divergences of the two axes of the beam as measured 1m from the output coupler were $\theta_H = 4.5$ mrad and $\theta_V = 4.2$ mrad with a horizontal beam waist $W_H = 2.6$ mm and a vertical beam waist $W_V = 2.45$ mm measured at the same location. The only practical result of this deviation from the ideal case was to dictate where we place the switching AOM in the beam path. Because the AOM substantially alters the beam profile of the laser, we found that it was most effective to let the beam diverge naturally and place the AOM where its output mode was cleanest, which was in the vicinity of 1m from the output coupler of the CO₂ laser.

3.2.2 The CO₂ AOM

The key piece of hardware around which we designed the CO₂ beam line, was the high power, water cooled AGM-406BIM Acousto-Optic Modulator from Interaction Corporation. The AOM consists of a germanium crystal driven by a GE-4030-6 driver that provides 30 W of stable RF power at 40 MHz. It is mounted on a very sturdy New Focus 9801 kinematic stage. Under normal operating conditions the CO₂ hits the crystal with 98 ± 1 W of power and we get 75 W of power in the -1 diffracted order for a diffraction efficiency of 85% (taking into account the crystal's 10% insertion loss). The undiffracted order is directed into a beam dump.

The total heat load of 40W dissipated by the AOM pales in comparison to the thermal load on the laser, but is in practice much more important to monitor. Thermal fluctuations in the AOM cause fluctuations in beam pointing, which is especially critical for our optical lattice implementation. In contrast, small long-term fluctuations in the

total laser power usually result in a small change in power at the vacuum chamber caused by a change in higher order modes that are spatially filtered by the long beam line. Or rarely, a correctable constant pointing offset. We have observed massive variations in both the output beam mode and pointing due to temperature fluctuations in the AOM. If the temperature of the AOM case rises more than 1°C the diffraction efficiency of the AOM will be reduced, and will cause the beam pointing to shift by millimeters over the length of the entire beam line. If the temperature rises more than 3°C the beam mode changes from a rough Gaussian profile to an actual donut mode, with no power in the center of the beam.

The AOM temperature is crudely monitored by a thermocouple screwed on to the exterior case. This gives a baseline measure of between 22.5°C - 24°C which is a function of the thermal conditions in the rest of the lab. We typically had our best results with a temperature level around 23.1°C . In order to stabilize the temperature in the AOM it was decoupled from the CO_2 laser cooling circuit and switched to a separate chilling line with more cooling capacity. An important result of the thermal loading characteristics of the AOM is that we were unable to use it to switch the trap on during an atomic loading cycle, since it takes a full second to stabilize. This means that all experiments involving the CO_2 beam must begin in the presence of the beam. The QUEST can, however be switched off in approximately $1\ \mu\text{s}$. This feature is used to release atoms and molecules from the trap, in order to determine their temperature.

3.2.3 Development of the Beam Line

In addition to the AOM placement, the other main constraint on the beam layout was the tension between focusing the beam as tightly as possible to maximize trap depth while damaging neither the ZnSe entrance window to the vacuum chamber nor the low field seeking electrodes inside the chamber. As a safety measure to avoid thermal damage to the ZnSe-to-metal seals, we attempted to generate a beam diameter at the ZnSe window that was 80% of the window's diameter. This corresponds to horizontal and vertical beam waists of 8 mm and 9 mm respectively at the location of the lens placed roughly 1" below the ZnSe window. These beam parameters are used to estimate the beam waist at the focus of the beam, w_0 , which is determined by the expression

$$2w_0 = \frac{M^2 \lambda f}{\pi(2w_{lens})^2} + \frac{K(2w_{lens})^3}{f^2}. \quad (3.15)$$

Here f is the 6" focal length of the lattice lens with an incident beam waist w_{lens} described above. The laser wavelength is λ , M^2 is the empirically measured beam parameter product of 1.2, and K is the spherical aberration coefficient with a value of 0.0187 for our meniscus lens. The resultant beam waists at the lens foci are $w_{0,h} = 95 \mu\text{m}$ and $w_{0,v} = 85 \mu\text{m}$ respectively. With a laser power P of 60 W actually reaching the first lattice lens we calculate a trap depth of ϵ^{50}

$$U_0 = 4 \times \frac{2\alpha_{stat}P}{\pi\epsilon_0 c(w_{0,v}w_{0,h})}, \quad (3.16)$$

where the static polarizability α_{stat} is $2 \times 10^{-5} \text{ MHz}/(\text{W}/\text{cm}^2)^{51}$ for RbCs molecules. In this case ϵ_0 is the permittivity of free space and c is the speed of light. The factor of two in the numerator of (3.16) converts averaged measured power to peak power for a Gaussian

beam. The further factor of 4 accounts for the doubling of the electric field due to the retroreflected beam in the lattice configuration. Given the static polarizabilities of $^{85}\text{Rb}^{52,53}$ and $^{133}\text{Cs}^{54,55}$ atoms we find trap depths of 6 mK, 4 mK, and 2.5 mK for RbCs, Cs, and Rb respectively. The above calculation assumes perfect overlap of the lattice beam foci. With this beam geometry we also have calculated that we heat the low-field seeking electrodes with an acceptable power of 230 μW due to beam overlap.

Because 10.6 μm is such a long wavelength and the beam must be aligned at full power, imaging the beam is a non-trivial exercise. The $1/e^2$ beam diameter is only 4.3 mm at a distance of 2m from the output coupler, so the only practical way to quickly interrogate the beam is to burn either pieces of cardboard or firebrick. Fortunately this crude method of alignment is sufficient to allow overlap of 780 nm absorption light with the beam by using a series of flip-mounted mirrors.

The beam parameters were measured by performing repeated measurements of the beam waist using a slit constructed from a pair of razorblades mounted on a two-axis translation stage. The razors were protected by a covering of anodized aluminum to prevent thermal drilling of their edges. Even with this protection it was inadvisable to profile the most intense center region of the beam, because this resulted in damage to both the razorblades and the power meter head.

Once the beam had been expanded to a larger size, we used a series of thermal imaging plates with a UV light to image a shadow of the beam. This equipment comes as a convenient set from Macken Instruments, but the images it produces can be slightly misleading.

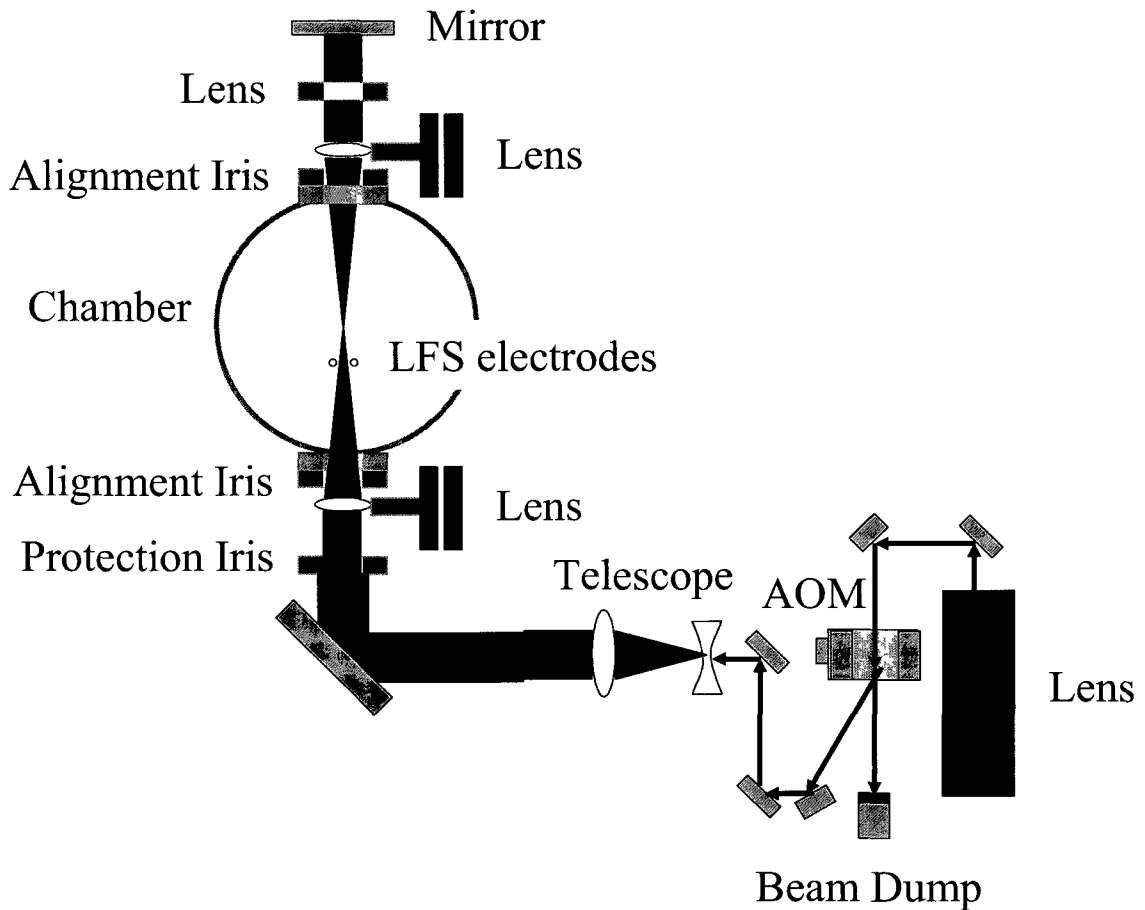


Figure 3.2: Schematic representation of the CO₂ beam line with emphasis on the hardware that enables the lattice. None of the distances are even close to scale, and the final mirror before the vacuum chamber actually directs the beam vertically.

The active material of these plates tends to saturate easily, so it is possible to be disturbed by extraneous mode structures that are very visible on the plates, but do not contain significant power. A good way to convince oneself that the beam mode is decent is to measure the total power of an area that does not contain the feature in question. As an historical note we have tried multiple optical methods of reducing the power in the beam line. These consisted of ZnSe wedges placed back-to-back in order to reduce the power in the transmitted beam without significant walk off. This concept was unsuccessful due to far too much residual beam displacement. Another optical power tuning method was an optical isolator using a water-cooled polarizer consisting of multiple Brewster plates in

series combined with a $\lambda/4$ plate. Unfortunately the wave plate was made out of CdS, which has a small band gap that allows room lights to excite electrons into the conduction band, which allows the wave plate to absorb 10.6 μm light. The thermal damage to the optic can (and, alas, did) cause it to act like a mirror that can retroreflect the beam and cause significant damage to the laser.

There is a telescope after the AOM in order to control the beam mode at the last lens before the vacuum chamber. This telescope has undergone two major iterations. The first version was a commercial (Wavelength Technologies) tunable 2x-8x beam expander. This part was functional, but replaced by a much more effective cylindrical Galilean telescope located with its input diverging lens 39" after the AOM. The telescope consisted of an $f = -3$ " lens and an $f = +7.5$ " lens aligned to expand the beam in the horizontal dimension, because by chance the natural vertical divergence of the beam coming out of the AOM yields the ideal vertical beam waist at the first lattice lens.

The beam is steered to the chamber using 2" protected silicon mirrors mounted on heavy posts to minimize vibration. The beam is steered vertically toward the chamber where it passes through a 1" stainless steel iris closed down to the final desired diameter of the beam. This iris serves to protect the last lens before the vacuum chamber as well as the ZnSe -to-metal seal of the viewports from thermal damage. During the course of normal operation, clipping of the high-powered beam by the protection iris causes this iris to heat up to a steady-state temperature of 68° C. The protection iris is placed a full 12" below the viewport so that it can convectively cool without affecting other optical components. As it continues the beam is focused by the last lens before the vacuum chamber as shown in figure 3.2. This is a 6" plano-convex ZnSe lens mounted on a 1/2"

post that is attached to a 1" total throw translation stage. The beam is gently focused as it passes through an alignment iris epoxied directly on the surface of the bottom viewport. The beam passes through the bottom viewport, into the chamber, reaches a focus at the center of the chamber, and then is diverging as it passes through the viewport and alignment iris on the opposite side of the vacuum chamber. Finally, the beam is collimated by a lens on the top side of the chamber, passes through another protection iris and is retroreflected off of a 2" mirror back into the chamber.

Initially we intended to slightly misalign the retroreflected beam such that it still overlapped in the trapping region, but was well-differentiated from the main beam once it traveled back to the AOM. We estimate that a beam separation of $\sim 3\text{mm}$ at the AOM is necessary to be able to deflect the retroreflected beam. Unfortunately, for a total beam path on the order of 3m the divergence between the two lattice beams must be much less than 1 mrad in order to preserve the lattice. This geometry did not allow us to deflect the return beam of the lattice, which led to an increase in heat load on the AOM when the lattice was implemented. This increased heat load in turn misaligned the trap beam and made a re-optimization of the lattice trap necessary every time it was turned on.

3.3 Lattice Diagnostics

The diagnostic tools we used for aligning the lattice all used loaded atoms as a basis for fine-tuning various beam alignments as well as perfecting loading techniques. Because the lattice must be run at full power and is spatially constrained by the low-field seeking electrodes, it serves as the static reference point for all other beams in the

experiment. In this section we describe how the lattice was loaded as well as the various diagnostics that were used to optimize the loading procedure.

3.3.1 Absorption Measurements in the Lattice

We use the same optics to image the shadow of the atoms in the lattice as we do in the MOT, but we have to be more precise about how we interpret the specifics of the measurement in the lattice. The intensity of an absorption beam propagating in a direction x is proportional to

$$\frac{dI}{dx} = -n(x, y=0, z=0)\sigma(\delta_L)I, \quad (3.17)$$

where $n(x, y, z)$ is the density profile of the atom cloud and $\sigma(\delta_L)$ is the absorption cross-section as a function of laser detuning. We choose to fit the density distribution to a Gaussian of the form

$$n(x, y=0, z=0) = \frac{A}{w\sqrt{\pi/2}} e^{-2\left(\frac{x}{w}\right)^2}, \quad (3.18)$$

with the cloud waist w and the peak density defined as $n_p = n(x=0, y=0, z=0)$. Now we integrate (3.17) to find an expression for n_p and we find

$$n_p = \frac{\ln \frac{I}{I_0} + 4 \frac{\delta_L}{\Gamma^2}}{w\sqrt{\pi/2}\sigma(\delta_L=0)}, \quad (3.19)$$

where all quantities have their usual meanings. Note the absorption cross section in the denominator is the resonant absorption cross section given in chapter two. Now if we model our atomic cloud as an oblate spheroid with a long axis L defined by the Gaussian

waist measured for the cloud in the direction perpendicular to the beam waist, we can compute the total number of atoms

$$N_{atoms} = n_p \int e^{-2\left(\frac{x}{w}\right)^2} e^{-2\left(\frac{y}{w}\right)^2} e^{-2\left(\frac{z}{L}\right)^2} dx = \left(\frac{\pi}{2}\right)^{\frac{3}{2}} n_p w^2 L \quad (3.20)$$

The average density follows as

$$n_{avg} = \frac{N_{atoms}}{\frac{4}{3}\pi w^2 L} = \frac{3}{8} n_p \sqrt{\frac{\pi}{2}} \quad (3.21)$$

The procedure for extracting an average density from the absorption images is to fit the absorption profile at a known detuning to a Gaussian curve with the waist and absorption depth as free parameters. These two quantities are then inserted into (3.19) to find the peak density, which is converted into the average density by insertion into (3.21). A typical absorption image and its accompanying fits are shown in figure 3.3.

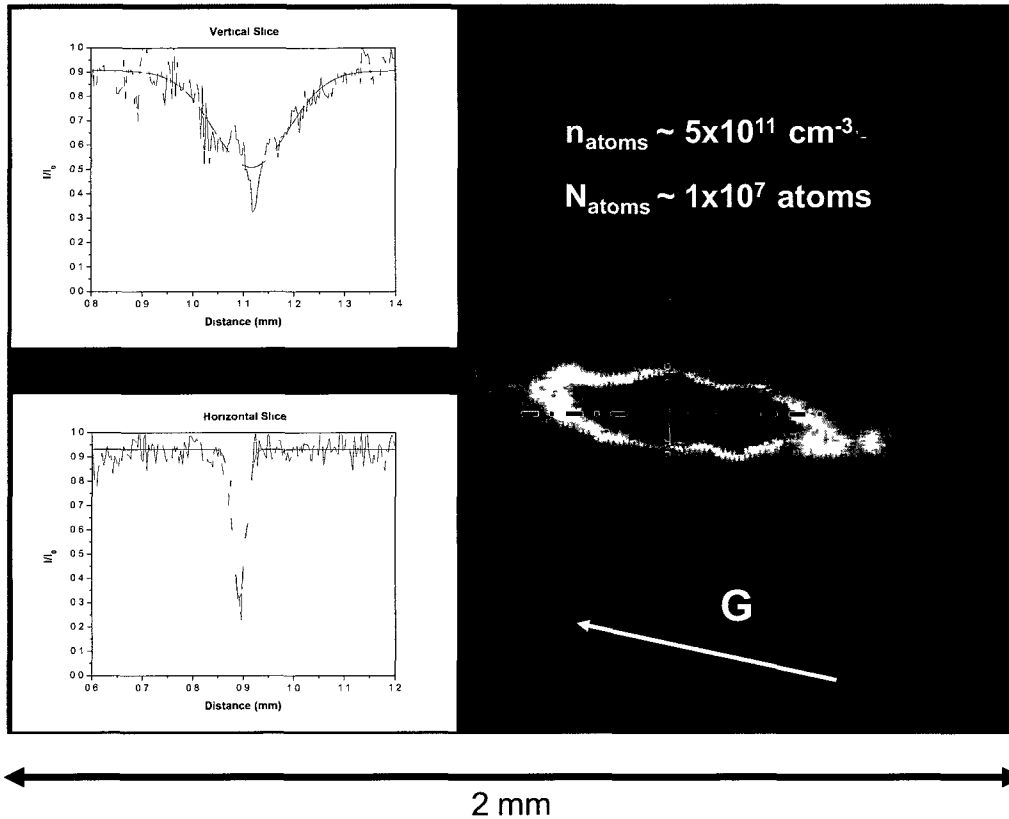


Figure 3.3: A typical absorption measurement loading Rb atoms from a dark spot MOT into the lattice. Absorption measurements are taken at a detuning of 10 MHz from the atomic resonance along orthogonal axes shown by the dashed black lines. The absorption profile graphs are labeled vertical and horizontal in reference to the lab frame, so the horizontal line in the graph corresponds to the extent of the “vertical” profile fit. The lengths of the dashed lines correspond to the extent of the data shown in the fits. The Gaussian fits obtained from the graphs are then converted into a density using the formula in the text. The results are shown.

3.3.2 Loading Protocols

The quasi-electrostatic optical lattice will induce a spatially dependent Stark shift on the energy levels of any atom or molecule proportional to the scalar polarizability of the level in question. Each level also has a tensor component to its polarizability (although this is negligibly small for the ground s states of alkali atoms) and a corresponding Stark shift quadratic in the induced electric field. The difference between

the scalar polarizability of the s and p states in addition to a small contribution from the tensor polarizability of the p state causes a differential Stark shift. This effect will shift the excited state to a lower energy relative to the ground state, causing the MOT trap light to be effectively blue-detuned from the cycling transition when the atom is in the lattice. The MOT trap light makes the lattice into an anti-lattice, which makes it extremely difficult to load any atoms into the lattice by simply overlapping the MOT and QUEST. The way to overcome this is to implement an optical molasses phase in our loading sequence.

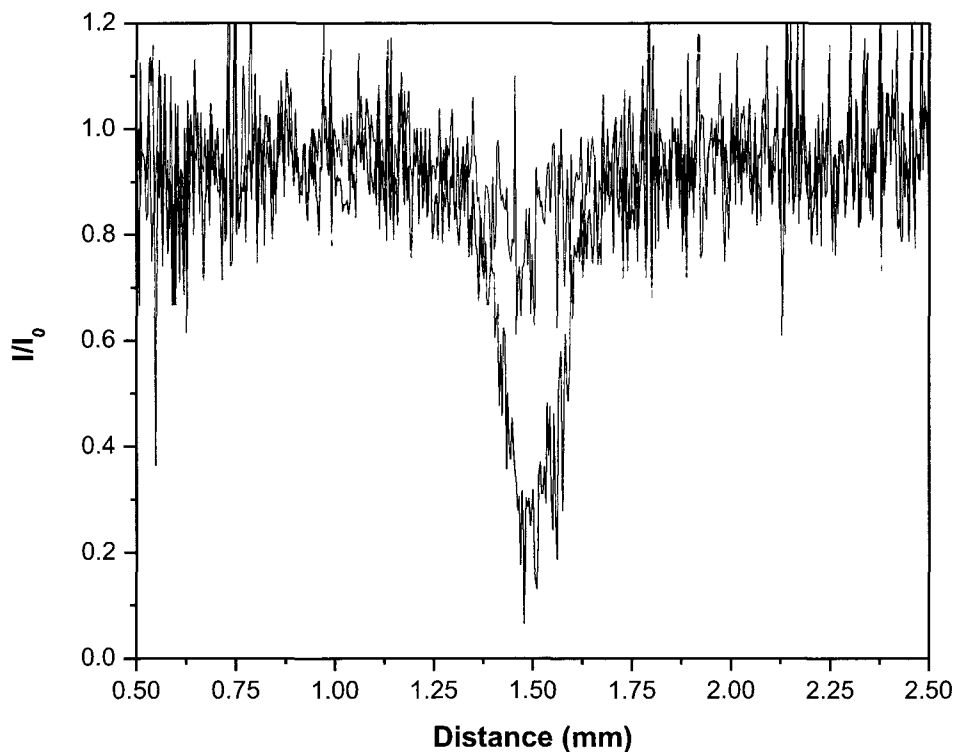


Figure 3.4: Absorption measurement of Cs atoms in the optical lattice. The figure shows the absorption profile with (red) and without (black) a 20 ms optical molasses phase during trap loading. The image is for an optical molasses detuning of 200 MHz from the Cs trap transition.

The procedure for loading atoms into the lattice is to load the MOT, then hold the trap laser frequency constant for 100 μs . After this time, the trap laser lock is turned off and a constant frequency shift is applied to the laser relative to its locked value. This condition is held for 9.9 ms, then the repump light is turned off. At the same time the frequency shift is released. One hundred microseconds later, the trap light is extinguished (but restored to prepare for the next loading/molasses cycle). This procedure detunes the trap lasers by a constant amount proportional to the applied holding voltage for 10 ms. This is not a true molasses protocol, since we do not ramp the repump intensity or usually turn off the magnetic field for the MOT. We speculate that the only reason this procedure works is due to our use of what is effectively equivalent to a spatial dark spot⁵⁶, which has a spatial depump gradient (here due to the lattice light-imposed Stark shifts of the depump transition) that allows the lattice to load. This procedure seems to compensate for the differential light shifts⁵⁷ on the MOT cycling transitions and allow a factor of four more atoms to be loaded into the lattice.

3.3.3 Temperature Measurements

We measure the temperature of atoms in the optical lattice with ballistic expansion. This method proceeds in an exact analogy to the measurement in the MOT. We turn off the lattice for a fixed time delay and then measure the expansion of the cloud's waist versus time. The functional dependence of the cloud waist versus time can then be related to the temperature of the atoms in the cloud exactly as in Chapter 2.

A typical expansion study is shown below for Rb atoms at various trapping times.

A typical temperature of atoms in the lattice was between 60-150 μK when trapping on the order of 10^9 atoms.

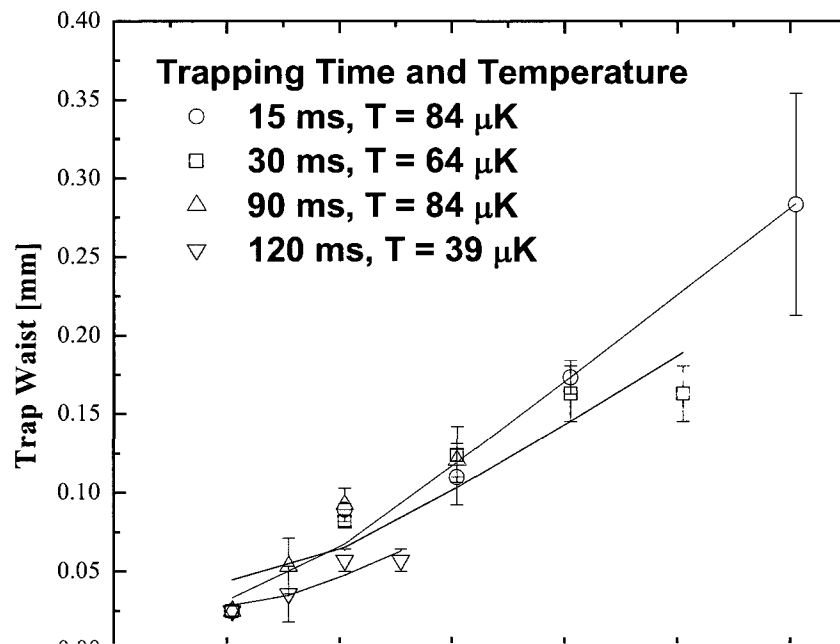


Figure 3.5: Ballistic expansion measurement of Rb in a lattice for varying expansion times. The signals were fit to a waist expansion formula as discussed in Chapter 2. Error bars were generated by the span of three measurements at each expansion time. The experiment was performed at a trap depth of 300 μK .

The atoms in Figure 3.5 may be evaporating; that is, the sample might be getting colder overall because the hottest atoms are leaving the trap. This could happen for this experiment because it was performed with a trap depth of only 300 μK . It has been shown⁵⁸ that atomic samples in dipole traps tend to have an evaporative decay in the first 100 ms of trapping time where the atoms equilibrate to a temperature of $U_0/10$. That is clearly not the case for this set of measurements, but it can qualitatively explain the

cooling for longer lifetimes. In any case, the atom temperature is consistent with the MOT temperatures, although with additional optimization of the “molasses” phase we were able to achieve atomic temperatures of 20 μK in the lattice.

3.4 Ion Detection

A critical diagnostic for both lattice overlap and background pressure was the trap lifetime of atoms confined to the lattice. Because absorption imaging does not work on molecules and we wanted to state-selectively detect RbCs molecules, we built the capability to do ion detection into our apparatus. We will deal with the specifics of the molecular ionization process in the next chapter and describe the calibration of the ion detection using rubidium atoms in this section.

3.4.1 Resonance Enhanced Multi-Photon Ionization

We used resonance-enhanced multiphoton ionization (REMPI)⁵⁹ to photoionize both atoms and molecules in our apparatus. Ion detection of atoms in the lattice consists of firing a resonant pulse that drives the two-photon 5S-7S transition in Rubidium and then ionizing the transferred atoms with a second pulse that arrives after a typical delay of 10 ns (2+1 REMPI). A negatively biased ion detector attracts the positive ion created by the second pulse. The process is shown schematically in figure 3.6. The time it takes the ions to reach the detector is proportional to the square root of the mass of the ion. This enables us to differentiate between Rb, Cs, and RbCs ions on the basis of arrival time alone.

We chose to use a pair of pulsed lasers to perform each step of the REMPI process. This allowed us to independently tune the resonant step to various intermediate states while still maintaining a fully saturated ionization pulse. Most importantly, because we had two independent lasers we were able to switch between atomic and molecular transitions for diagnostic purposes. The two lasers used will be described in detail in the next chapter, along with how the ion detector functions.

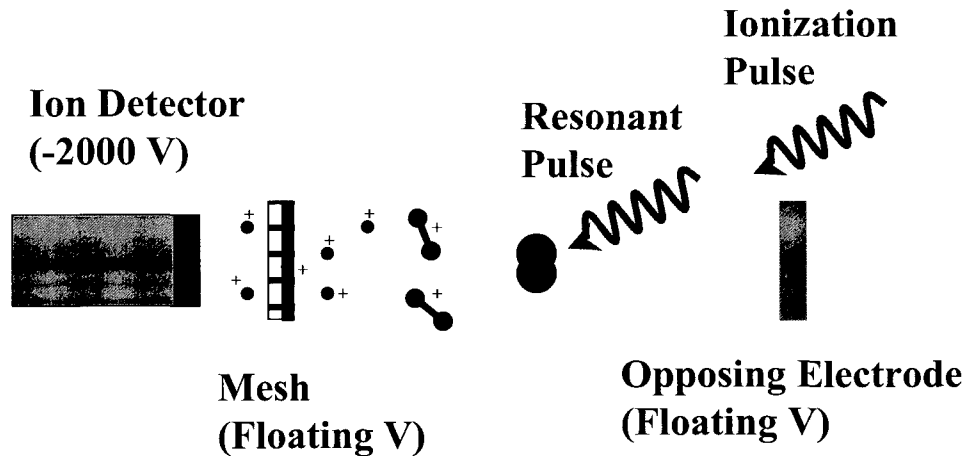


Figure 3.6: Schematic representation of ion detection using 1+1 REMPI. Resonant pulses that first excite and then ionize atoms, molecules, or both depending on the frequency of the resonant step hit the atoms and molecules in the sample. The positive ions created by the pulses are drawn into the ion detector and register a signal. The ions pass through a mesh for another application that is allowed to float relative to the other voltages in the vacuum chamber during the ion detection process. The signal generated by the ions is proportional to the mass of the ion due to the distance the ion must cover between the trap location and the detector.

3.4.2 Lifetime Measurements

The primary use for REMPI with atoms was to optimize the alignment of the lattice by maximizing the lifetime of the atoms in the trap. The high gain of the ion detector allowed the small signals at long timescales to be detected. Maximizing these signals provided fine alignment of the retroreflected lattice beam.

The trap lifetime measurement was performed by loading Rb atoms with a molasses stage and then detecting atomic ions via REMPI after a variable hold time. Figure 1.4 shows a typical long-timescale lifetime measurement of the trap.

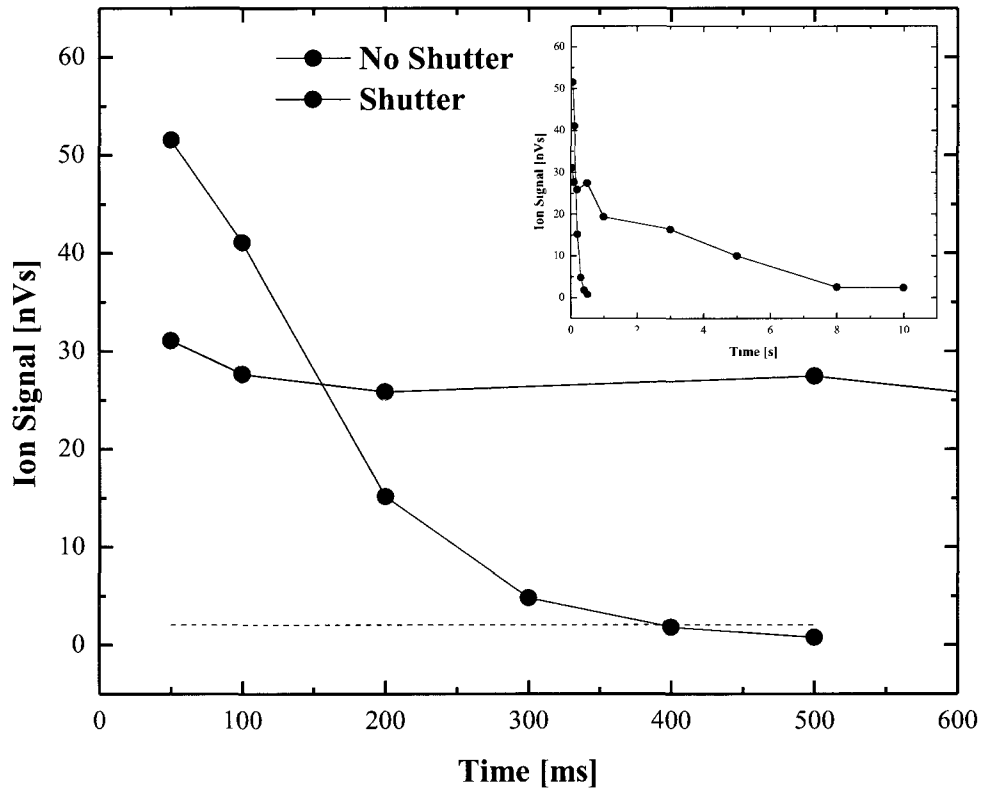


Figure 3.7: Difference in trap lifetime with and without a shutter positioned before the fiber coupler that transfers the MOT trap light to the experiment. The dramatic reduction in lifetime with the shutter open is due to leakage of resonant trap light into the fiber and subsequently the apparatus. There is enough trap light coupled into the fiber even when the switching AOMs are off that the scatter reduces the trap lifetime by an order of magnitude. The inset shows the full trapping time with the shutter closed. The dashed line is the approximate noise floor of the measurement, and the solid lines connecting the points are to guide the eye.

The figure illustrates a key point; even if an AOM is off there is non-zero overlap between the undeflected beam passing through the AOM and a fiber coupler optimized for the deflected beam when the AOM is on. This light is capable of reducing the trap

lifetime by an order of magnitude due to light-assisted collisions. Without using a shutter to filter out this resonant leakage light, the $1/e$ lifetime of the atoms in the lattice was on the order of 100 ms. Once the shutter was installed, the atom lifetime improved to 1.5 s which was consistent with the background pressures in the low 10^{-9} torr in the chamber.

4. Basic Molecular Theory

4.1 Introduction

A molecule has multiple nuclei that create an electric field that is not spherically symmetric from the point of view of its constituent electrons. As a result molecules have vibrational and rotational degrees of freedom in addition to the translational and electronic motion that atoms also possess. An exact description of the molecule's states is a very difficult problem even for the diatomic molecules we consider. Our ultimate goal is to find separable expressions for the molecule wave function⁶⁰

$\Psi = \Psi_{trans} \Psi_{elec} \Psi_{vib} \Psi_{rot}$ that allow us to deal with each degree of freedom separately.

This is a logical course, because the energy scales of each degree of freedom are very different. The rotational contribution to the energy is on the order of 10 cm^{-1} , the vibrational energy is near 10 cm^{-1} , while the electronic energy is 1000 cm^{-1} . In practice a separable form of the wavefunction cannot be found exactly, but we can make a series of approximations that allow us to come close enough to use perturbation theory to generate useful results. In this section we will summarize some basic theory that allows us to use these techniques to understand molecular transitions.

4.1.1 The Born-Oppenheimer Approximation

We will consider a molecule that consists of two nuclei A and B interacting with some number of electrons only through the Coulomb force. The wavefunction of the

system is a function of the nuclear coordinates \bar{R}_A, \bar{R}_B and the electron coordinates \vec{r}'_j , and it can be separated into internal and external parts. This is done by applying a coordinate transformation to a coordinate system with its origin at the center of mass of the molecule so that we can write

$$\Psi(\bar{R}_A, \bar{R}_B, \vec{r}'_j) = \Psi_{ext}(\bar{R}_{CM}) \Psi_{int}(\bar{R}, \vec{r}_j) . \quad (4.1)$$

Here \bar{R}_{CM} is the vector from the original origin to the center of mass of the molecule in the original coordinate system. The new electron coordinates $\vec{r}_j = \vec{r}'_j - \bar{R}_{CM}$ and the internuclear vector is defined as $\bar{R} \equiv \bar{R}_A - \bar{R}_B$. This transformation moves the problem to a molecule-fixed frame and leaves us free to ignore $\Psi_{ext}(\bar{R}_{CM})$ and as a result, the overall translational motion of the whole molecule. This separation is justified in general because translation is a symmetry operation in a field-free region of space.

Unfortunately, the Schrodinger equation

$$H\Psi_{int}(\bar{R}, \vec{r}_j) = E\Psi_{int}(\bar{R}, \vec{r}_j) , \quad (4.2)$$

is still intractable, so we invoke the Born-Oppenheimer approximation to further break the problem down.

We assume that the nuclei are extremely slow moving relative to the motion of the electrons and regard them as fixed in space, which removes their kinetic energy from the Hamiltonian. This is a reasonable assumption from the point of view of classical mechanics since the typical mass of a nucleus is four orders of magnitude higher than that of an electron. A given electron is now moving in an electrostatic potential $V_{elec}(R, \vec{r}_j)$

that is a function of static nuclear separation and the electron coordinates. The wavefunction $\Psi_{elec}(R, \vec{r}_j)$ satisfies the equation

$$\left[\sum_j \frac{1}{2m} \mathbf{P}_j^2 + V_{elec}(R, \vec{r}_j) \right] \Psi_{elec}(R, \vec{r}_j) = E_{elec}(R) \Psi_{elec}(R, \vec{r}_j), \quad (4.3)$$

where m is the mass of the j^{th} electron and $E_{elec}(R)$ is an electronic eigenvalue at a fixed internuclear distance R . Equation (4.3) can be repeatedly solved for many different values of R to yield many pairs of $E'_{elec}(R')$ and $\Psi'_{elec}(R', \vec{r}_j)$. These values can be compiled to define the dependence of both the eigenfunctions and wavefunctions as a function of the internuclear separation and so produce $\Psi_{elec}(\vec{R}, \vec{r}_j)$ and $E_{elec}(\vec{R})$.

Having found the electronic wavefunction we now assume the total wave function has the separable form

$$\Psi_{\text{int}}(\vec{R}, \vec{r}_j) \approx \Psi_{elec}(\vec{R}, \vec{r}_j) \Psi_N(\vec{R}), \quad (4.4)$$

where $\Psi_N(\vec{R})$ is the nuclear wave function that only depends on the internuclear coordinate. This treatment allows us to write separate Schrodinger equations for the electrons and nuclei, and we have used (4.3) to solve for the electron wavefunctions and eigenvalues. We now switch our point of view to that of the nuclei, which move under an effective potential $E_{elec}(\vec{R}) + V_N(\vec{R})$ where the second term is the internuclear potential energy.

Under the Born-Oppenheimer approximation we assume that because the electrons move so much faster than the nuclei they are able to adiabatically follow changes in the nuclear momenta and position. This amounts to inserting (4.4) into (4.2)

and neglecting terms that contain derivatives of electronic wavefunctions with respect to the nuclear coordinates. This procedure yields an equation for the nuclear motion

$$\left[\frac{1}{2\mu} \mathbf{P}_N^2 + E_{elec}(\vec{R}) + V_N(\vec{R}) \right] \Psi_N \vec{R} = E_{VR} \Psi_N \vec{R} . \quad (4.5)$$

Here \mathbf{P}_N^2 is the nuclear momentum operator, and E_{VR} is the nuclear eigenfunction. This result allows us to calculate the wavefunction for motion of the nucleus under the effective potential, and under these assumptions express the total energy of the molecule as $E = E_{elec} + E_{VR}$. The procedure described above generates electronic potentials that contain separable manifolds of vibrational potentials that are due to the motion of the nucleus.

In reality, the nuclei must always move some amount, but the Born-Oppenheimer approximation will approximately hold as long as the nuclei move slowly enough that the electron cloud of the molecule can quasi-statically adjust to the new internuclear potential. Perturbation theory can be used to account for the unused terms in the Hamiltonian to give a more accurate description of the actual molecular levels. We are free to expand our wavefunction as a complete set of spherical harmonics. When we do this we find that the expression (4.5) becomes

$$\left[\frac{1}{2\mu} \mathbf{P}_v^2 + E_{elec}(\vec{R}) + V_N(\vec{R}) + \frac{\hbar^2 J(J+1)}{2\mu R^2} \right] \Psi_v \vec{R} = E_v \Psi_v \vec{R} . \quad (4.6)$$

This equation can be solved in general by using the Dunham expansion⁶¹ for strongly bound states or numerical refinements on it for higher lying excited states.

We have now fully separated the molecular wave function into its constituent parts, and have gained a manifold of rotational levels that are perturbations on each vibrational manifold.

In general, the atoms that make up molecules have internal spins and the coupling of these spins to each other and the overall rotation of the molecule must be calculated on a case-by-case basis. There are differences in the calculations based on the relative strength of the spin-orbit, rotational, and electronic (Born-Oppenheimer) interactions. The different types of interaction between the various angular momenta of the molecule are called Hund's coupling cases and are discussed below.

4.1.2 Molecular State Labeling and Selection Rules

Because diatomic molecules do not have spherical symmetry the usual atomic quantum numbers are not necessarily constants of molecular motion.

We define the internuclear axis $\hat{z} = \hat{R}$ as the quantization axis and assign the quantum number \mathbf{N} to rotational angular momentum of the nuclei in the plane perpendicular to \hat{R} . In general we can define a quantum number \mathbf{J} that is the total angular momentum of the system. The projection of \mathbf{J} along the internuclear axis is defined as the quantum number $\mathbf{\Omega}$. For the cases most relevant to this experiment (Hund's cases (a) and (c)), $\mathbf{\Omega}$ is always a good quantum number, but the specifics of how \mathbf{J} is formed depend on the relative strengths of the couplings between the internuclear axis and the electronic angular momenta. It is still useful to think about the total orbital electronic angular momentum quantum number \mathbf{L} and the total electron spin \mathbf{S} even if they are not good quantum numbers. The differentiation between coupling cases depends on whether

L and **S** couple more strongly to each other or are coupled to the molecular axis by the internuclear electric field. The different sets of coupling are called Hund's cases and we will outline Hund's cases (a), (b), and (c) as they are most directly applicable to the work in this thesis.

Hund's case (a) is the limit of small spin-orbit coupling where both **L** and **S** couple much more strongly to the internuclear axis than each other. It is the usual coupling system for deeply bound vibrational levels of a molecule. In this case we can define the total angular momentum of the system as $\mathbf{J} = \mathbf{N} + \mathbf{L} + \mathbf{S}$. The projection of **L** onto the nuclear axis is a good quantum number with possible values

$M_L = -L, -L+1, \dots, L-1, L$. We define the projection of **L** as the vector Λ along \hat{R} with a magnitude

$$\Lambda = |M_L|. \quad (4.7)$$

Similarly, the total electron spin is **S** it has a projection Σ along \hat{R} that can take on values $\Sigma = -S, -S+1, \dots, S-1, S$. Σ is also a good quantum number and allows us to write Ω as vector sum of Σ and Λ with a magnitude

$$\Omega = |\Lambda + \Sigma|. \quad (4.8)$$

The conventional way to label electronic states of molecules in Hund's case (a) is

$$^{2S+1}\Lambda_{\Omega}^{\pm}, \quad (4.9)$$

where we can see that the molecular states have a multiplicity of $2S+1$. The naming convention for labeling electronic states of progressing Λ is to write $\Lambda=0, 1, 2, \dots$ as $\Lambda=\Sigma, \Pi, \Delta, \dots$ states. For states with zero total angular momentum (Σ) there is an additional symmetry that is included in the state labeling as the \pm superscript in (4.9). The label

specifies the sign change of the electronic wave function when it is reflected through the plane defined by the nuclear axis. The good quantum numbers in this coupling case are $\Omega, J, \Sigma, \Lambda$, and m_J . The last quantum number, m_J is defined as the projection of \mathbf{J} along the internuclear axis in the laboratory frame.

Hund's case (b) uses similar quantum numbers to Hund's case (a), but it is the special situation where \mathbf{S} is very weakly coupled to the internuclear axis. It can arise for light atoms or heavy atoms with $\Lambda=0$ but $\mathbf{S} \neq 0$, which applies in the lowest triplet state of the RbCs molecule (and all other alkalis). Since \mathbf{S} is decoupled from the nuclear axis Ω

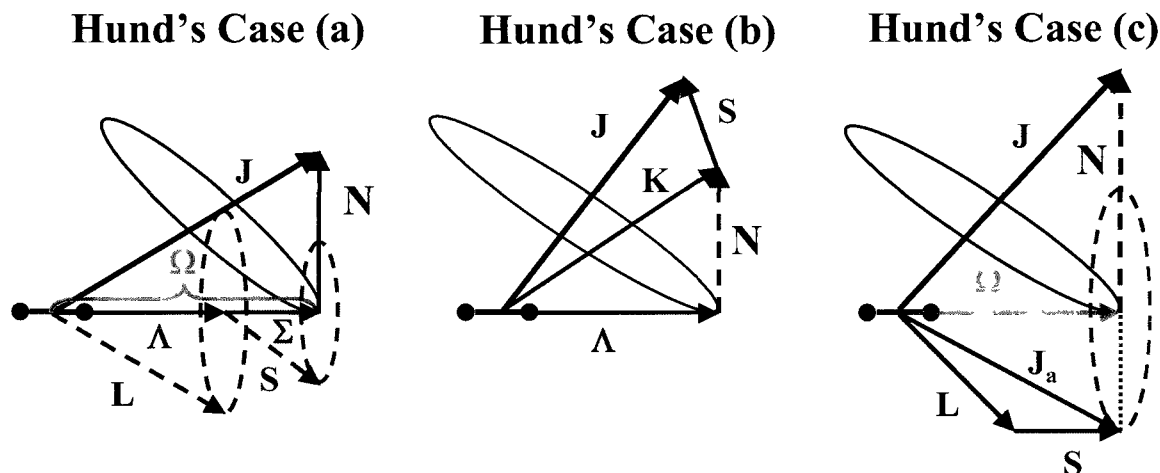


Figure 4.1: Vector Diagrams of relevant Hund's cases. Left: a schematic representation of Hund's Case (a). The \mathbf{L} and \mathbf{S} couple strongly to the internuclear axis leading to well-defined values of Λ and Σ Center: A schematic representation of Hund's Case (b). \mathbf{S} is uncoupled from the nuclear axis, leaving Σ undefined. Right: Hund's Case (c), where \mathbf{L} and \mathbf{S} couple to each other to form the vector \mathbf{J}_a which in turn precesses around the internuclear axis.

and Σ are no longer defined. Instead we form a vector $\mathbf{K} = \mathbf{L} + \mathbf{N}$ with allowed values $\mathbf{K} = \Lambda, \Lambda + 1, \Lambda + 2, \dots$ that couples to \mathbf{S} and forms \mathbf{J} . The good quantum numbers in this coupling case are $\Omega, \mathbf{J}, \Lambda$, and m_J .

Hund's case (c) is the case where the spin-orbit interaction is large compared to the coupling of \mathbf{L} and \mathbf{S} to the molecular axis. This case arises in our experiments for

vibrational levels high in the Born Oppenheimer potentials. These weakly bound states have a smaller internuclear electric field because the nuclei are relatively far apart on average. Because \mathbf{L} and \mathbf{S} couple more strongly to each other than to the internuclear axis we define a vector $\mathbf{J}_a = \mathbf{L} + \mathbf{S}$ that couples to \hat{R} with a projection Ω that is a good quantum number. The total angular momentum is defined as $\mathbf{J} = \mathbf{J}_a + \mathbf{N}$ and it is also a good quantum number in case (c). Because Σ and Λ are undefined in this case the only good quantum numbers are Ω , \mathbf{J} , and m_J . States in this coupling scheme are labeled Ω^\pm where in this case the \pm superscript refers to the reflection symmetry of the entire electron wave function through the internuclear axis.

4.1.3 Electric Dipole Transitions in Molecules

Transitions between different electronic states in the molecule depend on the value of the matrix element between the initial and final state of the transition. We consider electric dipole transitions, which have matrix elements of the form⁶²

$$\langle \Psi_f(R, r) | \mathbf{d} \cdot \mathbf{E} | \Psi_i(R, r) \rangle, \quad (4.10)$$

where $|\Psi_i(R, r)\rangle$ is the initial state wave function in the Born-Oppenheimer approximation, $|\Psi_f(R, r)\rangle$ is the final state wave function, \mathbf{E} is the electric field driving the transition, and \mathbf{d} is the electric dipole operator. In order to evaluate these overlap integrals we assume that an electronic transition happens on a time scale much shorter than that for a single vibration. This allows us to write the total wavefunction as a function with separable electronic and vibrational components $\Psi(R, r) = \Psi_e(\bar{R}, r)\Psi_v(R)$.

In order to assume separability we must remove the dependence of the electronic wavefunction on R , so we have evaluated the wavefunction at the average internuclear distance. Note that we are neglecting the coupling of rotation to the electronic motion for this treatment, it can be thought of as part of the electronic wave function for now. Using the separable form of the wave function we can write (4.10) as

$$\langle \Psi_{ef}(\bar{R}, r) | \mathbf{d} \cdot \mathbf{E} | \Psi_{ei}(\bar{R}, r) \rangle \langle \Psi_{vf}(R) | \Psi_{vi}(R) \rangle. \quad (4.11)$$

The first term is the usual electric dipole matrix element that can be calculated using well-known techniques. The second quantity is an overlap integral between the initial and final vibration state wavefunctions. It is important to note that the two vibrational functions are parts of two different electronic Born-Oppenheimer potentials. There is no requirement that vibrational levels must be orthogonal and there are no restrictions on Δv for a vibrational-electric transition. From the expression (4.11) we observe that the strength of the electronic transition is proportional to the familiar dipole matrix element for atomic transitions and the quantity $|\langle \Psi_{vf}(R) | \Psi_{vi}(R) \rangle|^2$, which is known as the Franck-Condon factor. The Franck-Condon factor will typically be maximized at the outer portions of the electronic potential. This is where the vibrational wave functions have the highest overlap integrals. This increases the probability of transition, so for maximum transition probability we select vibrational levels that have electronic potentials that line up along their classical turning points. The internuclear distance at which this turning point occurs is known as the Condon Radius R_c and is illustrated in figure 3.2.

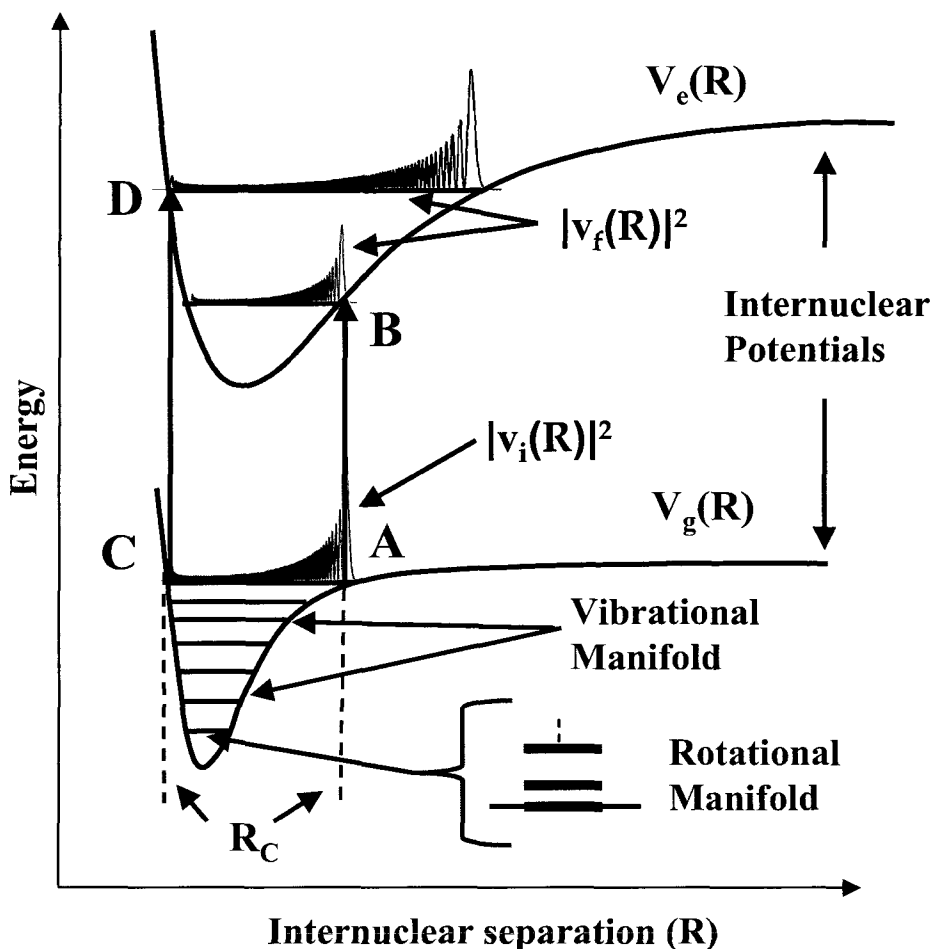


Figure 4.2: The structure of Born Oppenheimer potentials showing the ground (V_g) and first excited electronic state (V_e). The ground state vibrational and rotational level manifolds are illustrated schematically. The probability amplitudes for states at representative vibrational levels in the ground (v_i) and excited states (v_f) are shown. Two transitions from A-B and C-D with large Franck-Condon factors are shown. They take place at the Condon radius R_c with different excited vibrational states overlapping with the inner and outer turning points of the electronic ground state.

The other important aspect of electronic dipole transitions in molecules is the coupling between the electronic and rotational degrees of freedom. The various Hund's cases give rise to different types of symmetry that govern which quantum numbers are well defined. Because each coupling case has different good quantum numbers each Hund's case has different selection rules⁶³ for the determination of non-zero electric dipole matrix elements between molecular states.

First, we have the general rule that always applies to molecules

$$\begin{aligned} \Delta J &= 0, \pm 1 \\ \text{with} & \\ J = 0 &\not\leftrightarrow J' = 0. \end{aligned} \quad (4.12)$$

For cases (a) and (b) we have the rules

$$\Sigma^+ \leftrightarrow \Sigma^+, \Sigma^- \leftrightarrow \Sigma^-, \Sigma^+ \not\leftrightarrow \Sigma^-, \quad (4.13)$$

$$\Delta \Lambda = 0, \pm 1, \quad (4.14)$$

$$\Delta S = 0. \quad (4.15)$$

For cases (a) and (c) we have

$$\begin{aligned} \Delta \Omega &= 0, \pm 1 \\ \text{with} & \\ J = 0 &\not\leftrightarrow J' = 0, \end{aligned} \quad (4.16)$$

and case (c) has a selection rule analogue to (4.13)

$$0^+ \leftrightarrow 0^+, 0^- \leftrightarrow 0^-, 0^+ \not\leftrightarrow 0^-. \quad (4.17)$$

For case (a) alone we have the rule

$$\Delta \Sigma = 0. \quad (4.18)$$

Similarly, for case (b) alone the final selection rule is

$$\Delta K = 0, \pm 1. \quad (4.19)$$

It is important to recall that, while these selection rules are excellent guidelines, the good quantum numbers available for a molecular transition can and often do change between the two electronic manifolds. In addition, these guidelines only apply to pure Hund's cases, so it is important to use caution when examining particular transitions.

4.2 Collision Theory

Atomic and molecular collisions play a very important role in this thesis. The way we form molecules involves the three-body collision process of photoassociation, and our principle loss mechanism in the QUEST is from inelastic background collisions. The principle measurement of this work is the collisional properties of ultracold molecules and in order to understand the results of these experiments we need some background in collision physics.

4.2.1 Basic Elastic Collision Theory

The basic theory of atomic scattering has a long and rich history. We will sketch an outline of the important basic concepts here loosely following the work of Sakurai,⁶⁴ Julienne,⁶⁵ and Taylor⁶⁶. We will consider a collision between two distinguishable particles that have an interaction potential $V_g(R)$, where \mathbf{R} is the vector connecting the two particles that are moving relative to one another with a momentum \mathbf{k} . In scattering theory we refer to channels, or specific states, for the particles before and after a collision. If we label our particles a and b we have an incoming channel corresponding to the free atoms $a + b$ with individual momenta k_a and k_b that add up to \mathbf{k} . After the collision event we could have two free atoms with various individual momenta that still add up to \mathbf{k} . These outgoing channels that produce free atoms in the same state, but with possible different kinetic energies are known as elastic collision channels. We could also have outgoing channels (ab) that are bound molecular states of various internal energies. These channels, along with any others that transfer the energy of the colliding

atoms to internal degrees of freedom of one or both of the colliders or vice-versa are known as inelastic channels.

The general problem in scattering is to find the probability for the scattering particles to be in the particular outgoing state Ψ_0 given the interaction potential and the ingoing Ψ_{in} and outgoing Ψ_{out} wavefunctions that are sums over all available channels. We take Ψ_{in} and Ψ_{out} to be states that are prepared long before and detected long after scattering respectively. The standard way to do this is to relate the ingoing and outgoing wavefunctions by a unitary transform such that $\Psi_{out} = \mathbf{S}\Psi_{in}$. The quantity \mathbf{S} is known as the S matrix⁶⁷, which contains has non-zero terms connecting all available scattering channels. To find the probability for the system to be in the specific outgoing state Ψ_0 we would calculate

$$|\langle \Psi_0 | \mathbf{S} | \Psi_{in} \rangle|^2. \quad (4.20)$$

We can now see that the elements of \mathbf{S} make up all the possible outcomes of a collision between the particles a and b . The diagonal terms will correspond to elastic scattering events because they leave the scatterers in the same internal states. Similarly, the off-diagonal terms will correspond to inelastic channels.

The approach above is general, and the analysis in terms of wavefunctions that are eigenfunctions of \mathbf{k} is known as the plane wave basis. All the cases of two atoms scattering that we will consider involve an interaction potential $V_g(R)$ that is spherically symmetric. This makes an expansion of the free particles in spherical-wave states $|E, \ell, m; \alpha\rangle$ a natural basis⁶⁸ with which to work. Here we have an eignestate of total energy E scattering in channel α with total angular momentum ℓ and a projection of

that angular momentum of m along a quantization axis. Because the interaction potential is invariant under rotation angular momentum is conserved in the problem and \mathbf{S} is block diagonal with elements $S_{\alpha\alpha'}^\ell(E)$ that are only functions of E and ℓ . Each block of \mathbf{S} is an $n \times n$ matrix $\mathbf{S}^\ell(E)$ associated with the n open scattering channels associated with a specific angular momentum and energy. The block diagonal structure of \mathbf{S} into matrices associated with specific angular momenta lends itself very well to partial wave decomposition. In reality the magnetic field in the apparatus is enough to break the rotational symmetry of the problem, but the effect is small enough that it can be treated as a perturbation on the overall treatment by expansion in spherical eigenstates.

In an analogy to single-channel elastic scattering, we can define a multi-channel partial wave amplitude

$$f_{\alpha\alpha'}^\ell(E) = \frac{S_{\alpha\alpha'}^\ell(E) - \delta_{\alpha\alpha'}}{2i\sqrt{k_\alpha k_{\alpha'}}}, \quad (4.21)$$

with $\delta_{\alpha\alpha'}$ the familiar Kronecker delta and k_α the magnitude of the wavevector for the channel α . It is worth noting two useful limits. First we define the expansion in the limit of a single open channel $S_{11}^\ell(E) = e^{2i\delta_\ell}$ such that we recover the usual expression for the elastic phase shift δ_ℓ . Second, to check correspondence we observe that the one channel limit of (4.21) is $f_{11}^\ell(E) = \frac{e^{2i\delta_\ell} - 1}{2ik}$ which is the expression for the elastic partial wave scattering amplitude. We also have the total scattering amplitude

$$f_{\alpha\alpha'}(\mathbf{k}_\alpha, \mathbf{k}_{\alpha'}) = \frac{1}{2i\sqrt{k_\alpha k_{\alpha'}}} \sum_\ell (2\ell + 1) [S_{\alpha\alpha'}^\ell(E) - \delta_{\alpha\alpha'}] P_\ell(\cos \theta) \quad (4.22)$$

here $P_\ell(\cos\theta)$ is a Legendre polynomial and the incoming, \mathbf{k}_α , and outgoing, $\mathbf{k}_{\alpha'}$ wavevectors are at an angle θ to one another. We are typically interested in a scattering rate for a given process, which will be related to the total cross-section for the process.

The total cross-section for a pair of atoms in channel α to scatter into channel α' is

$$\sigma_{tot}(\alpha, \alpha') = \int |f_{\alpha\alpha'}(\mathbf{k}_\alpha, \mathbf{k}_{\alpha'})|^2 d\Omega = \frac{\pi}{k^2} \sum_{\ell} (2\ell + 1) |S_{\alpha\alpha'}^{\ell}(E) - \delta_{\alpha\alpha'}|^2, \quad (4.23)$$

where conservation of energy demands that $k = k_\alpha = k_{\alpha'}$. The total cross section is related to the scattering rate constant K by the expression

$$K = \int_0^{\infty} v \sigma_{tot}(v) f(v) dv, \quad (4.24)$$

where v is the relative atomic speed and $f(v)$ is the velocity distribution of the colliding atoms. We will consider collision channels of atom pairs with reduced mass μ moving at a velocity v relative to one another. In our case we have a 3-D atomic gas with thermal distribution of velocities, so we must take a thermal average over the energies and momenta in the system in order to define a total cross-section. If we assume a Maxwell-Boltzmann velocity distribution the average velocity⁶⁹ will be $\langle v \rangle = \sqrt{\frac{8k_B T}{\pi\mu}}$ and we can

evaluate (4.24) with $k = \frac{\mu\langle v \rangle}{\hbar}$ to find the total scattering rate constant

$$\begin{aligned} K(T, \alpha, \alpha') &= \left\langle \frac{\pi v}{k^2} \sum_{\ell} (2\ell + 1) |S_{\alpha\alpha'}^{\ell}(E) - \delta_{\alpha\alpha'}|^2 \right\rangle \\ &= \sqrt{\frac{\hbar^4 \pi^3}{8\mu^3 k_B T}} \left\langle \sum_{\ell} (2\ell + 1) |S_{\alpha\alpha'}^{\ell}(E) - \delta_{\alpha\alpha'}|^2 \right\rangle. \end{aligned} \quad (4.25)$$

The above expression sheds some phenomenological light on the scattering rate if we examine the scaling of a density-dependent experimental total scattering rate constant. If our sample has atomic densities n_a and n_b this rate constant is proportional to

$$\frac{n_a n_b}{\sqrt{T}}, \quad (4.26)$$

so to increase collisions we clearly would like to minimize the sample temperature while maximizing the atomic densities. More specifics about the actual experimental system are necessary for additional insight into the photoassociation process.

4.2.2 Inelastic Collisions and Photoassociation

Photoassociation is a three-body inelastic collision between two atoms and a photon that is slightly red-detuned to an atomic transition frequency. We are free to use much of the formalism developed in the previous section, but with a few modifications due to the fact that we are dealing with three body free-to-bound transitions rather than two body bound-to-bound as the above. In order to proceed we also need to know more specific information about the interaction potential between ^{85}Rb and ^{133}Cs .

When we move to the spherical basis to use partial wave decomposition of the scattering problem, the interaction potential between the atoms takes on the long-range form

$$V(R) = -\frac{C_6}{R^6} + \frac{\hbar^2 \ell(\ell+1)}{2\mu R^2}, \quad (4.27)$$

where μ is the reduced mass. The first term of (4.27) is the van der Waals interaction between the atoms while second term is known as the centrifugal barrier. For the Rb + Cs system the centrifugal barrier occurs at an interatomic radius on the order of 50 \AA with barriers of 80 \mu K and 240 \mu K for p- wave ($\ell = 1$) and d- wave ($\ell = 2$) collisions respectively. The heights of these barriers were calculated by finding the maxima of (4.27), with $C_6 = 2.6 \times 10^7 \text{ \AA}^6 \text{ cm}^{-1}$ for RbCs molecules⁷⁰. The region where electronic transitions occur is at a nuclear separation of approximately 15 \AA , so atoms colder than the barrier heights that have angular momentum will not approach close enough to have an electronic transition. In our experiments the MOT temperatures are on the order of 100 \mu K , so the collisions are predominantly s-wave in character.

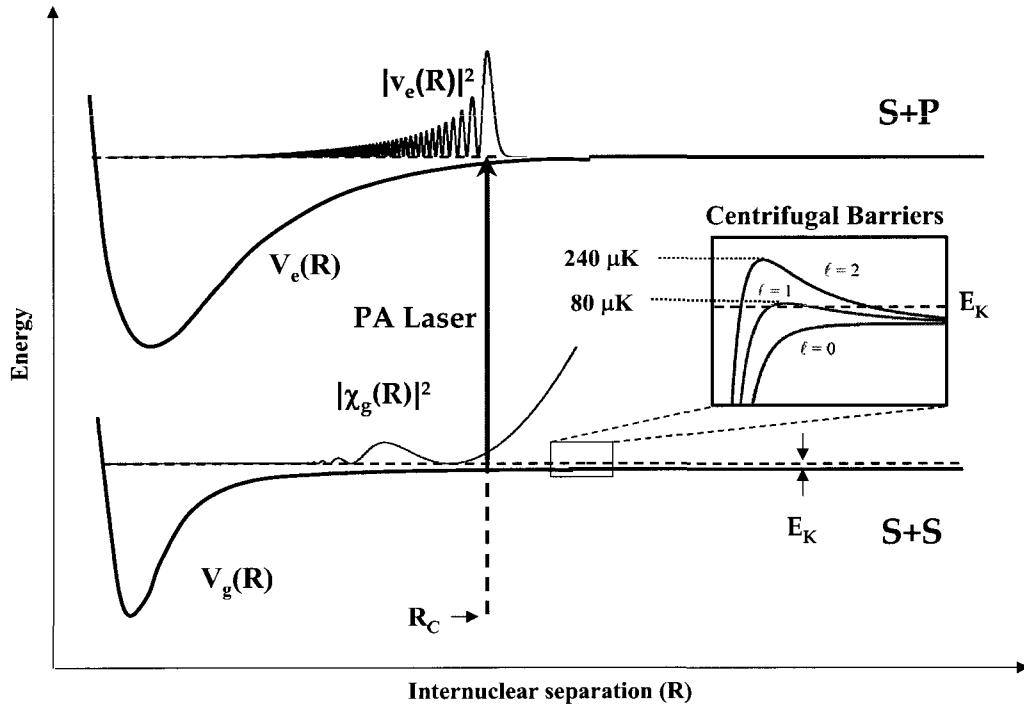


Figure 4.3: The mechanics of a free-to-bound transition for a pair of atoms that enter on a collision channel with kinetic energy E_k where both atoms are in atomic electronic S states. The inset shows the centrifugal barriers for RbCs located at a nuclear separation of roughly $100 a_0$. If the atoms are in an angular momentum state that can reach the Condon radius R_c they can be excited into a bound, electronically excited state.

We will assume only the s-wave atoms participate in the photoassociation process, which allows us to narrow our focus to matrix elements of the form S_y^0 that will greatly simplify calculations. Following the treatment of Bohn and Julienne⁷¹ we can model the photoassociation process as a single incident channel inelastic collision ignoring the atomic fine and hyperfine structure. The atoms follow their interaction potential on an initial free-atom channel, 0, and are radiatively coupled by a laser photon to a bound, electronically excited channel b . We can represent this coupling with the off-diagonal matrix element S_{0b}^0 , which must be proportional to Γ , the free to bound transition rate. In reality channel b is then coupled via spontaneous decay to many bound and free atomic channels. However, we can model b as decaying only to an artificial free-atom channel a , via the off-diagonal matrix element S_{ab}^0 . Channel a is constructed so that the coupling rate γ represents the spontaneous emission rate from b to all free and bound ground electronic states. There is no direct coupling between states 0 and b .

Explicitly evaluating these matrix elements is nontrivial and is described by Bohn, however we can gain considerable insight into the photoassociation process by virtue of being in the $k \rightarrow 0$ limit of the scattering process. Because closed channel wavefunctions are constrained to asymptotically approach zero we can use a reduced scattering matrix with a dimensionality equal to the number of open channels in the problem. In our case we are concerned with the photoassociation rate, which will be proportional to the square of the off-diagonal element $S_{0a}^{0,red}$:

$$\left| S_{0a}^{0,red} \right|^2 = \frac{\gamma \Gamma}{E - (\delta_L + E_e)^2 + \frac{\gamma + \Gamma}{2}^2}. \quad (4.28)$$

Here we have the laser detuning δ_L from the excited electronic energy E_e . The total photoassociation rate, K_{PA} will be (4.25) with (4.28) substituted for the thermally averaged matrix element.

The photoassociation rate is clearly maximized when the spontaneous emission rate γ is equal to the free-bound transition rate Γ . As Γ is increased relative to γ the coupling between the bound channel b and the continuum channel 0 grows so strong that the probability for a stimulated transition back to the continuum outstrips the probability for spontaneous decay. As a result K_{PA} decreases with increasing Γ . This continuum-coupling behavior is also the reason that stimulated transitions cannot be used to drive population into bound ground states, since any such efforts would simply couple to continuum states of free atoms with the same energy.

We have defined how the electric dipole matrix element connects the various channels in photoassociation, but in order to fully address the phenomenon we must define what we mean by a free-to-bound transition rate. We can use Fermi's golden rule to write the rate as

$$\Gamma = \frac{2\pi}{\hbar} \left| \langle \Psi_i | e\mathbf{E} \cdot \mathbf{r} | \Psi_f \rangle \right|^2, \quad (4.29)$$

where the subscripts signify the initial and final total wavefunctions of the coupled states. Even though the initial state is a free scattering state, we can still separate the wavefunctions into electronic and vibrational (nuclear) parts to write

$$\Gamma = \frac{2\pi}{\hbar} \left| \langle \Psi_{ei} | e\mathbf{E} \cdot \mathbf{r} | \Psi_{ef} \rangle \right|^2 \left| \langle \Psi_{ve}(R) | \chi(R) \rangle \right|^2. \quad (4.30)$$

Where the first term is the square of the usual electronic dipole matrix element and the second term is known as the free-bound Frank-Condon factor. This term describes the

overlap of the bound excited state wavefunction with the free scattering state $|\chi(R)\rangle$.

The scattering state can be reasonably approximated by the WKB method as

$$|\chi(R)\rangle = \left(\frac{2\mu}{\pi\hbar^2 k(R)} \right)^{\frac{1}{2}} \sin\left(\sqrt{\frac{2\mu(E - V_g(R))}{\hbar^2}} R + \phi \right), \quad (4.31)$$

where the kinetic energy of the atoms is $E - V_g(R)$. In contrast to the bound-to-bound situation, the free-to-bound Condon Radius is defined solely by the outer turning point of the excited potential. This is due to the fact that the incoming scattering state cannot be peaked because it is not bound in the ground state potential. The total photoassociation rate still depends on the strong overlap between the nuclear portions of the free and bound states, so this must be a strong consideration in choosing transitions.

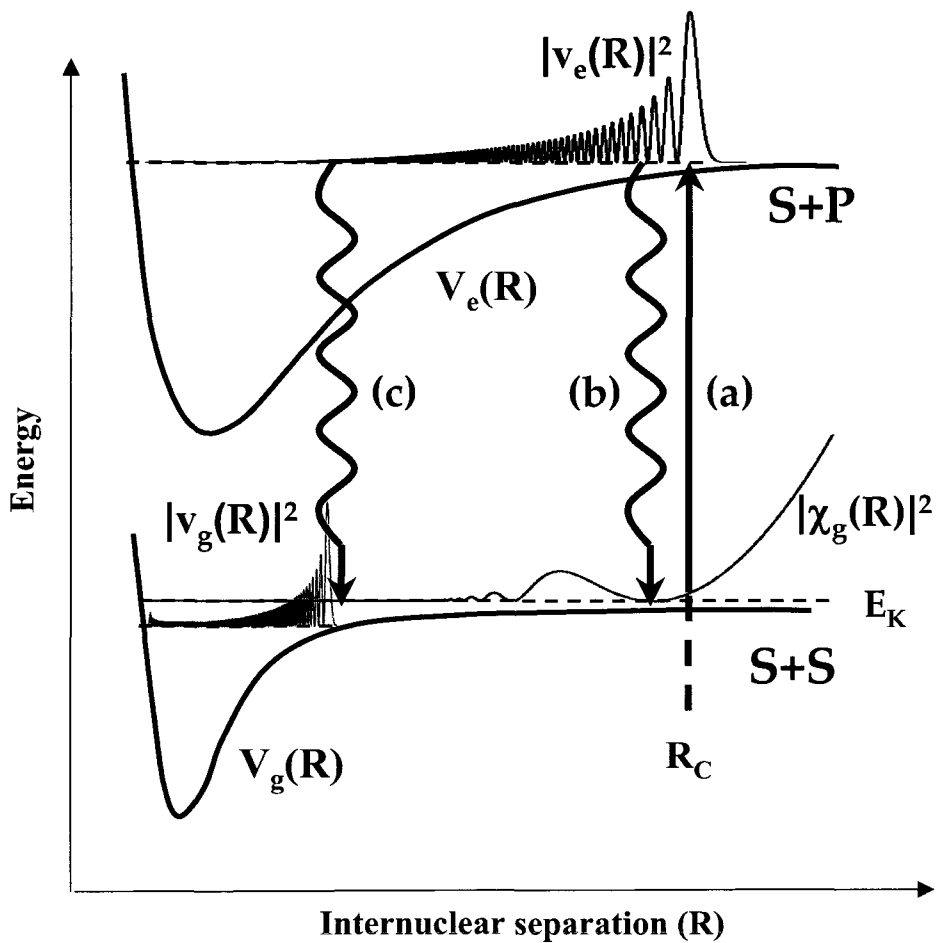


Figure 4.4: The process of photoassociation. The free atoms enter on a ground state potential well until they reach the Condon Radius R_C where they are (a) excited by a laser photon into the excited potential. From here they can spontaneously emit into either free atom (b) or bound (c) states of the ground state potential.

5 Measurement of RbCs Collision Rates

The principal result of this thesis was the measurement of the collision cross-section between RbCs in various vibrational states and with Rb and Cs atoms. In this chapter we describe the experimental apparatus and the results of the measurements. Finally, we describe a model of the observed inelastic collision processes.

The experiment consists of overlapping two dark spot MOTs with the optical lattice and then switching on a photoassociation beam that loads molecules directly into the lattice. Then, if desired, Rb or Cs atoms are loaded into the lattice using an optical molasses stage. After a variable time a particular vibrational level of the RbCs population is state selectively ionized and detected using time of flight mass spectrometry. By mapping out the survival rate of molecules in this state as a function of time, we obtain the lifetime of molecules with specific vibrational quantum numbers in the presence of an atomic species. This in turn tells us the collisional cross sections of RbCs with Rb or Cs in these specific vibrational states.

5.1 Experiment Overview

The vacuum apparatus is exactly the same as described in chapter 2. The starting point for these experiments was loading Rb and Cs dark spot MOTs that were overlapped well with each other and the QUEST beam. After loading the MOTs for 5 s, we captured $(9 \pm 1) \times 10^7$ rubidium atoms in a forced dark spot MOT at a temperature of $80 \pm 25 \mu\text{K}$ and a density of $(4 \pm 2) \times 10^{11} \text{ cm}^{-3}$. We overlapped this with a forced dark spot cesium MOT that captured $(2 \pm 1) \times 10^8$ atoms at a temperature of $105 \pm 40 \mu\text{K}$ and a

density of $(5 \pm 1) \times 10^{11} \text{ cm}^{-3}$. The optical lattice was implemented as described in chapter 3.

In this section we will explain the use of the ion detector, the two additional lasers required for state-selective ionization, and the push beams that allow the creation of a pure trapped sample of molecules.

5.1.1 Experimental Photoassociation

The specific RbCs states and potentials relevant for our experiment are shown in figure 5.1. For these measurements we chose to photoassociate to an excited, bound molecular state near the Rb $5S_{1/2}(F=2) + \text{Cs } 6P_{1/2}(F=3)$ atomic asymptote. The specific state to which we photoassociate is an $\Omega=0^-$, $J^P=1^+$ level that lies 38.02 cm^{-1} below this asymptote. Note that the molecular states are labeled in the spectroscopic convention where the lowest observed singlet state is called the “X” state and the lowest observed triplet state is labeled the “a” state. The states are then labeled by ascending energy as A, B... for the singlets and b, c... for the triplets. We detuned our laser to the red of the Rb $5S_{1/2}(F=2) + \text{Cs } 6P_{1/2}(F=3)$ atomic asymptote to form excited, bound molecules that could decay to the stable $a^3\Sigma^+$ ground state. Based on previous work⁷² the photoassociation level was chosen because it provided favorable Franck-Condon Factors for populating the $a^3\Sigma^+$ electronic ground state through spontaneous decay, while avoiding predissociation.

The Rb $5S_{1/2}(F=2) + \text{Cs } 6P_{3/2}(F=3)$ asymptote has a slightly higher energy than the Rb $5S_{1/2}(F=2) + \text{Cs } 6P_{1/2}(F=3)$ asymptote. This means that if one tries to photoassociate to the $5S_{1/2}(F=2) + \text{Cs } 6P_{3/2}(F=3)$ state there will be a continuum of unbound levels associated with the Rb $5S_{1/2}(F=2) + \text{Cs } 6P_{1/2}(F=3)$ asymptote that will

have nearly the same energy as the targeted photoassociation state. This allows the desired bound state to couple to the continuum and dissociate into their constituent atoms soon after formation. This process is known as predissociation⁷³ and we avoid it by choosing the lowest energy atomic asymptote that has no lower energy continuum states to couple to. Avoiding predissociation increases the chances of producing the bound molecules that interest us.

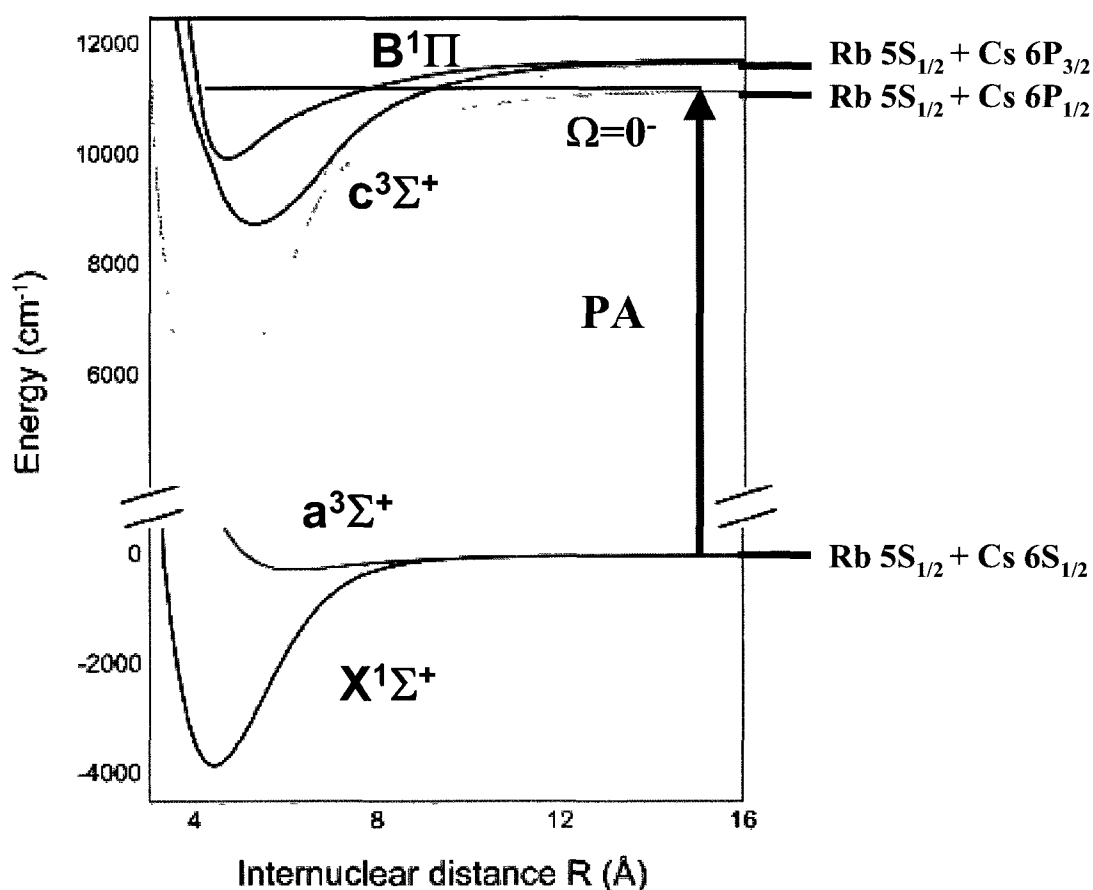


Figure 5.1: RbCs levels used in photoassociation. The PA laser is detuned to the red of the Rb 5S_{1/2} + Cs 6P_{1/2} asymptote to avoid predissociation. The ground and electronic excited states are labeled using Hund's case (a) notation. The long-range area of the excited state potential to which we actually photoassociate is better described by its Hund's case (c) quantum number Ω . The horizontal line within the electronically excited potential represents a specific vibrational level to which we photoassociate.

We generate the light used to photoassociate the molecules with a commercial tunable Ti: Sapphire laser, the Coherent 899-29. This laser is pumped by a frequency doubled, diode-pumped Nd: YVO₃ Coherent Verdi V-10 laser. The Verdi had an output power of 10W which resulted in 1W of output power from the 899 near our chosen operational wavelength of ~ 897 nm. The Ti: Sapphire laser is internally stabilized to a line width of roughly 1 MHz. It was focused onto the lattice using a 50 cm focal length lens that resulted in a 270 ± 20 μm beam waist at the molecules. For our typical operating powers this resulted in a photoassociation intensity of 3.4 MW/m^2 at the atoms.

A portion of the Ti: Sapphire laser output was coupled into a Burleigh WA-1500 wavemeter that had an absolute accuracy of 150 MHz. Simultaneously, another small portion of the Ti: Sapphire output power was coupled into a Fabry-Perot cavity along with a small amount of Cs repump light. The output of the photodiode for the cavity was digitized using a National Instruments PCI 6024-E board and read into the experimental control program. Our Labview program allowed us to adjust the frequency of the Ti: Sapphire laser while monitoring the wavemeter to find a photoassociation resonance. Because the line width of the photoassociation transitions (~ 15 MHz) is well below the resolution of the wavemeter, we located the center of the photoassociation line by manually scanning the Ti: Sapphire to maximize the RbCs⁺ ion signal.

Once the photoassociation resonance was found, a peak-finding algorithm combined with a simple PID software servo stabilized the Ti: Sapphire frequency relative to the Cs repump frequency. We applied two analog voltages to the laser. The first voltage is an offset that moves the laser by 2 MHz jumps limited by the voltage scan resolution of the laser. This is the signal we use to find the PA line. After the line is

located, the software PID loop is engaged and applies active feedback in the form of the second voltage to stabilize the laser at the photoassociation frequency. The repump was chosen as a reference frequency because it had a mean time to unlocking on the order of days.

5.1.2 Ion Detection

Excited electronic state molecules created via photoassociation can decay into free atoms, or into vibrationally excited bound molecules in the electronic ground state. Because Rb and Cs atoms each have one unbound electron, RbCs can be formed in singlet ($X^1\Sigma^+$) and triplet ($a^3\Sigma^+$) bound electronic ground states.

Because we photoassociate to a $\Omega=0^-$ level, the electronically excited molecules we form are forbidden by selection rules from decaying to the ($\Omega=\Lambda+\Sigma=0^+$) $X^1\Sigma^+$ state. In contrast, the $a^3\Sigma^+$ state has both $\Omega=0^-$ and $\Omega=1^\pm$ character that comes about due to the details in the recoupling of angular momenta in Hund's case (c) notation. For our purposes it is sufficient to note that this is the bound state to which an excited $\Omega=0^-$ molecule must decay. It has been found previously⁷⁴ that roughly 30 % of the bound molecules decay to the vibrational level with a binding energy of $E_B = -5.0 \pm 0.6 \text{ cm}^{-1}$ which we assign the vibrational number v_0 . This level has been previously assigned as $v_0 = 37$, but due to the uncertainty in the depth of the triplet potential well this assignment has an uncertainty of at least one vibrational number. Once we have populated v_0 we state-selectively detect the molecules using resonance enhanced multiphoton ionization.

The ions were created using pulsed lasers to perform both steps of the ionization process. Pulsed lasers were originally chosen because of their ability to deliver large instantaneous power over a wide range of wavelengths. This was convenient for the

original molecular spectroscopy work, as it ensured one could saturate transitions with small Franck-Condon factors over many states. It is convenient to have independent lasers because it becomes much easier to avoid background signals due to multi-photon processes by using too much power. This is particularly true in the ionization step, which can off-resonantly ionize Cs_2 molecules as well as atoms.

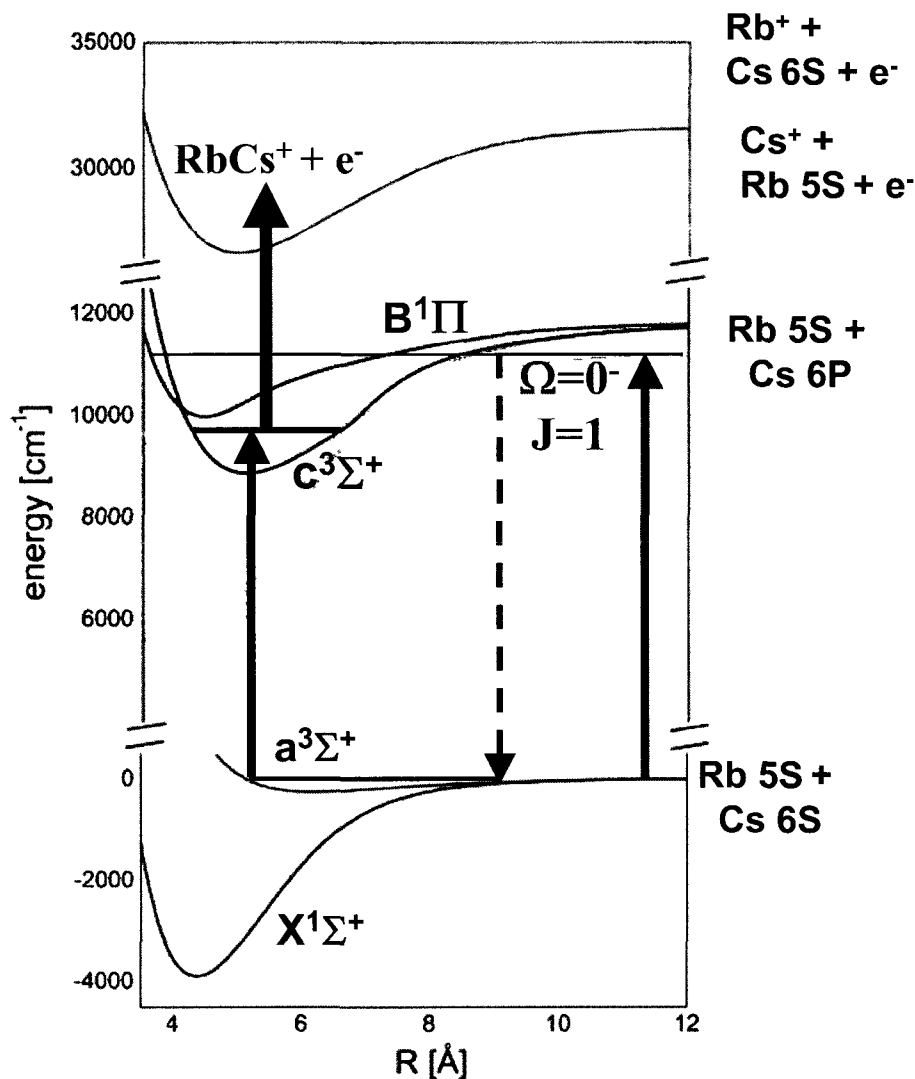


Figure 5.2: The relevant steps and levels involved in detecting triplet state molecules. First, the cold atoms are photoassociated into a bound $\Omega=0^-$ state. This state decays prominently into the bound $a^3\Sigma^+$ electronic level, but the resultant molecules are spread over a number of vibrational levels. The $a^3\Sigma^+$ molecules are state-selectively excited via the $c^3\Sigma^+$ state by a tunable dye laser, and then photoionized.

The pulsed laser light for the resonance and ionization detection steps was provided as follows. A Sirah Cobra tunable dye laser was pumped at 532 nm by the second harmonic of a SpectraPhysics Quanta Ray Pro-Series pulsed Nd: YAG laser. The Nd: YAG operates at 10 Hz with a 220 mJ pulse energy at 532 nm. Both the dye laser and the pump laser provided pulses with 7 ns duration. A portion of the 532 nm light (a few mJ) was diverted before pumping the dye laser; this 532 nm pulse was used to provide the light for the ionization step.

When detecting RbCs molecules, the dye circulator in the Sirah laser was filled with Pyrromethene 597 dye dissolved in ethanol with a concentration of 0.16 g/L. The maximum dye laser power output is specified as 20 mJ/pulse. Note that this value is not the maximum power output that the laser could achieve; it is the upper limit of the damage threshold of the laser. We succeeded in damaging the dye cell by “optimizing” our output power to 30 mJ per pulse.

The dye laser light is passed through a commercial H₂ Raman cell in order to reach the actual transition wavelengths. This cell writes sidebands split by the H₂ ground state vibrational splitting of 4155.25 cm⁻¹ onto the pulsed laser wavelength. The various frequencies were spatially separated from one another using a prism.

The 532 nm ionization pulse is directed through a 3m optical delay path to ensure that it arrived at the molecules ~10 ns after the resonant dye pulse. We typically operated with 2 mJ/pulse of 532 nm light reaching the sample in an oblong beam profile that was 200 μm wide by 500 μm high. For the resonant excitation we used a 1 mJ pulse from the second Stokes order of the H₂ Raman cell (~1040.5 nm) whose profile was 250 μm wide by 380 μm high.

A portion of the unshifted dye laser light is diverted to a Coherent Wavemate wavemeter to monitor the pulse laser's frequency. This wavelength is stabilized by servoing the dye laser grating using a simple PID loop that takes advantage of the GPIB interface available for our wavemeter. Our Labview program is able to communicate with the Sirah laser via an RS232 interface combined with Labview compatible software from the manufacturer. The software allows us to servo the dye laser wavelength by adjusting its internal grating. The resonant light from the dye laser maximizes the REMPI signal by driving population out of the $a^3\Sigma^+$ ($v=v_0$) state at an unshifted wavelength of 585.065 nm if one uses the second Stokes order to generate the resonant pulse.

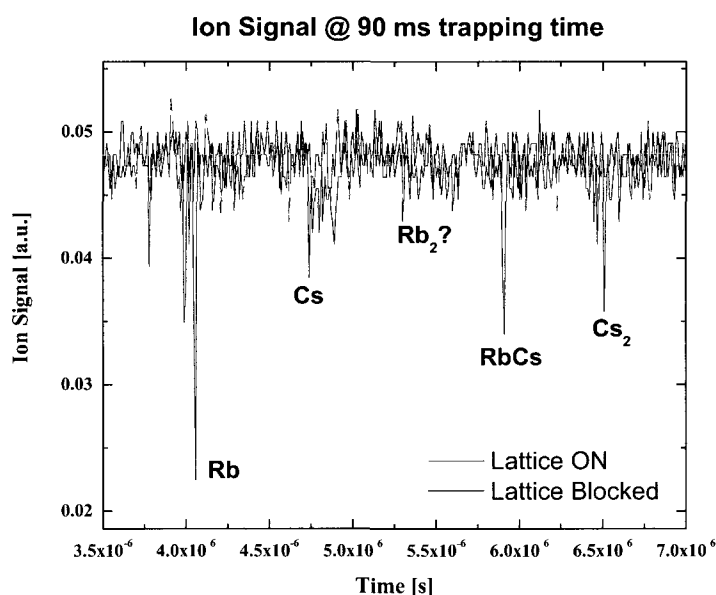


Figure 5.3: A typical time of flight measurement signal from the ion detector. This trace shows the time of flight signal with the relevant species labeled. The data was taken after a 90 ms hold in the lattice.

The ions were detected using a commercial Burle 5901 Magnum electron multiplier. For this experimental work we biased the detector at -2000 V which results in

a gain of $\sim 1.4 \times 10^6$. The resultant signal was fed through an Ortec Ser. 4160 transimpedance amplifier that provided an additional gain of 5 with a 50Ω transimpedance resistor. This voltage was then digitized using an NI 5112 PCI card.

We believed we allowed the opposing electrode to float, but further investigation has revealed that leakage currents effectively ground the opposing electrode. The different species were identified through time-of-flight mass spectrometry as shown in figure 5.3. The time of flight from the trapping region to the detector is proportional to the square root of the mass of the particle, so RbCs signals can be easily differentiated from Rb and Cs atoms as well as Rb₂ and Cs₂ molecules.

5.1.3 Push Beams

One other loading tool we added to the apparatus was a pair of dedicated beams to selectively remove atoms from the optical lattice. Because our ultimate goal was to study molecules, we wanted a species-selective way to remove atoms from the lattice without affecting the molecular sample. The solution was a pair of dedicated beams close to resonance with cycling transitions as used for trapping atoms in the MOTs. These beams were generated from the undeflected order of the AOMs that create the absorption light. Each undeflected beam passes through an AOM that shifts it on resonance with the MOT trapping transition. The frequencies of the AOMs were 100 MHz for Cs and 78.6 MHz for Rb. The beams are combined on a polarizing beam splitter, coupled into a multimode optical fiber and aligned with the atom-trapping region.

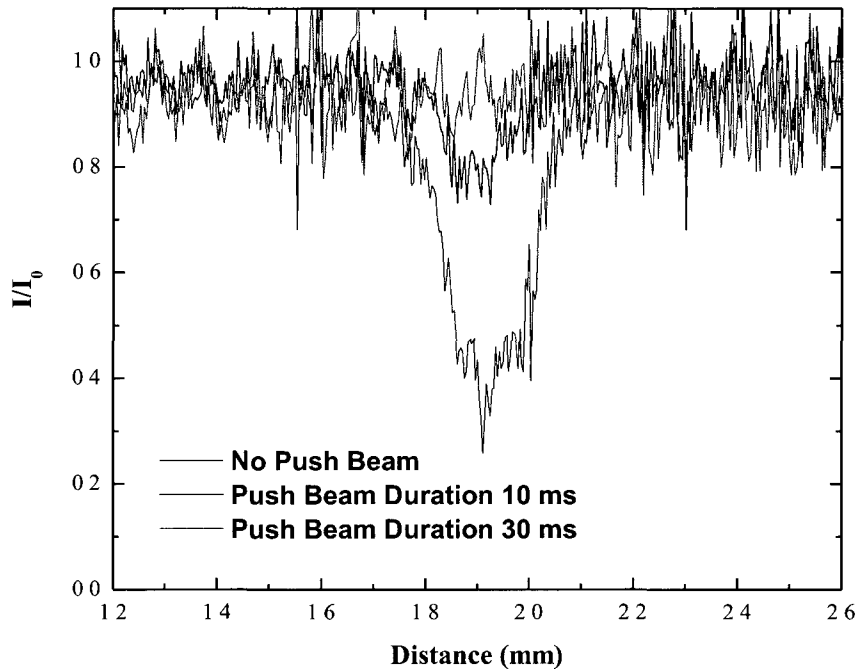


Figure 5.4: The effect of the 30 mW dedicated push beams on a Rb sample in a lattice. The push beams and repump light illuminated the atomic sample for a variable time as noted on the graph. In all cases the total time the atoms were in the lattice before absorption imaging was fixed at 60 ms. The beam was red-detuned by 20 MHz from the MOT trapping transition in this case.

We implemented the dedicated beams to overcome the differential light shifts caused by the lattice as discussed in chapter 3. We were motivated by the finding that we were unable to depopulate the lattice even by turning on every beam associated with the MOTs. Presumably the force imparted by the MOT trap beams is too well mechanically balanced to be effective in ejecting atoms from the lattice.

The data in figure 5.4 shows the results of our initial push beam calibration. In order to close the cycling transition the repump was switched on whenever the push beams were on. We found it took a collimated 30 mW beam with a 3 mm waist a time of ~ 30 ms to fully remove one species of atoms from the lattice. Later, we were able to use

more precise alignment of the beams with the lattice to drop the removal time to 5 ms.

After realignment the repump was nearly sufficient to remove the atoms from the lattice, which supports the “mechanical” balance theory of why the trap beams failed to have an effect.

5.1.4 Signal Optimization

There are two important experimental details for optimizing the RbCs ion signal out of the lattice. The first, which cannot be over-emphasized, is that we were only ever able to generate useful ionization spectra in beam alignments where the signal was wholly dependent on having the 532 nm light present. It is possible to generate spurious ion signals by multiphoton processes due solely to the light from the dye laser. These features are not repeatable and often change, as one would expect when the photoassociation light is turned on and off.

The limiting factor in loading a lattice is typically the limited spatial overlap between the lattice beam and the atoms in the MOT. The typical waist of our lattice is on the order of 100 μm , while a MOT is roughly 1 mm in diameter. Because the lattice had a depth of over 1 mK for all species as described in chapter 3, we were able to trade some of our excess trap depth for increased spatial overlap between the MOTs and the lattice.

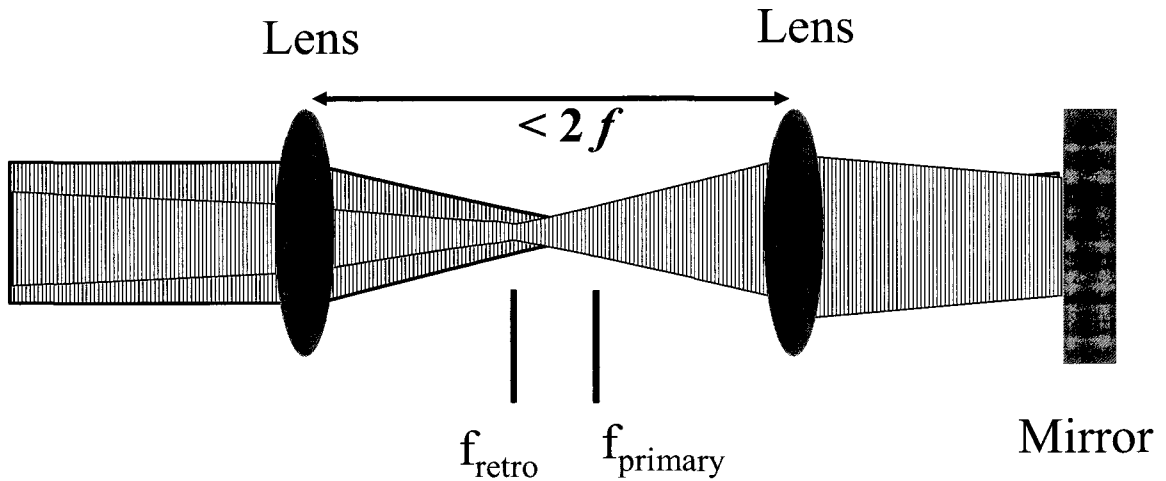


Figure 5.5: Schematic depiction of the intentionally lowered lattice potential. Moving the lenses displaces the foci relative to one another and lowers the trap potential. At the same time it defocuses the trap, allowing much larger spatial overlap with the MOTs and hence loading many more atoms into the trap.

In order to optimize the number of molecules present in the lattice, we moved the focus of our lattice beam 9 mm closer to the opposing lens that makes up the lattice (see Fig. 5.5). This increases the e^{-2} beam waist to $\sim 400 \mu\text{m}$ at the trapping region. This lowers the trap depths to $\sim 150 \mu\text{K}$ for Rb, $\sim 250 \mu\text{K}$ for Cs, and $\sim 300 \mu\text{K}$ for $a^3\Sigma^+$ RbCs. This optimal defocusing was determined empirically by maximizing the ion signal. In addition to increasing spatial overlap, this procedure also greatly reduced the differential light shift caused by the lattice. This in turn rendered the push beams much more effective (5 ms push time) during the experiment.

5.1.5 Experimental Lattice Loading

The QUEST is much deeper for molecules than for atoms and as a result we were able to load molecules into the lattice directly through photoassociation. Ballistic expansion studies of the molecules reveal that they have a temperature of $250 \mu\text{K}$ in the lattice. We interpret this slight heating of the molecules relative to the associated atoms

to be due to the tight confinement of the QUEST. Based on known photoassociation rates we estimate we trap 10^5 molecules in an estimated volume of 10^{-4} cm^3 , leading to an estimated molecular trap density of 10^9 cm^{-3} . This is a rough, order of magnitude estimate based solely on the photoassociation rate combined with an extrapolation of the observed extent of atomic absorption images in the QUEST. There is at least a factor of 2 uncertainty in the trap volume estimate for the molecules due to the lack of a diagnostic that can observe the trap volume for molecules.

When loading atoms into the lattice during the lifetime measurements we had much more success optimizing the molasses phase with the defocused, shallower lattice. It was still very difficult to load atoms directly into even the shallow lattice, but the combination of the smaller light shifts with the larger overlap with the MOTs make loading the MOTs via the molasses stage quite efficient. We used the same protocol we described in Chapter 3 with trap laser detunings optimized for the new lattice depth, but will repeat the exact procedure for clarity.

We red detuned the MOT trap lasers by -6Γ (36 MHz) and -16Γ (83.2 MHz) for Rb and Cs, respectively. Here Γ is the natural line width of the trap transition for each atom. The trap lasers were detuned for 10 ms and during the last 100 μs of this time the repump light was turned off to optically pump all atoms loaded into the QUEST into their lowest (dark) hyperfine ground state. This loading procedure leads to typical densities of $(2 \pm 1) \times 10^{11} \text{ cm}^{-3}$ rubidium atoms and $(6 \pm 1) \times 10^{11} \text{ cm}^{-3}$ cesium atoms occupying a trap volume of roughly $3 \times 10^{-5} \text{ cm}^3$. The temperature of both species in the lattice was measured at $20 \pm 15 \mu\text{K}$ through ballistic expansion. These parameters represent a factor

of 40 increase in density combined with a factor of 5 reduction in the atoms' temperature compared to atoms in a dark spot MOT.

Any atoms that were not wanted in the lattice during a given data run were removed by using the push beams for 10 ms immediately after the molasses sequence. Finally, all light other than the QUEST was extinguished for a variable delay time, after which REMPI was used to state selectively ionize any remaining trapped molecules. The molecules were detected via time of flight mass spectrometry as described above. This experimental sequence allowed us to measure the trap lifetime of the molecules as a function of the environment in the trap.

5.2 Results of the Collision Experiments

We describe the results of the collision experiments and describe a conceptually simple model that is able to explain the results.

5.2.1 Lifetime Measurements

Typical data from a lifetime measurement of molecules in the $a^3\Sigma^+$ ($v=v_0$) state are shown in figure 5.6. The lifetime of the trapped molecules is observed to be severely shortened in the presence of atoms in the lattice. This can be seen by comparing the pure Cs atomic decay shown in the figure with the pure RbCs decay. The lifetime of Cs atoms in the trap is consistent with the background pressure of our vacuum chamber, so we assume that it is limited by elastic collisions with background gas. Because the lifetime data of pure RbCs molecular sample in the trap is nearly coincident with the Cs data, we can infer that the lifetime of the trapped molecules is also background limited.

We attribute the drastic change in the lifetime of the molecules, in the presence of atoms, to be due to inelastic collisions between the atoms and molecules. The inelastic losses are most likely due to rovibrational quenching or hyperfine changing collisions. Any of these degrees of freedom has enough potential energy so that, when it relaxes, it will release enough kinetic energy to liberate both the colliding atom and molecule from the trap.

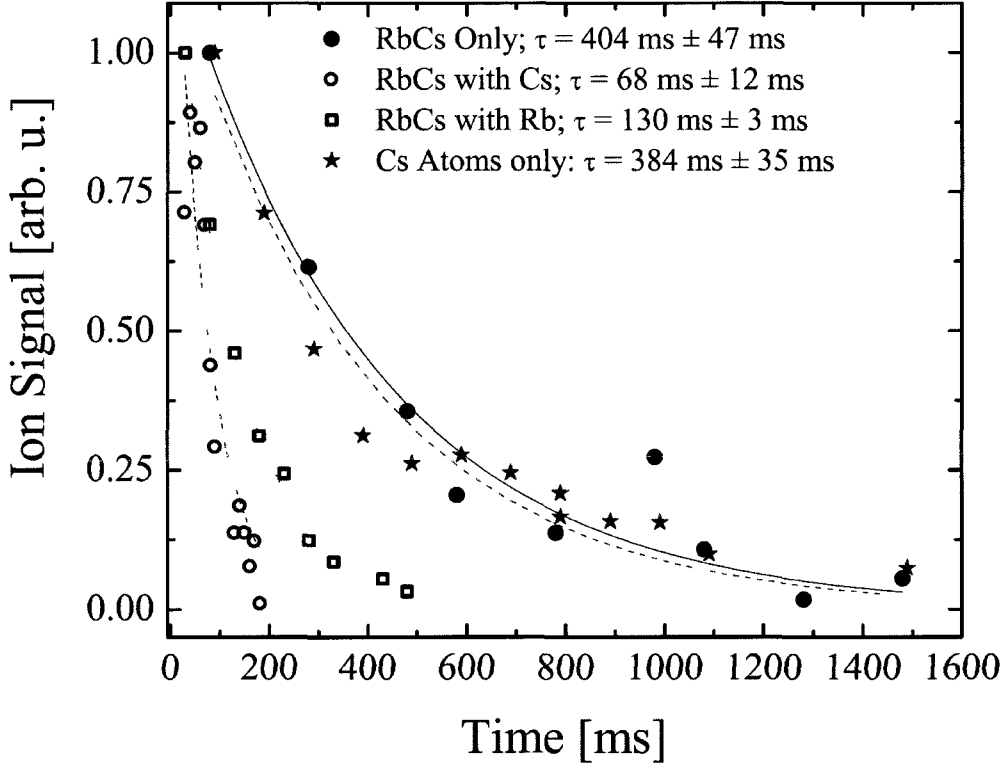


Figure 5.6: Typical molecular lifetime data. Here, the number of molecules in the $a^3\Sigma^+$ ($v=v_0$) state with binding energy $E_B = -5.0 \pm 0.6 \text{ cm}^{-1}$ is observed in the QUEST as a function of time. The presence of inelastic collisions between the atoms and molecules is evidenced by the dramatic reduction of the molecular lifetime when atoms are present. With no atoms present, we observe molecule lifetimes consistent with the background gas-limited lifetime seen for isolated atomic clouds in the trap.

The number of trapped molecules, N_{RbCs} , evolves as

$$\frac{dN_{RbCs}}{dt} = -\Gamma_{BG} + \Gamma_{atom} N_{RbCs} - \frac{\beta}{V} N_{RbCs}^2. \quad (5.1)$$

Here, Γ_{BG} is the loss rate due to collisions with the background gas, Γ_{atom} is the loss rate due to inelastic collisions with atoms, β is the molecular two-body loss rate, and V is the trap volume occupied by the molecules. Our background gas pressure is high enough and our molecular density is low enough that we have $\beta n_{\text{RbCs}} \ll \Gamma_{\text{BG}}$, where n_{RbCs} is the molecular density. As a result, we can neglect the two-body term in (5.1), define $\tau = \Gamma_{\text{BG}} + \Gamma_{\text{atom}}$, and fit our data to the form $N_{\text{atom}}(t) = N_0 e^{-t/\tau}$. We can extract a value for Γ_{atom} from our fit and relate it to the energy-dependent inelastic cross-section, $\sigma(E)$ and relative atomic velocity v , as

$$\Gamma_{\text{atom}} = n_{\text{atom}} \langle \sigma(E)v \rangle = n_{\text{atom}} K(T), \quad (5.2)$$

where $\langle \rangle$ is a thermal average over the relative velocities of the sample and $K(T)$ is the scattering rate constant as a function of temperature.

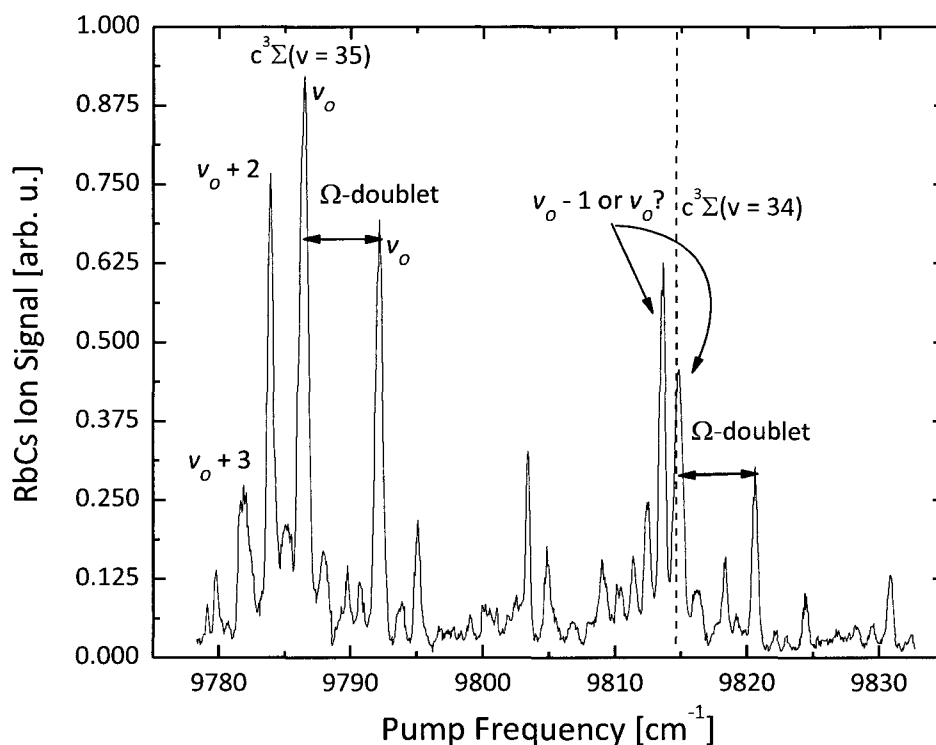


Figure 5.7: Spectroscopy and population distribution of the $a^3\Sigma^+$ state. The substructure present in the $a^3\Sigma^+ \rightarrow c^3\Sigma^+$ spectrum is shown for vibrational levels 34 and 35 of the $c^3\Sigma^+$ state. The doublet peak structure within each of these levels corresponds to the $\Omega = 0$ - and 1 components of the $c^3\Sigma^+$ state. The finer structure within each of the Ω manifolds corresponds to the vibrational structure of the a state. The vertical dashed line shows where the $v=v_0$ we refer to throughout the text is located.

The photoassociation process populates several vibrational levels within the $a^3\Sigma^+$ state. Figure 5.7 shows the various substructures present in the $a^3\Sigma^+ \rightarrow c^3\Sigma^+$ spectrum. The data was generated by scanning the frequency of the resonant pulse during REMPI to map out the population distribution of the triplet state. This illustrates how we are able to selectively detect a particular vibrational level of the a state.

We utilize this state-selective REMPI detection to measure data similar to figure 5.6 for many different vibrational states in the $a^3\Sigma^+$ potential. The binding energies of

these states relative to the $a^3\Sigma^+$ asymptote range from $E_B = -0.5 \text{ cm}^{-1}$ to -7 cm^{-1} .⁷² The results of this study are summarized below in figure 5.8.

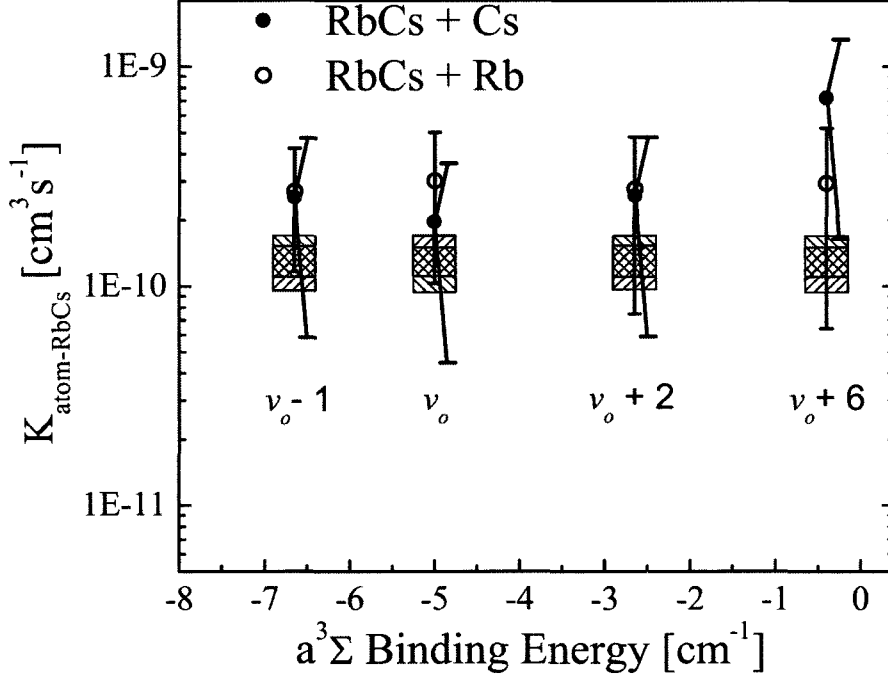


Figure 5.8: Molecular trap-loss scattering rate constant K vs. binding energy for molecules in specific vibrational levels of the $a^3\Sigma^+$ state. The vibrational state label is below each data point. The black (red) crosshatched box is the prediction of the inelastic collision model described in the text below for collisions with Cs (Rb). The width of the boxes shows the uncertainty of in the collision temperature.

Because the molecules are loaded into the lattice at a different temperature than the atoms, there is a systematic uncertainty in determining the trap volume which they occupy. Our ion detection is destructive and necessarily relies on removal of the molecules from the lattice, so we do not have precise knowledge of the volume occupied by the molecules once they are loaded into the lattice. We measure the temperature of the molecules to be roughly $250 \mu\text{K}$, which suggests that the molecules are heated as they load into the trap. As a result, we expect them to occupy a different volume than the atoms in the lattice and have chosen to bound our volume estimate with the most conservative, but measurable, volumes in our system. We set the uppermost bound of

the RbCs lattice occupation volume as the volume of the MOTs as determined by absorption imaging of atoms. We set the lower bound of the occupation volume as the measured atomic lattice occupation volume as determined by absorption imaging. The error bars at each point in (5.8) are dominated by this uncertainty.

Despite more than an order of magnitude variation in the binding energy, the measured collision rates are identical within experimental precision. The size of the molecule and its rovibrational spacing change substantially over this range of energies. The insensitivity of the measured scattering rates to the changes in binding energy suggest a process that is insensitive to the short-range details of the interaction potential. This idea is encouraged by the agreement of the data with the results of a simple model of the collision process shown in figure 5.8 as hatched boxes. This model, developed by Orzel⁷⁵ and coworkers, assumes that any collision that penetrates to a short range results in an inelastic collision resulting in trap loss.

5.2.2 Inelastic Collision Model

Using a slightly different treatment than that covered in chapter 4, we can write the energy-dependent cross section for the ℓ^{th} partial wave with projection m from state i to state f in all outgoing waves ℓ', m' as

$$\sigma_{\ell,m}(E, i \rightarrow f) = \frac{\pi}{k^2} \sum_{\ell', m'} |T_{\ell,m,\ell',m'}(E, i \rightarrow f)|^2. \quad (5.3)$$

In this case the quantity $T_{\ell,m,\ell',m'}(E, i \rightarrow f)$ is the so-called ‘‘T-Matrix’’ which is related to the familiar ‘‘S-Matrix’’ from chapter 4 by the relation $T=1-S$. The T-Matrix describes

the probability for a transition from the incoming spherical wave $\psi_{i,\ell,m}$ to the outgoing wave $\psi_{f,\ell',m'}$. In this case we define the wave vector for a given reduced mass μ and collision energy E as $k = \sqrt{2\mu E/\hbar^2}$ just as in chapter 4. The experiment is only sensitive to the total cross section for all collisions that result in trap loss, so we must sum over all final states f as well as ℓ and m . If we assume that every collision that penetrates to short-range is inelastic, we can write the total cross-section as

$$\sigma(E, i) = \sum_{f,\ell,m} \sigma_{\ell,m}(E, i \rightarrow f) = \sum_{\ell} \frac{\pi}{k^2} (2\ell + 1) P_T(E, \ell), \quad (5.4)$$

where $P_T(E, \ell)$ is the probability of transmission to short-range. This transmission probability can be determined by numerically solving the Schrodinger equation for the long-range potential under the assumption that any incident flux not reflected off of the potential is lost to short-range inelastic processes. This method applies to any highly inelastic process because it only requires knowledge of the long-range behavior of the scattering potential.

The long-range ($R > 10 \text{ \AA}$) behavior of the system is the familiar potential with the centrifugal barrier:

$$V(R, \ell) = \frac{\hbar^2 \ell(\ell + 1)}{2\mu R^2} - \frac{C_6}{R^6}. \quad (5.5)$$

Here the potential is only a function of the Van der Waals coefficient C_6 and μ , the reduced mass. The C_6 for two general colliding particles is determined by integrating over the imaginary frequency portion of the product of their dynamic polarizabilities.⁷⁶ Kotochigova⁷⁷ has calculated the dynamic polarizability of the relevant species in the

system using the method she developed. Using these values we have the values for the various C_6 's listed in Table 5.1.

Table 5.1: Calculated C_6 coefficients for collisions between $a^3\Sigma^+$ RbCs(ν) colliding with various partners. Values are given in atomic units.

Collision Type	(ν_0-1)	(ν_0)	(ν_0+2)	(ν_0+6)
RbCs(ν) + RbCs(ν)	65745	65086	64310	61291
Rb + RbCs	16991	16920	16869	15960
Cs + RbCs	19688	19604	19541	18482

Using these values for the Van der Waal's coefficients, we can calculate values for P_T , σ , and K for RbCs + RbCs, RbCs + Rb, and RbCs + Cs collisions. The results of these calculations are shown in figure 5.9.

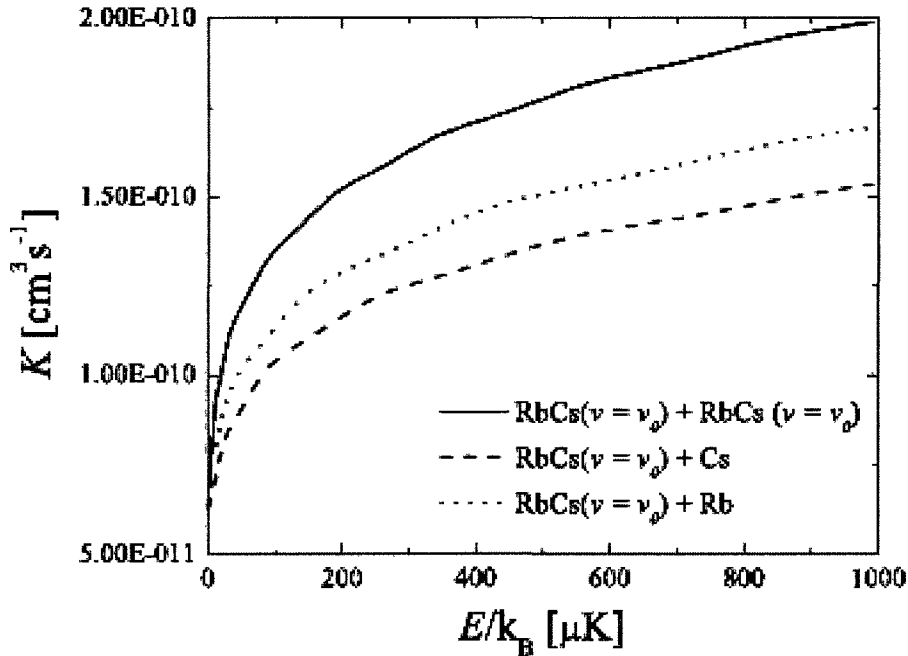


Figure 5.9: Numerically calculated scattering rate constant K vs. center-of-mass frame collision energy E for atom-molecule and molecule-molecule collisions.

The p-wave ($l = 1$) barrier heights from equation (5.5) are $E/k_b \cong 5\mu\text{K}$, $15\mu\text{K}$, and $25\mu\text{K}$ for RbCs colliding with RbCs, Cs, and Rb respectively. At the lowest collision energies the collision rates have *s*-wave ($l = 0$) contributions only. The quantum reflection from the *s*-wave potential scales as $\sigma \propto 1/k$ as $E \rightarrow 0$, which is consistent with the Wigner threshold law for low temperature inelastic scattering, as expected.⁷⁸ This results in a finite probability to scatter at $T = 0$ despite the fact that the unitarity – limited scattering rate scales as $1/v$. The theoretical molecular scattering rate from model allows us to calculate a RbCs – RbCs two body loss rate of 0.1 Hz. Unfortunately, we have a background loss rate of 2 Hz so the model only enables us to show that our molecular losses from the trap are consistent with scattering from background gas.

6 Conclusion

We have demonstrated optical trapping of vibrationally excited, $T = 250 \mu\text{K}$ RbCs molecules in their $a^3\Sigma^+$ electronic ground state. Measurements of the lifetimes of the molecules in the trap show strong inelastic collisions when molecules are co-trapped with atoms. This work represents the first measurement of ultracold collisions with trapped, photoassociated, heteronuclear molecules. We used state-sensitive detection to measure the molecular scattering rate with two species of atoms, over a large range of binding energies.

This work represents a vital intermediate step toward the goal of isolating a trapped, absolute ground state [$X^1\Sigma^+(v=0, J=0)$] sample of polar ultracold molecules. The next step in the experiment is to spin-polarize the atoms before photoassociation to limit the number of hyperfine states available for photoassociation. This will allow precise assignment of quantum numbers to the various levels for use in a new scheme to transfer the molecules to their absolute ground state.

By using Stimulated Adiabatic Raman Passage (STIRAP)⁷⁹ to transfer the molecules instead of the previously used stimulated emission pumping,⁸⁰ one can achieve transfer efficiencies approaching 100%. Based on calculations with available laser powers we estimate a transfer time $\leq 100 \mu\text{s}$, so there should be negligible loss of molecule population due to inelastic collisions during this process. Post-transfer we expect to be able to create an absolute ground state, $20 \mu\text{K}$ sample of molecules with a density greater than or equal to 10^9 cm^{-3} .

Although a denser and colder sample will increase all of the collision rates in the trap, we believe that this can be used to our advantage. If we intentionally load Cs atoms into the lattice with our molecular sample, it will take roughly 100 ms to eject all non-ground state RbCs species from the trap through inelastic collisions. It is believed the $[X^1\Sigma^+(v=0, J=0)]$ absolute ground state molecules cannot undergo inelastic collisions with Cs molecules (although they can inelastically collide with Rb atoms in an energetically permitted substitution reaction. $[RbCs + Rb \rightarrow Rb_2 + Cs]$). After the vibrationally excited RbCs molecules have been ejected from the trap, the push beams can be used to remove the remaining Cs atoms leaving behind a pure trapped sample of $X^1\Sigma^+(v=0, J=0)$ RbCs molecules.

The lasers to do this have already been constructed and are in place, so the main remaining obstacle is the implementation of photoassociation of atoms already trapped in the lattice. This will be necessary because it takes 2 ms to switch off the magnetic field coils of the MOT. During this time the atoms are free to fly away, which makes photoassociation and the subsequent loading of the lattice with spin-polarized molecules very difficult.

These improvements are technically challenging, but fantastic scientists are running the experiment and the implementation of the necessary new systems is already under way.

Bibliography

- ¹ R. V. Krems, Molecules near absolute zero and external field control of atomic and molecular dynamics. *Int. Rev. Phys. Chem.* 24, 99 (2005)
- ² A. Micheli, G. K. Brennen, and P. Zoller. A toolbox for lattice-spin models with polar molecules. *Nature Phys.* 2, 341 (2006)
- ³ D. DeMille. Quantum computation with trapped polar molecules. *Phys. Rev. Lett.* 88, 067901 (2002)
- ⁴ J. P. Gordon. Radiation forces and momenta in dielectric media. *Phys. Rev. A.* 8, 14 (1973)
- ⁵ E.L. Raab, M. Prentiss, A. Cable, S. Chu, and D.E. Pritchard. Trapping of neutral sodium atoms with radiation pressure. *Phys. Rev. Lett.* 59, 2631 (1987)
- ⁶ T. Takekoshi, J.R. Yeh, , and R.J. Knize. Quasielectrostatic trap for neutral atoms. *Opt.Comm.* 114, 421 (1995)
- ⁷ W. D. Phillips and H. Metcalf. Laser deceleration of an atomic beam. *Phys. Rev. Lett.* 48, 596 (1982)
- ⁸ S. Chu, L. Hollberg, J.E. Bjorkholm, A. Cable, and A. Ashkin. Three-dimensional viscous confinement and cooling of atoms by resonance radiation pressure. *Phys. Rev. Lett.* 55, 48 (1985)
- ⁹ A. Ashkin, J.M. Dziedzic, J.E. Bjorkholm and S. Chu. Observation of a single-beam gradient force optical trap for dielectric particles. *Opt. Lett.* 11, 288 (1986)
- ¹⁰ A.V. Avdeenkov and J.L. Bohn. Linking ultracold polar molecules. *Phys. Rev. Lett.* 90, 043006 (2003)
- ¹¹ A. Micheli, G. Pupillo, H. P. Büchler, and P. Zoller. Cold polar molecules in two-dimensional traps. *Phys. Rev. A* 76, 043604 (2007)
- ¹² C. Ticknor, J. L. Bohn. Long-range scattering resonances in strong-field-seeking states of polar molecules. *Phys. Rev. A* 72, 032717 (2005)
- ¹³ E. Bodo, F.A. Gianturco, and A. Dalgarno. F+D2 reaction at ultracold temperatures. *J. Chem. Phys.* 116, 9222 (2002)
- ¹⁴ D. DeMille. Quantum computation with trapped polar molecules. *Phys. Rev. Lett.* 88, 067901 (2002)
- ¹⁵ P.W. Shor. Algorithms for quantum computation: discrete logarithms and factoring. In Proceedings, 35th Annual Symposium on Foundations of Computer Science, Los Alamitos, CA, IEEE Press (1994)
- ¹⁶ H. P. Buchler, E. Demler, M. Lukin, A. Micheli, N. Prokof'ev, G. Pupillo, and P. Zoller. Strongly correlated 2D quantum phases with cold polar molecules: controlling the shape of the interaction potential. *Phys. Rev. Lett.* 98, 060404 (2007)
- ¹⁷ Ryan Barnett, Dmitry Petrov, Mikhail Lukin, and Eugene Demler. Quantum magnetism with multicomponent dipolar molecules in an optical lattice. *Phys. Rev. Lett.* 96, 190401 (2006)
- ¹⁸ A. Micheli, G. Pupillo, H. P. Buchler, and P. Zoller. Cold polar molecules in 2D traps: Tailoring interactions with external fields for novel quantum phases. *Phys. Rev. A* 76, 043604 (2007)

-
- ¹⁹ M. G. Kozlov and D. DeMille. Enhancement of the electric dipole moment of the electron in PbO. *Phys. Rev. Lett.* 89, 133001 (2002)
- ²⁰ S. N. Bagayev, A. E. Baklanov, V. P. Chebotayev, and A. S. Dychkov. Superhigh resolution spectroscopy in methane with cold molecules. *App. Phys. B - Photophysics and Laser Chemistry* 48, 31 (1989)
- ²¹ V. V. Flambaum and M. G. Kozlov. Enhanced sensitivity to the time variation of the fine-structure constant and m_p/m_e in diatomic molecules. *Phys. Rev. Lett.*, 99, 150801 (2007)
- ²² D. DeMille, S. Sainis, J. Sage, T. Bergeman, S. Kotochigova, and E. Tiesinga. Enhanced sensitivity to variation of m_e/m_p in molecular spectra. *Phys. Rev. Lett.* 100, 043202 (2008)
- ²³ S. Bickman, P. Hamilton, Y. Jiang, D. DeMille. Preparation and detection of states with simultaneous spin alignment and molecular orientation in PbO. *Phys. Rev. A* 80, 023418 (2009)
- ²⁴ Amar C. Vutha, Wesley C. Campbell, Yulia V. Gurevich, Nicholas R. Hutzler, Maxwell Parsons, David Patterson, Elizabeth Petrik, Benjamin Spaun, John M. Doyle, Gerald Gabrielse, David DeMille. Search for the electric dipole moment of the electron with thorium monoxide. arXiv:0908.2412
- ²⁵ H.R. Thorsheim, J. Weiner, and P.S. Julienne. Laser-induced photoassociation of ultracold Na atoms. *Physical Review Letters*, 58, 2420 (1987)
- ²⁶ K. Honda *et al.*, Magneto-optical trapping of Yb atoms and a limit on the branching ratio of the 1P_1 state. *Phys. Rev. A* 59, R394 (1999)
- ²⁷ J. Grünert and A. Hemmerich, Sub-Doppler magneto-optical trap for Calcium. *Phys. Rev. A* 65, 041401 (2002)
- ²⁸ Kevin. E. Strecker *et al.* Conversion of an atomic Fermi gas to a long-lived molecular Bose gas. *Phys. Rev. Lett.*, 91, 080406 (2003)
- ²⁹ E. A. Donley *et al.* Atom-molecule coherence in a Bose-Einstein condensate. *Nature*, 417, 529 (2002)
- ³⁰ S.E. Maxwell, N. Brahm, R. deCarvalho, J. Helton, S. V. Nguyen, D. Patterson, J. M. Doyle, D. R. Glenn, J. Petricka, and D. DeMille. High-flux beam source for cold, slow atoms or molecules. *Phys. Rev. Lett.* 95, 173201 (2005)
- ³¹ J.D. Weinstein, R. deCarvalho, T. Guillet, B. Friedrich, and J.M. Doyle. Magnetic trapping of calcium monohydride molecules at millikelvin temperatures. *Nature*, 395, 148 (1998)
- ³² D. DeMille, D.R. Glenn, and J. Petricka. Microwave traps for cold polar molecules. *Eur. Phys. J. D*, 31, 375 (2004)
- ³³ H.L. Bethlem, G. Berden, F.M.H. Crompvoets, R.T. Jongma, A.J.A van Rooij, and G. Meijer. Electrostatic trapping of ammonia molecules. *Nature*, 406, 491 (2000)
- ³⁴ B. C. Sawyer *et al.* Magneto-electrostatic trapping of ground state OH molecules. *Phys. Rev. Lett.* 98, 253002 (2007)
- ³⁵ L. P. Parazzoli, N. J. Fitch, D. Lobser, and H. J. Lewandowski. High-energy-resolution molecular beams for cold collision studies. *New Journal of Physics* 11, 055031 (2009)
- ³⁶ E. R. Hudson *et al.* Efficient Stark deceleration of cold polar molecules. *Eur. Phys. J. D* 31, 351 (2004)

-
- ³⁷ Meystre, *Atom Optics*. New York, NY: Springer Verlag (2001)
- ³⁸ ibid
- ³⁹ Atsushi Hatakeyama, Markus Wilde and Katsuyuki Fukutani, Classification of light-induced desorption of Alkali atoms in glass cells used for atomic physics experiments. *e-J. Surf. Sci. Nanotech.* 4, 63 (2006)
- ⁴⁰ ibid
- ⁴¹ B. P. Anderson and M. A. Kasevich, Loading a vapor-cell magneto optical trap using light-induced atom desorption. *Phys. Rev. A*, 63, 023404 (2001)
- ⁴² S. Aubin et al. Trapping Fermionic ⁴⁰K and Bosonic ⁸⁷Rb on a chip. *J. Low Temp. Phys.* 140, 377-396 (2005)
- ⁴³ D. Budker, D. F. Kimball, and D. P. DeMille, *Atomic Physics: an exploration through problems and solutions*. Oxford University Press (2004)
- ⁴⁴ JM Sage PhD thesis (2006)
- ⁴⁵ E. S. Shuman, J. F. Barry, D. R. Glenn, and D. DeMille. Radiative force from optical cycling on a diatomic molecule. *Phys. Rev. Lett.*, 103, 223001 (2009)
- ⁴⁶ T. Takekoshi, J.R. Yeh, , and R.J. Knize. Quasielectrostatic trap for neutral atoms *Opt.Comm.* 114, 421 (1995)
- ⁴⁷ T. Takekoshi, and R.J. Knize. CO₂ laser trap for Cesium atoms. *Opt. Lett.* 21, 77 (1996)
- ⁴⁸ R. Grimm, M. Weidemüller, and Y. B. Ovchinnikov. Optical dipole traps for neutral atoms. *Adv. At. Mol. Opt. Phys.* 42, 95 (2000)
- ⁴⁹ JT Verdeyen, *Laser Electronics*. Englewood Cliffs, N. J. : Prentice Hall (1994)
- ⁵⁰ M. Mudrich, S. Kraft, K. Singer, R. Grimm, A. Mosk and M. Weidemuller. Sympathetic cooling with two species in an optical trap. *Phys. Rev. Lett.* 88, 253001 (2002)
- ⁵¹ S. Kotochigova, and E. Tiesinga. Controlling polar molecules in optical lattices. *Phys. Rev. A* 73, 041405 (2006)
- ⁵² K. E. Miller, D. Krause, Jr., and L. R. Hunter. Precise measurement of the Stark shift of the rubidium and potassium D1 lines. *Phys. Rev. A*. 49, 5128 (1994)
- ⁵³ C. Krenn, W. Scherf, O. Khait, M. Musso, and L. Windholz, Stark effect investigations of resonance lines of neutral potassium, rubidium, europium and gallium. *Zeitschrift fur Physik D* 41, 229 (1997)
- ⁵⁴ L. R. Hunter, D. Krause, Jr., S. Murthy, and T. W. Sung. Precision measurement of the Stark shift of the cesium D lines. *Phys. Rev. A*. 37, 3283 (1988)
- ⁵⁵ C. E. Tanner and C. Wieman. Precision measurement of the Stark shift in the 6S1/2 → 6P3/2 cesium transition using a frequency-stabilized laser diode. *Phys. Rev. A*. 38, 162 (1988)
- ⁵⁶ W. Ketterle, K. B. Davis, M. A. Joffe, A. Martin, and D. E. Pritchard. High densities of cold atoms in a dark spontaneous-force optical trap. *Phys. Rev. Lett.* 70, 2253 (1993)

-
- ⁵⁷ P. F. Griffin et al. Spatially selective loading of an optical lattice by light-shift engineering using an auxiliary laser field. *New J. Phys.* 8, 11 (2006)
- ⁵⁸ M. Mudrich, S. Kraft, J. Lange, A. Mosk, M. Weidemuller, and E. Tiesinga. Hyperfine-changing collisions in an optically trapped gas of ultracold cesium and lithium. *Phys. Rev. A.* 70, 062712 (2004)
- ⁵⁹ P.M. Johnson. Molecular multiphoton ionization spectroscopy. *Accounts Chem. Res.* 13 (1980)
- ⁶⁰ Demtroder, *Laser Spectroscopy: Basic Concepts and Instrumentation* Berlin: Third Edition Springer-Verlag (2003)
- ⁶¹ J.L. Dunham. The Energy Levels of a Rotating Vibrator. *Phys. Rev.* 41, 721 (1932)
- ⁶² Weissbluth, *Atoms and Molecules*. New York, NY.: Academic Press (1978)
- ⁶³ Gerhard Herzberg. *Molecular Spectra and Molecular Structure, Volume I- Spectra of Diatomic Molecules*. Melbourne, FL: Krieger Publishing Company, second edition, (1950)
- ⁶⁴ J. J. Sakurai. *Modern Quantum Mechanics*. Reading, MA: Addison Wesley (1994)
- ⁶⁵ P.S. Julienne. Cold binary atomic collisions in a light field. *Journal of Research of the National Institute of Standards and Technology.* 101, 487, (1996)
- ⁶⁶ J.R. Taylor. *Scattering Theory*. Hoboken, NJ: John Wiley & Sons (1972)
- ⁶⁷ R. G. Newton. *Scattering Theory of Waves and Particles*, NY, NY: McGraw-Hill (1966)
- ⁶⁸ J. J. Sakurai. *Modern Quantum Mechanics*. Reading, MA: Addison Wesley (1994)
- ⁶⁹ H.J. Metcalf and P. van der Straten. *Laser Cooling and Trapping*. NY, NY: Springer-Verlag (1999)
- ⁷⁰ C.E. Fellows, R.F. Gutterres, A.P.C. Campos, J. Verges, and C. Amiot. The RbCs X₁⁻ + ground electronic state: new spectroscopic study. *Journal of Molecular Spectroscopy*, 197, 19 (1999)
- ⁷¹ J.L. Bohn, and P.S. Julienne Semianalytic theory of laser-assisted resonant cold collisions. *Phys. Rev. A.* 60, 414, (1999)
- ⁷² A. J. Kerman, J. M. Sage, S. Sainis, T. Bergeman, and D. DeMille. Production of ultracold, polar RbCs molecules via photoassociation. *Phys. Rev. Lett.*, 92, 033004, (2004)
- ⁷³ T. Bergeman, P.S. Julienne, C.J. Williams, E. Tiesinga, M.R. Manna, H. Wang, P.L. Gould, and W.C. Stwalley. Photoassociation in 0⁺u and 1g states of K₂. *Journal of Chemical Physics*, 117, 7491, (2002)
- ⁷⁴ A. J. Kerman, J. M. Sage, S. Sainis, T. Bergeman, and D. DeMille. Production and state-selective detection of ultracold RbCs molecules. *Phys. Rev. Lett.*, 92, 153001 (2004)
- ⁷⁵ C. Orzel, M. Walhout, U. Sterr, P.S. Julienne, and S. L. Rolston. Spin polarization and quantum-statistical effects in ultracold ionizing collisions. *Phys. Rev. A.*, 59, 1926, (1999)
- ⁷⁶ M. Marinescu, H. R. Sadeghpour, and A. Dalgarno. Dispersion coefficients for alkali-metal dimers. *Phys. Rev. A*, 49, 982 (1994)
- ⁷⁷ S. Kotochigova, and E. Tiesinga. Controlling polar molecules in optical lattices. *Phys. Rev. A* 73, 041405 (2006)

⁷⁸ N. Balakrishnan, R. Forrey, and A. Dalgarno. Quenching of H₂ vibrations in ultracold ³He and ⁴He Collisions. *Chem. Phys.Lett.* 280, 1 (1997)

⁷⁹ K. Bergmann, H. Theuer, and B. W. Shore. Coherent population transfer among quantum states of atoms and molecules. *Rev. Mod. Phys.* 70, 1003 (1998)

⁸⁰ J. M. Sage, S. Sainis, T. Bergeman, and D. DeMille. Optical production of ultracold polar molecules. *Phys. Rev. Lett.* 94, 203001 (2005)